



FINAL DESIGN REPORT

NACDeC - VII

2023-2024*

Team FlightForge

Aditya Singh[1,†], Kanak Agarwal[1,†]
Parth Jain[1,†], Pranav Karkera[1,†]
Vedant Vijayakrishnan[1,†]

[1] Department of Aeronautical and Automobile Engineering, Manipal Institute of Technology, Manipal, Karnataka, India - 576104

† These authors contributed equally to this work.

* As of the 31^{st} of August, 2024

Contents

Tables

Figures

1 Introduction

1.1 The Problem Definition

The team's objective for this competition is to develop and propose a fully-fledged conceptual UAV for the planetary boundary layer (PBL) study of the lower stratum of the Martian atmosphere. The region of study for the proposed UAV would be the roughness layer corresponding to the initial 100 m above the Martian surface. Fig. 1 was reproduced from reference [5].

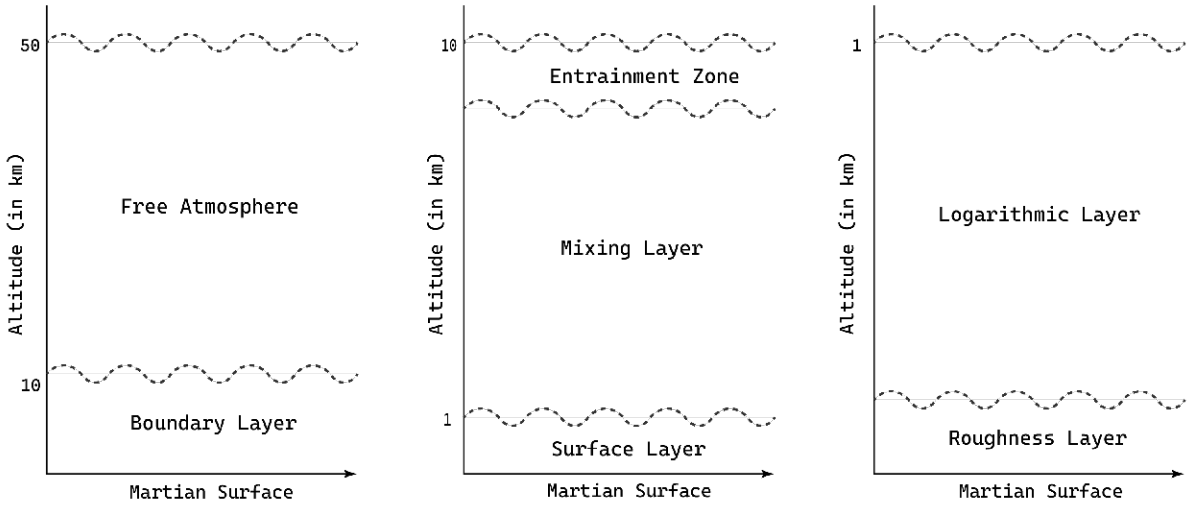

Figure 1: Martian Planetary Boundary Layer (PBL)

1.2 Preliminary Values Provided

The values provided initially as a part of the problem statement were taken as the starting point for the conceptual design process of the UAV and are defined in Tab. 1.

Parameter	Value	Parameter	Value
All up mass of the UAV	$\leq 70\ kg$	Payload Mass	$\geq 5\ kg$
Stowage Modularity	Aeroshell of Diameter 2.5 m	Waiting Period between two flights (after recharging)	100 s
Battery Energy Density	650 kJ/kg	Peak Irradiance on Mars (at 100 m)	586.2 W/m^2
Irradiance Attenuation Factor (at 100 m)	0.70	Length of a Martian Sol	760 minutes
Reserve Battery Fraction after Each Flight	25 %	Mass Fraction of the Battery Health Management System	10 %
Mass Fraction of the Stowage System	10 %	Mass Fraction of the Avionics System	5 %

Table 1: Preliminary Values

1.3 Timeline for the Competition

The requirements for each task were analysed. Post analysis, the work to be carried out was distributed across definite time frames using a Gantt chart (Fig. 2) in order to maximise productivity.

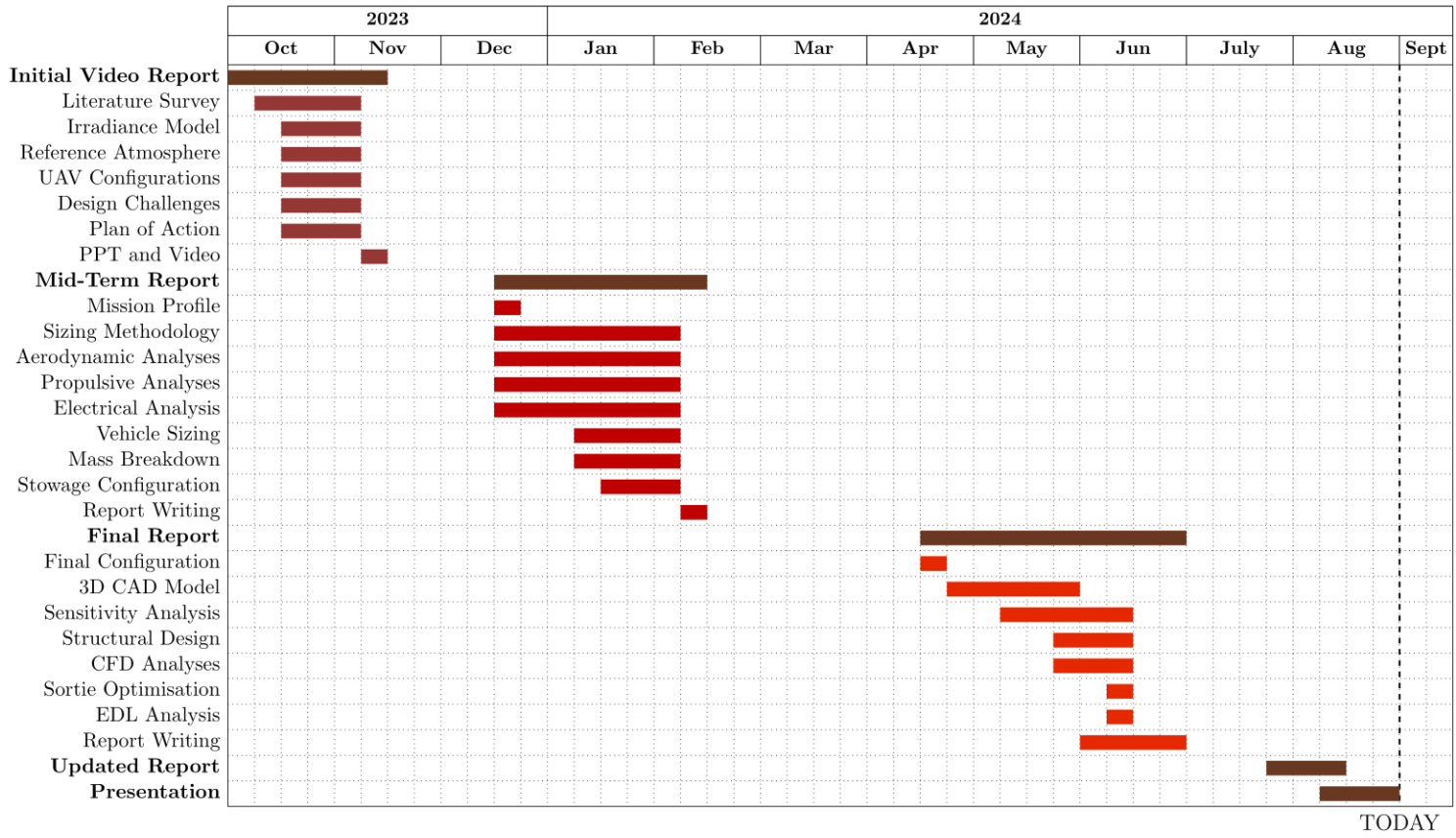

Figure 2: Timeline of the Project

2 Mars: A Brief Overview

Mars, often called the "Red Planet," [6] has captivated human curiosity for decades. The first successful flyby over the planet was performed by a NASA satellite on July 14, 1965 [7]. However, attempts by the then-USSR had begun as early as 1960 [8]. It is the fourth planet in the solar system and is situated 215.46 million km away from the sun. Its unique characteristics make it a focal point of scientific exploration and potential future human endeavours. Striking features mark its surface, including vast deserts, towering volcanoes, and deep canyons. The planet's distinctive reddish hue comes from iron oxide in its soil.

Mars boasts a diameter of approximately 6,779 kilometres, about half the size of Earth [9]. Mars is comparatively less dense than Earth, with 15% of Earth's volume and 11% of Earth's mass, resulting in about 38% of Earth's surface gravity. It experiences extreme temperatures, with highs reaching around 24°C (75°F) near the equator during the day and plummeting to -153°C (-243°F) at the poles during the night [10]. Its thin atmosphere, predominantly carbon dioxide, contributes to the planet's harsh climate, punctuated by intense dust storms that can engulf the entire planet. The atmosphere of Mars consists of about 96% carbon dioxide, 1.93% argon and 1.89% nitrogen, along with traces of oxygen and water [11][12]. Compared to Earth, there is a higher concentration of atmospheric CO_2 and a lower surface pressure in

the Martian atmosphere. The speed of sound is approximately 240 m/s for frequencies below 240 Hz and 250 m/s for higher frequencies [13]. The infographic (Fig. 3) has been reproduced from reference [14].

Mars has been extensively studied by robotic missions, including rovers like Spirit [15], Opportunity [16], Curiosity [17], and Perseverance [18] sent to the Martian planet over the years by the National Aeronautics and Space Administration (NASA). These missions have provided valuable insights into the planet's geology, climate, and potential for past habitability. Evidence suggests that liquid water existed on the Martian surface in the past [12][19], raising questions about the possibility of a past microbial life and the potential for extant life in the planet's subsurface environments. It remains a prime target for future human exploration and possible colonization. Organizations like NASA and SpaceX are actively developing technologies and strategies for crewed missions to Mars. Mars remains at the forefront of scientific research and exploration due to its similarities and differences with Earth, its potential habitability, and its role in understanding planetary evolution and the potential for life beyond Earth.

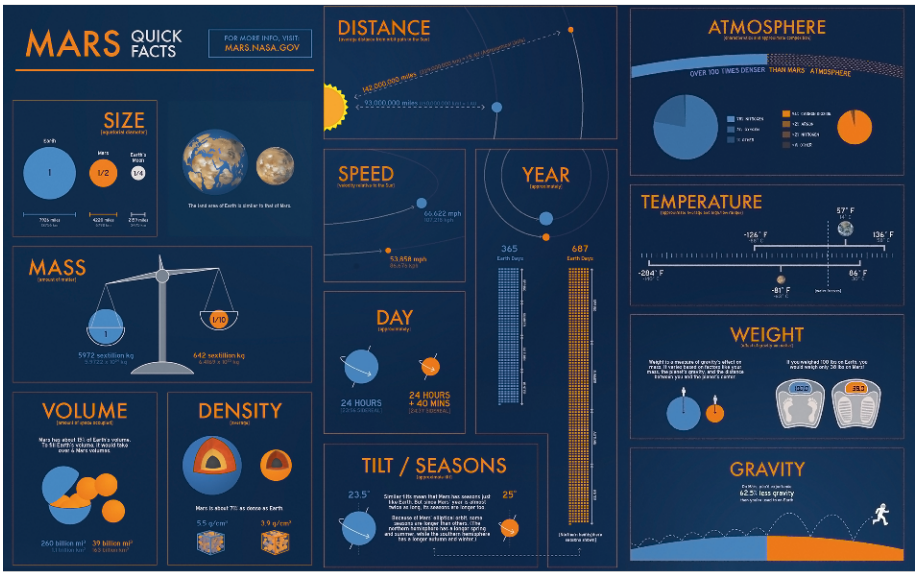

Figure 3: The Martian Planet

3 Martian Reference Atmosphere Model

A Martian reference atmosphere was modelled using the data obtained from the Mars Climate Database [20]. The Mars Climate Database is an open-source Martian climate database that was developed by several academic institutions in collaboration with the European Space Agency (ESA). It incorporates a correction for the CO_2 cycle and has been validated with data obtained throughout MY24 to MY35, corresponding to the previous solar cycle. These statistical models reflect the current best understanding of the Martian atmosphere based on observed conditions and governing physical laws. Version 6.1 was released in 2022 and has been used to obtain the plots in this report. The software is primarily FORTRAN-based and incorporates a Python interface. It was built on Ubuntu 23.10 using NetCDF and gFortran. It can calculate different atmospheric properties based on different scenarios. The atmospheric properties can be calculated at any combination of latitude, longitude, altitude (up to 300 km) and solar longitude (time of the year). The driving factors for these scenarios are the extreme UV input and the amount of dust

suspended in the atmosphere. The primary factors for the modelling of these scenarios are:

- The solar conditions describe variations in the Extreme UV input. Depending on the scenario, either fixed (i.e., constant over time) solar maximum average and/or minimum conditions are provided, or varying (i.e., changing from day to day, as observed) realistic solar EUV.
- The amount and distribution of suspended dust governs the variability in the Martian atmosphere. Hence, the details of the dust distribution and optical properties can be uncertain for a given year. Various models are integrated, assuming different "dust scenarios".

The Mars Climate Database (MCD) can simulate 20 different atmospheric scenarios, including a global dust storm. These 20 scenarios are given by,

- The cold and warm scenarios correspond to low and maximum dust conditions, respectively.
- Standard Climate over the Martian year with three solar EUV conditions (minimum, maximum and average)
- The dust storm scenario depicts the Martian planet in a global dust storm, specifically during northern fall and winter (Ls =180°-360°). It includes three cases of solar EUV inputs: average, minimum, and maximum.
- Exact data simulations for the Martian years 24 to 35.

It can also add perturbations to the data obtained. These are given by:

- Small-scale perturbations due to the propagation (both upwards and horizontally) of gravity waves for any altitudes.
- Large-scale perturbations due to the motion of baroclinic weather systems and other transient waves.
- Perturbations equal to n times the RMS day-to-day variation for all variables.

The Mars Climate Database (MCD) can calculate 90 different atmospheric properties. The following properties would be relevant to designing and developing a UAV for Martian operation.

- Pressure P
- Temperature T
- Density ρ
- Wind components (Zonal, Meridional and Vertical)
- Daily Mean Dust Deposition Rate on a Horizontal Surface ($kg/m^2 \cdot s$)
- Surface Wind Stress ($kg/m \cdot s^2$)
- Surface sensible heat flux (W/m^2)
- Specific Heat Capacity of Air C_p ($J/kg \cdot K$)
- $\gamma = C_p/C_v$ (Ratio of specific heats)
- Reduced molecular gas constant R ($J/kg \cdot K$)
- Kinematic Viscosity of Air ν ($N \cdot s/m^2$)
- Total Electronic Content (TEC) ($1/m^2$) (It is an essential parameter for radio communication and helps determine the scintillation and group and phase delays of a radio wave through a medium)

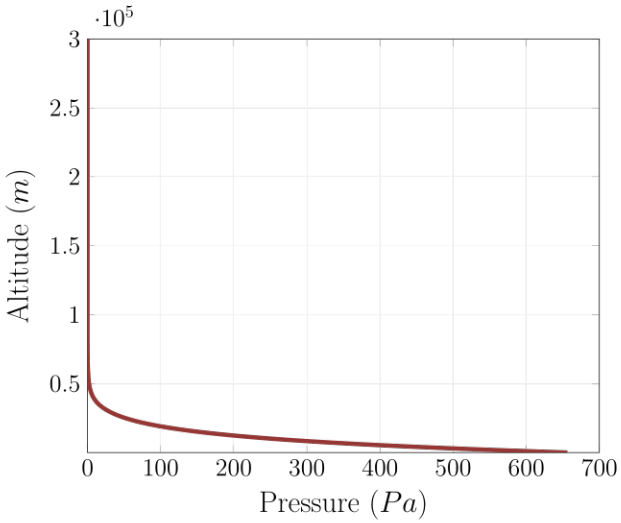

(a)

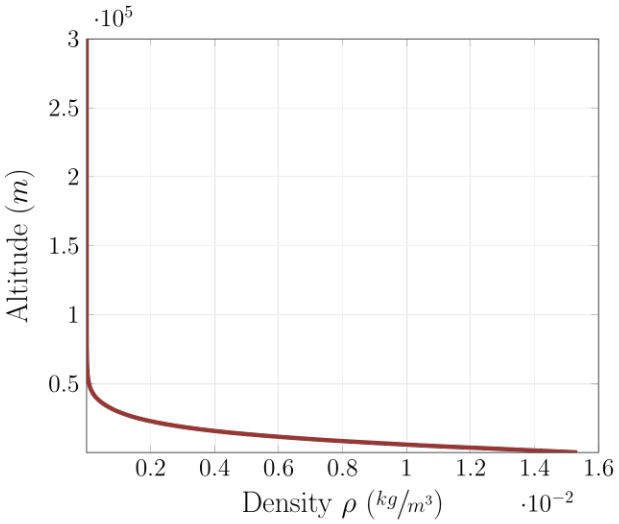

(b)

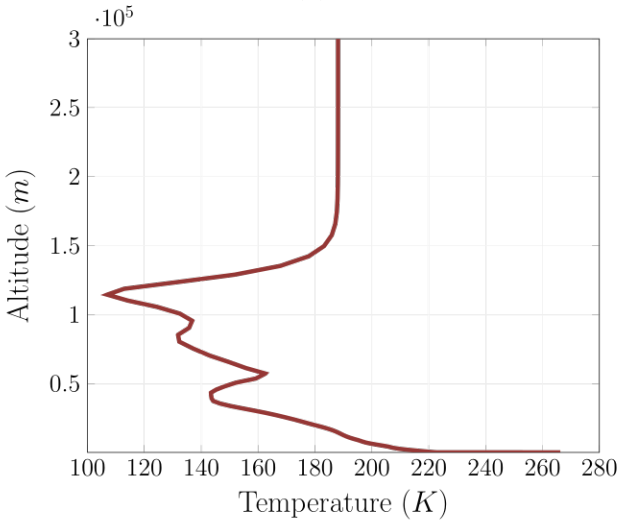

(c)

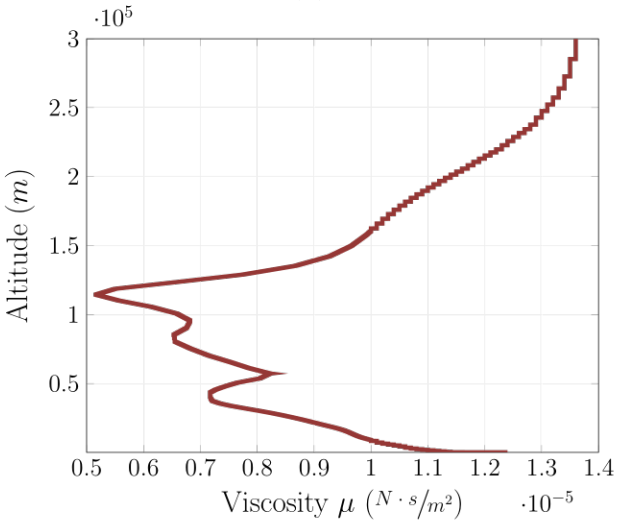

(d)

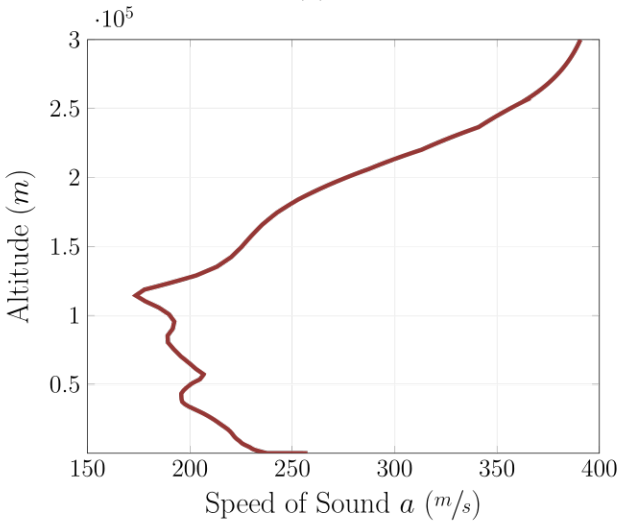

(e)

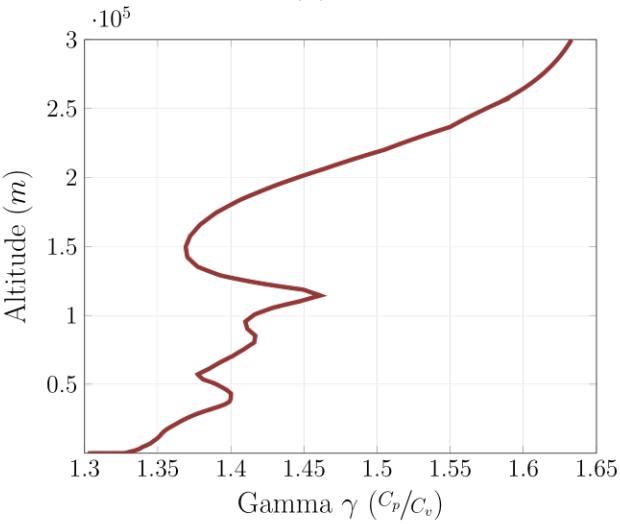

(f)

Figure 4: Martian Properties at constant Latitude & Longitude of 0°, Solar Longitude of 90° & Time = 12 hrs

4 Solar Irradiance Model

An irradiance model was created in MATLAB® after taking into consideration various parameters like the attenuation factor, latitude, Martian sol length and peak irradiance. The equation used to model the solar irradiance is given by,

$$Q = \frac{Q_p \times (\mu/2) \cdot (1 + cos(\pi \times (t - (n \times 60)/2))}{(n \times 60)/2} \cdot cos(\theta) \tag{1}$$

where Q is the solar irradiance, Q_p is the peak solar irradiance, t is the time of the day, μ is the attenuation factor, n is the length of a Martian sol in hours and θ is the latitude. The values used to model the solar irradiance are given below.

Parameter	**Value**
Peak Irradiance on Mars (at 100 m)	586.2 W/m^2
Irradiance Attenuation Factor μ (at 100 m)	0.70
Length of a Martian Sol	12.33 Hours

Table 2: Preliminary Irradiance Values

The solar irradiance at the equator as a function of time, i.e., over the due course of the Martian day, is given in the figure below.

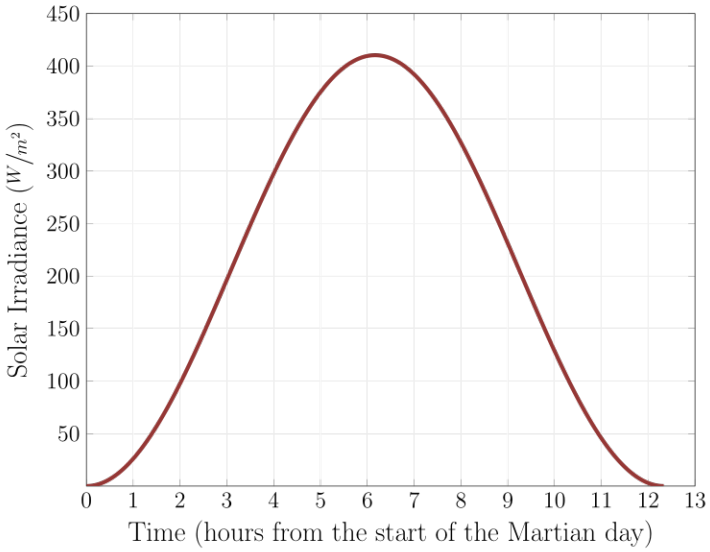

Figure 5: Variation of Solar Irradiance over the Martian Day

The formulation used to calculate and plot the solar irradiance has been obtained from references [21], [22] and [23].

5 Preliminary Mission Profile

Initially, a preliminary mission profile (Fig. 6) was formulated. This helped to improve our understanding of the scope of the problem at hand.

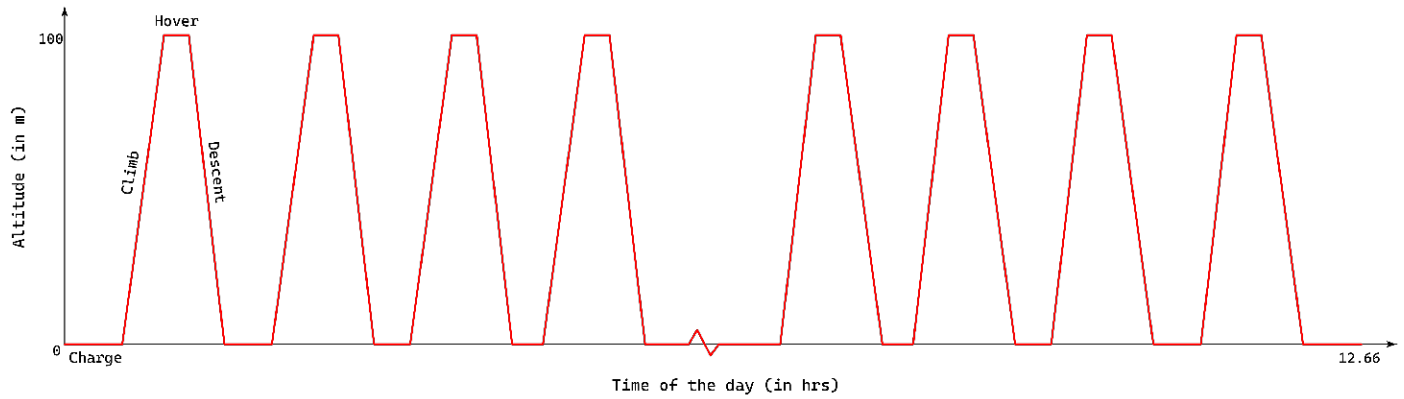

Figure 6: Preliminary Mission Profile

Some significant inferences drawn from the preliminary mission profile include:

- The charging time follows a parabolic trend, with the least charging time at noon and the maximum just after and before sunrise and sunset, respectively.
- The flight time depends solely on the rate of ascent, the rate of descent and the hover time. It is higher for conventional climbing flight (fixed-wing UAVs) when compared to purely vertical flight (rotary UAVs).

6 Entry, Descent and Landing (EDL)

6.1 Introduction

EDL is formally defined as the process of delivering a vehicle from the top of the atmosphere (outer space) to the surface and landing safely [24]. It has been long regarded as the riskiest part of interplanetary exploration missions that aim to land on a different planet (lander missions). There are primarily three stages of flight during a landing approach. These are classified as the following based on flight speeds (Mach Number).

- Entry - Hypersonic Regime of Flight
- Descent - Supersonic Regime of Flight
- Landing - Subsonic Regime of Flight

However, in terms of flight operations, they would be defined as,

- Entry - Guide the spacecraft to the target
- Descent - Turn on the engines
- Landing - Extend the landing gear and throttle the engines for touchdown

Fig. 7 showcases the proposed EDL architecture adopted by the Phoenix lander [25]. In comparison, Fig. 8 represents the actual EDL approach of the Phoenix lander, which was reconstructed and then analysed in reference [26].

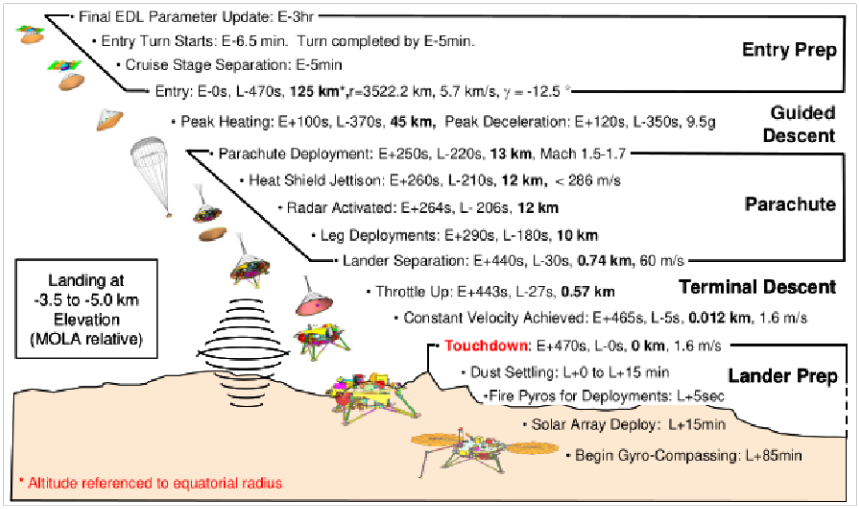

Figure 7: Proposed EDL Architecture of the Phoenix Lander

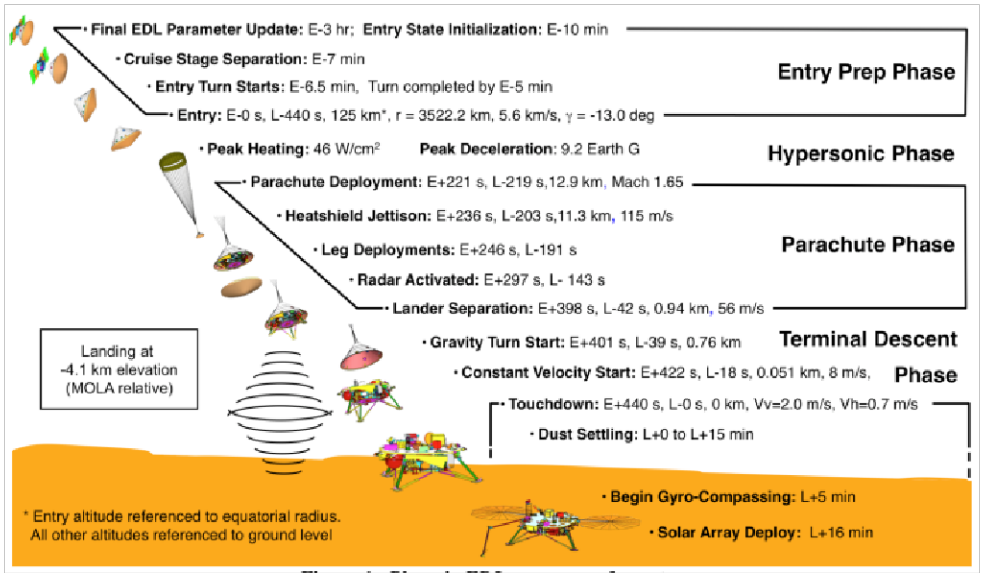

Figure 8: Actual EDL Architecture of the Phoenix Lander

6.2 Challenges Associated with Martian EDL

The Martian EDL approach is fraught with systems engineering challenges [2]. These challenges emanate from various factors, and this section aims to address each of these challenges in detail and the impact of each challenge on the overall system.

6.2.1 Atmospheric Density, Opacity, and Landing Site Elevation

As discussed in Sec. 2, the Martian atmosphere is thinner than that of Earth (Fig. 4b). As a result, Mars entry vehicles tend to decelerate at much lower altitudes and, depending upon their mass, they may never reach the subsonic terminal descent velocity of aerodynamic vehicles re-entering the Earth's atmosphere.

The Martian re-entry follows a ballistic entry rather than a lifting entry, as evident in Fig. 9.

Extreme atmospheric variation across a Martian year limits our ability to develop a standard EDL system. In addition, significant variation in atmospheric dust content (random occurrence) increases the temperature of the lower atmosphere, thus reducing density and affecting the selection of the elevation of the landing site. To date, all successful Martian landings have been to surface sites with elevations less than -1.4 km MOLA (Mars Orbiter Laser Altimeter). This technology-imposed requirement has eliminated surface exploration of the ancient terrain in a majority of the southern hemisphere (average MOLA elevation of +2 km). The coupling of low atmospheric density with complex mission requirements for deceleration has led to entry systems that are designed to produce a high hypersonic drag coefficient.

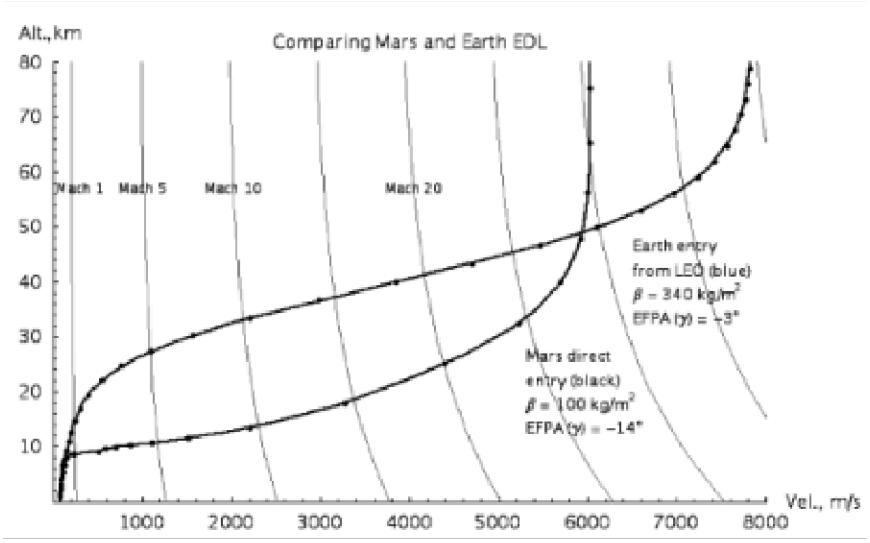

Figure 9: Altitude Velocity Map [2]

6.2.2 Mars Surface Hazards

Landing systems are designed to deliver their payloads within the horizontal and vertical velocity envelopes of their touchdown equipment. Despite contrasting visual differences, previous landing systems have significant commonality. These systems initiate while suspended on a parachute near terminal velocity (55-90 m/s) and at an altitude of 1 km off the Martian surface.

As far as legged landers are concerned, rock hazards pose one of the most significant challenges. Legged landers developed so far have had 20–30 cm of ground clearance. Rock clearance is also especially crucial for the propulsion system. Terminal descent thrusters cannot spend more than a few hundred milliseconds within a meter of the Martian surface without digging trenches, launching small rocks into the landing gear, and producing a destabilizing ground effect on the bottom of the lander. Hence, legged landers with integrated propulsion systems approach the ground at a relatively high speed (2.4 m/s), which introduces the converse effect of increased susceptibility to slope-induced tip-over hazards.

A surface clearance of 30-50 cm is believed to be sufficient for many potentially scientifically significant landing sites on Mars. However, the ability to directly detect rocks of that size from Mars orbit has not yet been accomplished (the current detection limit is > 1 m). Instead, rock size distributions are inferred from

the average thermal inertia of the landing area based on thermal response measured from the infrared thermal mappers, thermal emission spectrometers, and thermal emission imaging system instruments. With the advent of the Mars reconnaissance orbiter, rocks larger than 0.5 m in diameter may become visible from orbit.

Large rocks can also be found in the vicinity of crater rims for craters larger than 100 m in diameter. The landing site selection process attempts to limit the number of large craters (with diameters > 1 km) within the target landing ellipse. However, craters less than 1 km are difficult to avoid when the target ellipse is on the order of 30-80 km or more. Rocks combined with slopes on the scale of a lander may pose touchdown and tip-over hazards as well as potential post-landing solar array deployment interference.

Larger scale surface features like hills, mesas, craters, and trenches pose risks not only to the touchdown system but also to ground sensors. Radar altimetry and Doppler radars can be "spoofed" by slopes and other surface shapes. Horizontal velocity errors may be induced when a wide beam from a Doppler radar measures surface-relative velocity over the slopes.

When performing Monte Carlo simulations that consider the various aspects of EDL, especially expected environmental variations, it is a common practice to count the number of times the EDL system encounters conditions that exceed its design capability envelope. For legged systems, the Martian surface variability causes the largest source of capability violations. On the other hand, for airbag systems, wind variability (and its effect on the touchdown velocity) is the largest source of capability violations. In both these landing systems, environmental conditions result in a 2–15% probability of a capability violation (and hence an associated probability of mission failure). In addition, nonpropulsive landing systems, airbags, and other mechanical means are generally limited to lower lander masses due to the design and qualification challenges associated with these systems in uncertain, rock-abundant terrain.

6.2.3 Space Flight Qualification

Because of the extremely short time span of Mars EDL (order of 5–8 minutes) and the added complexity of switching between units in flight, most critical EDL subsystems are nonredundant (single-string). Hence, EDL systems must exhibit high intrinsic reliability during operation. Further, end-to-end verification and validation tests of the EDL approach are not possible on Earth due to atmospheric and gravitational limitations. This necessitates substantial simulation as a part of the EDL's verification and validation process. This end-to-end simulation must be anchored in data obtained from each EDL component's use in past flights or validated and verified Earth-based testing. The costs associated with the reproduction of a Mars-relevant environment for hypersonic and supersonic EDL systems can be quite large, further limiting the development of novel EDL technologies and restricting approaches to those that are derived from past missions with minor modifications or qualified in ground-based facilities at a reasonably low cost.

6.3 Subsystems Associated with EDL

EDL is a combination of multiple subsystems at play. It requires an extremely precise approach and a small variation can lead to the failure of the entire mission. This is further elucidated in Fig. 10 from reference [24].

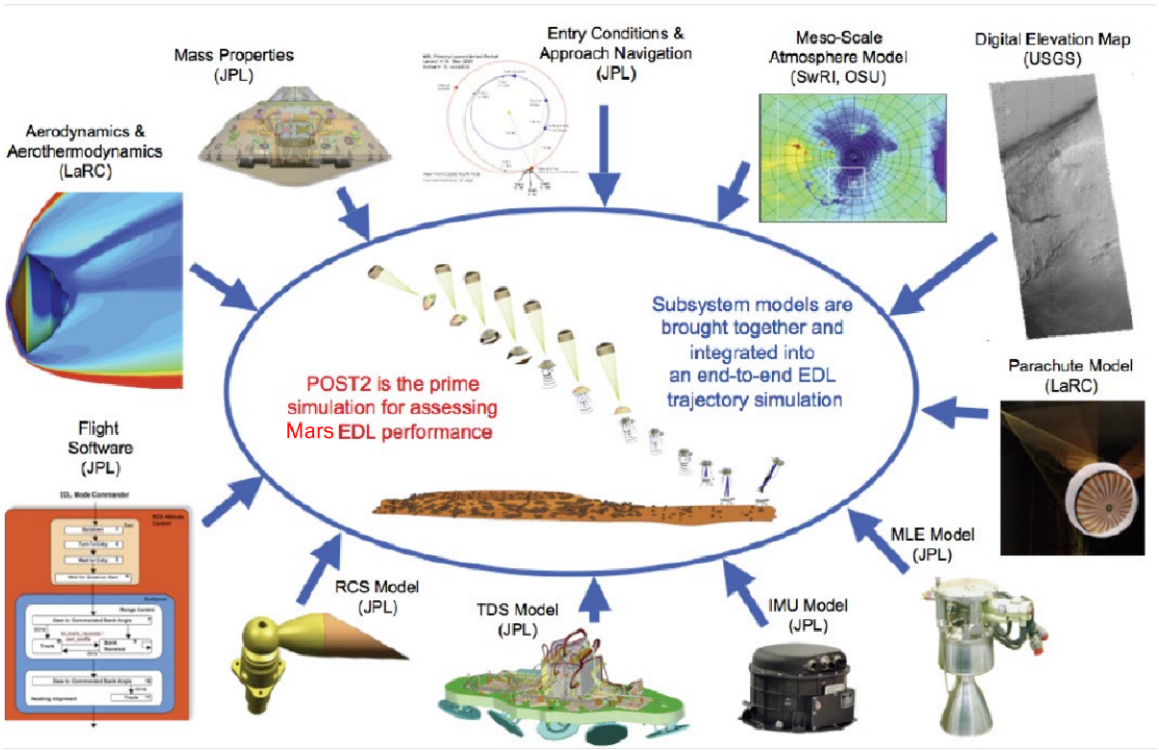

Figure 10: Subsystems for EDL

7 Potential UAV configurations

The mission requirements and limitations were carefully analysed in order to maximise the UAV's effectiveness and efficiency, leading to the selection of the optimal design. In order to achieve this, various configurations were analysed thoroughly, and their strengths and weaknesses were identified.

7.1 Hexacopter configuration

A hexacopter is a UAV powered by six propellers and motors. With six rotors working together, the hexacopter offers superior stability compared to a quadcopter. In the event that one motor fails, the remaining five can compensate, allowing the UAV to maintain control and land safely. This redundancy made them ideal for our applications where reliability is paramount. The additional motor allows for increased thrust, enabling hexacopters to carry heavier payloads while operating their motors at maximum efficiency.

7.1.1 Limitations

Even though many factors suggest that a hexacopter is the ideal configuration, various parameters led to its rejection, as given below.

- **Weather Resistance**: The exposed motors of a hexacopter are significantly more vulnerable to the strong winds found in the Martian atmosphere and increased turbulence compared to the enclosed motors of a coaxial helicopter, limiting their operability in harsh weather conditions.
- **Flight Time**: Due to the usage of multiple motors, the higher power draw of the hexacopter configuration drastically affects flight time and hover time. This is especially a major issue when we take into account the nature of the experiment and the power constraints.
- **Weight**: By utilising six motors instead of one, the gross thrust-to-weight ratio reduces significantly, thereby affecting the maximum payload the UAV is able to carry within the weight constraints. The size and weight of the onboard control systems required to run six motors further limit payload capacity.
- **Vibrations**: Hexacopters utilise six rotors, which increases the inherent vibrations exponentially. This increases the chances of malfunctioning various sensors onboard, including the IMU (Inertial Measurement Unit), which is crucial for navigation and can cause them to give erroneous data, affecting the entire experiment. Vibrations can also loosen electrical connections and, more importantly, cause fatigue, resulting in structural failure.

7.2 Balloon/Airship Configuration

A balloon is an aircraft carrier that is able to float due to its buoyancy and is a potential candidate for future planetary missions. Essentially, there are two types of balloons, Montgolfiere balloons and Super-pressured balloons.

- **Montgolfiere Balloons:** Montgolfieres, which are balloons that are filled with heated ambient atmospheric gas, appear promising for the exploration of Mars. Montgolfieres can be used on Mars in such a way that they are filled by ambient gas flowing in through a hole in the bottom, and the balloon is rapidly heated to provide buoyancy.
- **Super-pressured Balloons:** A super-pressure balloon is a style of aeroelastic balloon where the volume of the balloon is kept relatively constant, and the pressure of the lifting gas is somewhat higher than ambient pressure in the face of changes in ambient pressure outside the balloon, and the temperature of the contained lifting gas.

7.2.1 Limitations

The overall scope of using balloons for the given mission is not promising due to the fact that the operation of this configuration is based on the buoyancy effect of the balloon, which depends on the differential density of the ambient air and lifting gas used. The buoyant force, which must match the weight of the balloon, is calculated in the following way.

$$F_b = m_{balloon} \times g \tag{2}$$

$$(\rho_{air} - \rho_{gas}) \times V_{balloon} \times g = m_{balloon} \times g \tag{3}$$

$$V_{balloon} = \frac{m_{balloon}}{(\rho_{air} - \rho_{gas})} \tag{4}$$

Due to atmospheric air having extremely low density on Mars, the volume of the balloon required to lift a certain mass is substantially larger than that on Earth, and thus, the volume of the balloon on Mars must be unreasonably large for the mission.

Another limitation for Montgolfieres is that they are vastly affected by the temperature variation of the atmosphere during the sol, whereas for super-pressure balloons, there is a risk in carrying pressurised Helium gas for which a fully impermeable membrane must be ensured.

7.3 Fixed Wing Configuration

For a fixed-wing configuration assuming the fundamental cruise condition that L = W and substituting that into the following equation, we obtain,

$$L \;=\; W \longrightarrow \frac{1}{2}\,\rho \times V^2 \times S \times C_L \;=\; W \tag{5}$$

We conducted a parametric study and concluded that a fixed-wing UAV is not feasible due to the unrealistic C_L requirements and the substantially large planform area associated with it. Furthermore, there are various other shortcomings for this configuration which contributed to its rejection.

- Lack of suitable flat landing zones on the Martian surface.
- This configuration cannot utilise the provided sensor package to its maximum potential due to the frequency of landings and subsequent take-offs which need to be carried out.
- The necessary flight envelope for the operation of this UAV is not optimised for this configuration.

7.4 Hybrid Configuration

7.4.1 Advantages

- **Versatility:** Hybrid UAVs combine the vertical takeoff and landing capabilities of rotorcraft with the efficiency and range of fixed-wing aircraft.
- **Efficiency:** By transitioning from vertical to horizontal flight, hybrid UAVs can achieve higher speeds and cover longer distances more efficiently than conventional platforms.
- **Adaptability to Terrain:** The ability to perform VTOL operations allows hybrid UAVs to operate in rugged or uneven terrain, where conventional fixed-wing aircraft may have difficulty taking off and landing.

7.4.2 Limitations

- **Complexity:** Hybrid UAVs with VTOL capabilities are more complex than either purely rotorcraft or fixed-wing aircraft. They require sophisticated control systems, propulsion mechanisms, and aerodynamic designs to facilitate both vertical and horizontal flight modes. This complexity increases the risk of system failures and maintenance challenges, particularly in the harsh Martian environment.
- **Weight and Size:** Integrating VTOL capabilities into a fixed-wing aircraft design typically adds weight and bulk to the UAV, impacting its overall performance, manoeuvrability, and energy efficiency.

- **Power Requirements:** Hybrid UAVs rely on multiple propulsion systems, including electric motors for VTOL and conventional engines or electric propulsion for fixed-wing flight. Meeting the power requirements of these systems, especially during transitions between flight modes, while also optimizing energy efficiency and battery life, is a complex task.
- **Control and Navigation:** Hybrid UAVs require advanced control and navigation algorithms to seamlessly transition between vertical and horizontal flight modes, maintain stability and control during transitions, and navigate effectively in dynamic and unpredictable environments. A significant technical challenge is ensuring reliable and autonomous operation without real-time communication with Earth.

7.5 Helicopter (Conventional) Configuration

One of the most common configurations for use in UAVs is the conventional helicopter configuration, with a single main rotor producing thrust and a tail rotor producing the opposing counter-torque. This conventional configuration is often preferred due to its long endurance, ability to carry heavier payloads and VTOL capabilities. Nevertheless, for the requirements of the problem statement, we did not proceed with this configuration for the following reasons.

- The helicopter configuration is often optimised for excellent performance during forward flight. However, the UAV to be deployed on Mars is only required to traverse up and down within the roughness layer of the Martian atmosphere boundary layer, with no real requirement to cover a range with forward flight. Subsequently, other configurations, such as the Coaxial rotor, which does not include a tail rotor, would be better optimised for the same. The tail Rotor is an undesirable power source that consumes approximately 7-9% of the total helicopter power.
- The problem statement states that the entire UAV has to be stowed in an aeroshell of diameter 2.5m. Given the especially low surface density of the Martian atmosphere, in order to generate sufficient thrust to get the UAV airborne, the span of the propeller blades will have to be extremely high. This would heavily compromise on realistic propeller stowage solutions.

7.6 Coaxial UAV Configuration

The NASA Ingenuity Martian UAV (Fig. 11) is one of the most prominent examples of a UAV featuring a coaxial rotor, which is also directly applicable to our problem statement. The coaxial configuration features a single motor with two rotors mounted on a concentric shaft, with the propellers turning in opposite directions to produce an effective zero torque. For a similar radius, a coaxial system produces considerably more thrust than a conventional helicopter configuration. Coaxial UAVs, in general, tend to be more compact (desirable while considering stowage) [27] and can carry more payload for the same engine power. The disk loading (Thrust/Rotor Area) is a significant parameter for VTOL aircraft. The low disk loading obtained in the coaxial configuration makes it ideal for efficient hover and rotor thrust utilisation. Furthermore, since the Martian atmosphere often experiences strong dust storms, the enhanced stability that the coaxial configuration provides in cross-wind conditions will be highly desirable. These

advantageous features mean that all analysis henceforth will be carried out on the coaxial single rotor system, which has been selected as our configuration for this problem statement.

Figure 11: The Ingenuity UAV

8 Design Methodology

The following flowchart details the sizing methodology incorporated throughout this report. It involves an iterative process where the design is evaluated at each step of the flowchart.

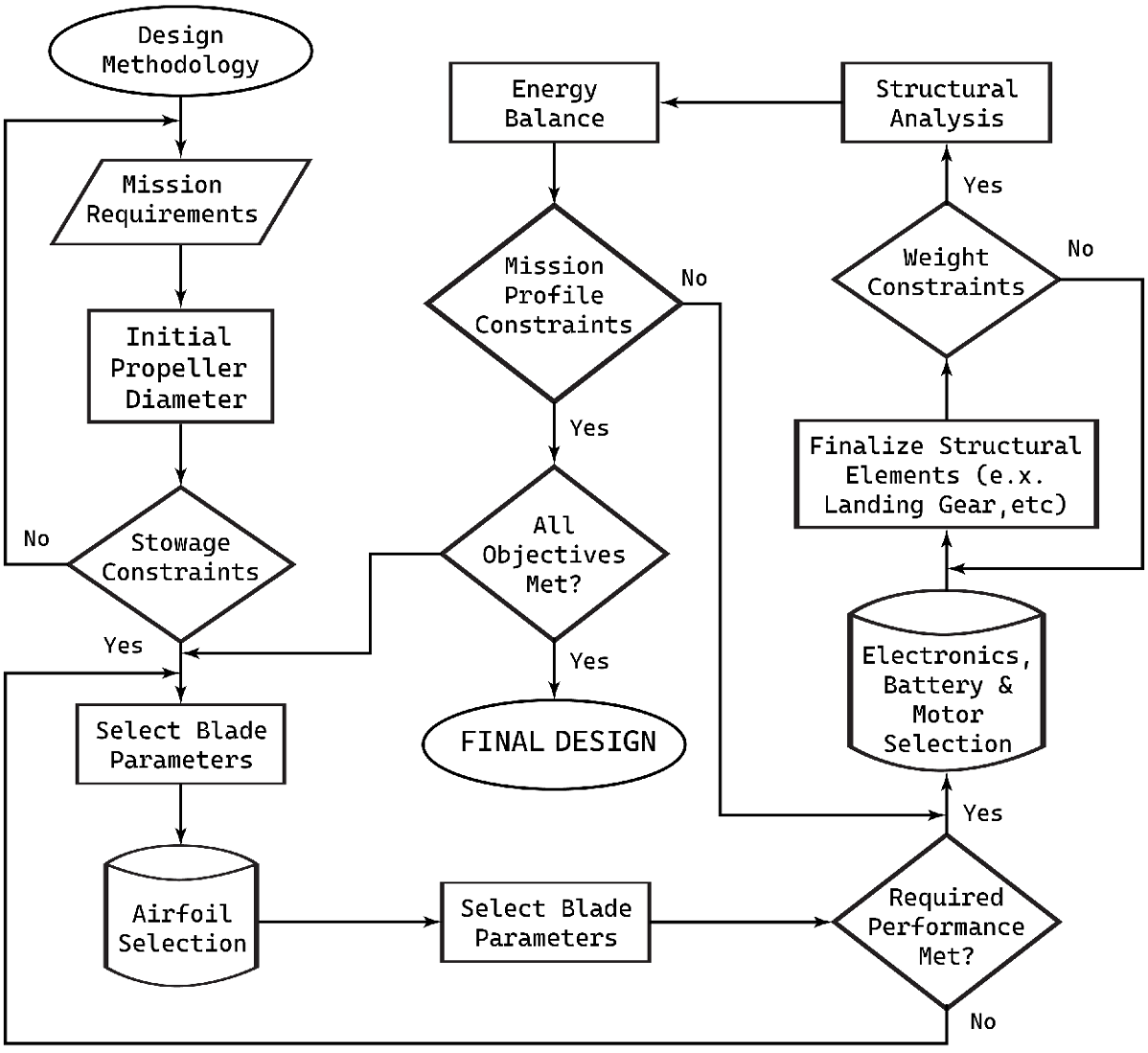

Figure 12: Design Methodology

9 Initial Sizing Constraints

One of the first steps in the sizing methodology was estimating the propeller blade span, as this would be the most significant parameter for all analyses henceforth. The larger the propeller span, the lesser the disc loading (Thrust/Rotor Area) and hence, the power required to hover is lower, so a larger propeller span is always preferred. While there are many constraints and factors to be taken into account during propeller sizing, in our case, the stowage considerations primarily constrain the span of the propellers. As per the problem statement, the entire UAV should be able to be stowed within an aeroshell with a diameter of 2.5 m and a height of 5 m. Even if the propeller span exceeds the aeroshell diameter, it can be retracted and folded upwards using hinges at the root of the blades. Subsequently, since the height of the pod and the other structural elements are unknown yet, 50% of the Aeroshell height, and hence, **2.5** m is designated to stow the propeller blades. This is illustrated in Fig. 13.

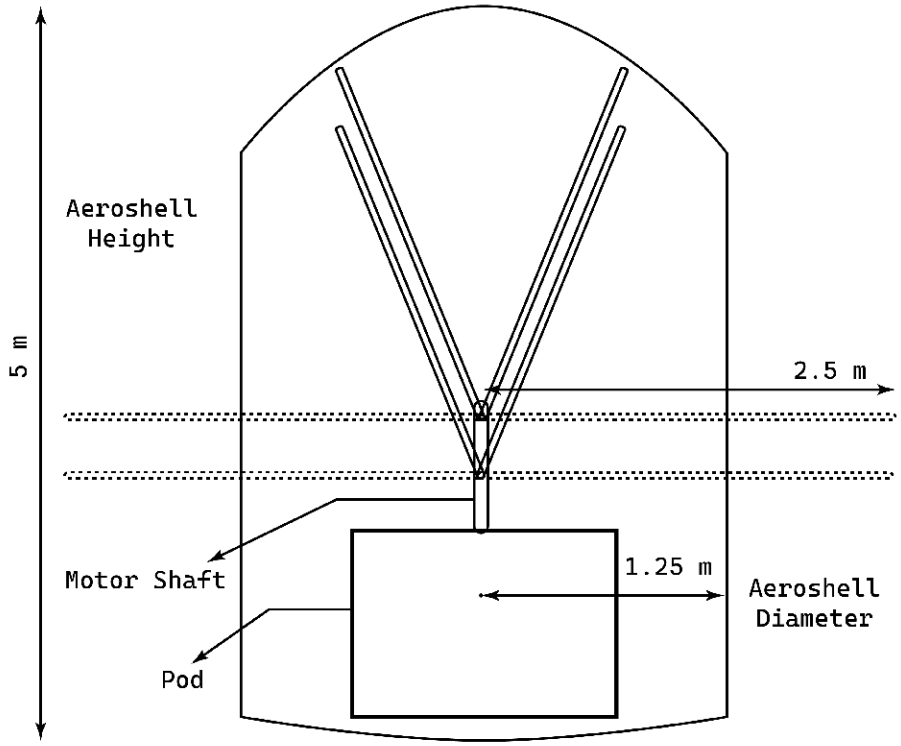

Figure 13: Proposed Stowage of the Propellers

10 Aerodynamic and Performance Analysis

10.1 Analysis Methodology

While accounting for the expected and required type of mission provided in the problem statement that the UAV would potentially perform on Mars, the complete performance estimation and sizing were primarily carried out by considering only the hover and vertical flight (ascent and descent) phases. Nevertheless, power and performance estimations for forward flight have also been carried out and elaborated further in Sec. 10.11.

The performance analysis was carried out primarily using existing analytical methods. The Blade Element

theory and especially the momentum theory were implemented extensively. The momentum theory applies the basic mass, momentum and energy conservation equations of fluid mechanics to model the turbo-machinery interactions between the rotor and the fluid. It essentially states that the power applied by the actuator disc (representing the rotor) equals the rate of change of kinetic energy of the flow passing through the rotor [28]. It provides accurate initial estimations for rotor power, thrust and performance in general. However, it assumes uniform flow through the actuator disc, which is rarely realised in practice. On the other hand, the blade element theory determines rotor performance by estimating blade profile drag losses through the extensive consideration of various rotor blade design parameters [29]. It is important to note that neither the momentum nor the blade element theory considers viscid or compressibility losses, and subsequently, the parameters obtained will have to be scaled accordingly.

Empirical relationships and literature charts were also used wherever possible, namely to estimate and sometimes validate UAV performance parameters. Apart from these methods, numeric means were also employed in the form of OpenFoam CFD and XFLR5 software for airfoil aerodynamic analysis. Furthermore, CFD turbomachinery analysis is carried out on the rotating co-axial propeller model using the commercially available XFlow and Simulia CFD software in order to visualise the flow distribution and wake generation patterns.

10.2 Initial Constants

Tab. 3 depicts some of the initial constants and parameters assumed for this study. These include physical constants, problem statement specifications, and other factors used for the calculations.

Parameter	**Value**
Mass, m	70 kg
Acceleration due to Gravity, g_m	3.71 m/s^2
Thrust	259.7 N
Average Speed of Sound, a_m	240 m/s
Surface Density, ρ_m	0.015 kg/m^3
Dynamic Viscosity, μ_m	1.24×10^{-5} Pas
Kinematic Viscosity, ν_m	8.266666×10^{-4} m^2/s
Radius, R	2.5 m
Propeller Actuator Disc Area, A	19.635 m^2
Tip Loss Factor, B	0.98
Empirical non-uniform flow correction factor, κ	1.1

Table 3: Initial Constants and Parameters

10.3 Propeller Design

In order to proceed further, the propeller design parameters of the coaxial configuration have to be determined. The spinning rotor blades of a helicopter interact with the flow field by pushing it downwards

to generate thrust. It is well known that when any moving or rotating body transgresses into the transonic speed regime (M > 0.8) or above the drag divergence Mach number, there will be an exponential increase in drag due to the formation of shockwaves, which results in a substantial increase in the rotor profile power. For a rotating propeller, the tip velocity (V_{tip}) represents the maximum attained velocity and is subsequently constrained to M = 0.8 in order to remain within the purely subsonic regime. The maximum angular velocity (Ω) and motor RPM can thus be calculated for a propeller radius of 2.5 m, as shown below.

$$V_{tip} = a_m \times M = 240 \times 0.8 = 192 m/s \qquad \Omega_{max} = \frac{V_{tip}}{R} = \frac{192}{2.5} = 76.8\, rad/s \tag{6}$$

$$RPM_{max} = \frac{\Omega_{max}}{2\pi} \times 60 = 733.78\, RPM \tag{7}$$

For a typical coaxial setup, the number of blades per rotor can vary between 2 and 4. It was determined that two blades per rotor would provide sufficient thrust and would also save weight. The chosen configuration also utilises a servo-swashplate mechanism to vary the blade pitch independently for both the top and bottom rotor. This allows us to augment the thrust and facilitate forward flight. Since each rotor has an independent motor, it allows us to vary torque to enhance stability and control.

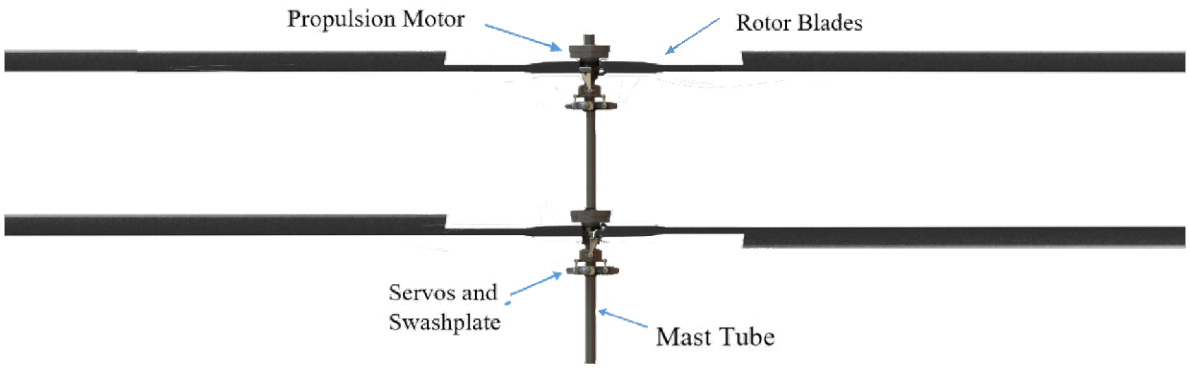

Figure 14: Propeller Configuration

Parameter	**Value**
Speed of sound, a_m	240 m/s
Mach Constraint, M_{max}	0.8
Propeller Tip Velocity, V_{tip}	192 m/s
Angular Velocity, Ω_{max}	76.8 rad/s
Revolutions per second, RPS	12.2231 /s
Revolutions per minute, RPM	733.386
Blade Aspect Ratio, AR	25
Blade Chord, c	0.2 m
Number of blades (per rotor), b	2

Table 4: Propeller Design Parameters

The rotor solidity (σ) is a useful parameter that can be determined to ensure geometric similarity while comparing the coaxial setup to a single rotor configuration. It can also provide a measure of how close the rotor is to the ideal actuator disc approximation used in the momentum theory. It is defined as the area of the rotor blades to the area covered by the actuator disc.

$$\sigma = \frac{bc}{\pi R} = \frac{2 \times 0.2}{\pi \times 2.5} = 0.0509 \tag{8}$$

For a coaxial system, considering four blades, $2\sigma = 0.0509 \times 2 = 0.1018$. For a conventional helicopter, the solidity varies between 0.05 and 0.12 [30]. The other propeller parameters, as shown in Tab. 4, are determined iteratively by calculating the thrust produced, power required, and weight of the propellers at each step and also by considering stowage and other details.

10.4 Airfoil Selection

The airfoil section of the rotor plays an important role in the rotor blade performance. Hence, it is of utmost importance that a closer look is taken at its aerodynamic properties. Maximising C_l while reducing C_d is crucial in order to maximise aerodynamic efficiency. The airfoil section also influences the weight of the rotor through its (t/c) ratio.

Due to the extremely low density on the Martian planet ($0.015\ kg/m^3$), the rotor operates in extremely low Reynolds number flows (of the order of 10^4). Conventional vortex panel methods employed by XFOIL and XFLR5 fail to predict the aerodynamic coefficients, and hence, to predict aerodynamic performance, we are required to use Computational Fluid Dynamics Software. The CFD simulations were conducted using the open-source CFD software OpenFOAM. At low Reynolds numbers, the aerodynamic performance of airfoils deteriorates. At the critical Reynolds number, flat and cambered plates can outperform conventional airfoils. Studies conducted such as that in references [31], [32] and [33] conclude that a cambered flat plate would be the most efficient at a low Reynolds number due to a subcritical flow state. This essentially implies that the boundary layer is fully laminar up to the point of separation without subsequent (turbulent) flow reattachment or on-body transition. In other words, the operating Reynolds number is less than the critical Reynolds number (10^5 for flat plates) and hence more efficient when compared to conventional airfoils.

The simulations were run using the steady-state Reynolds-Averaged Navier-stokes (RANS) simpleFOAM solver along with the viscous Spalart-Allmaras turbulence model. SimpleFOAM is a pressure-based solver (for low-speed incompressible flows) that incorporates the SIMPLE (Semi-implicit Method for pressure-linked equations) algorithm. The Spalart-Allmaras model is widely used in various aerospace applications and is designed for low-velocity wall-bounding flows with boundary layers subject to adverse pressure gradients like in airfoils. It is commonly used for low-Reynolds number flows. The Spalart-Allmaras transport equation, solving for the turbulent kinematic viscosity, $\widetilde{\nu}$, is given below:

$$\frac{\partial}{\partial t}(\rho\widetilde{\nu}) + \frac{\partial}{\partial x_i}(\rho\widetilde{\nu}\mu_i) = \frac{1}{\sigma_{\widetilde{\nu}}}\Big(\frac{\partial}{\partial x_j}\Big[(\mu + \rho\widetilde{\nu})\frac{\partial\widetilde{\nu}}{\partial x_j}\Big] + C_{b2}\rho\left(\frac{\partial\widetilde{\nu}}{\partial x_j}\right)^2\Big) + G_{\widetilde{\nu}} - Y_{\widetilde{\nu}} + S_{\widetilde{\nu}} \tag{9}$$

The turbulent viscosity, ν_t can be determined through:

$$\nu_t = \rho\widetilde{v} f_{v1} \tag{10}$$

Subsequently, the viscous damping function, $f_{\nu 1}$ is given by:

$$f_{v1} = \frac{X^3}{X^3 + C_{v1}^3} \tag{11}$$

X represents the ratio of the turbulent kinematic viscosity to the kinematic viscosity. The Reynolds number of the flow is given by,

$$Re = \frac{\rho \times V_{tip} \times c}{\mu} \tag{12}$$

where, V_{tip} is the tip velocity and c is the chord of the rotor. For the Martian planet, ρ and μ are given by 0.015 kg/m^3 and 1.24 x 10^{-5} Ns/m^2 respectively. The V_{tip} is taken to be 183.264 m/s, which corresponds to a tip Mach number of 0.76. This is suitably in the subsonic regime since a higher value of V_{tip} could potentially lead to the formation of shockwaves due to transonic operation. Taking these factors into consideration, the operating Reynolds number for the current rotor configuration is approximately 30,000.

The mesh consisted of hexahedral cells that were divided into a far-field and a more refined near-field region. Multi-grading techniques were used to control the expansion ratios of the cells within the blocks and to make the boundary layer region close to the airfoil wall especially refined. A grid independence study was conducted, and the number of cells in the mesh was finalised to be 1,98,000. The mesh is given in the following figures.

With the chosen first layer height and mesh refinement, the average y^+ value obtained during the course of the simulations was approximately 0.15. This should sufficiently resolve the inner parts of the boundary layer. The simulations were performed at various angles of attack, and the results of the validation study are given below.

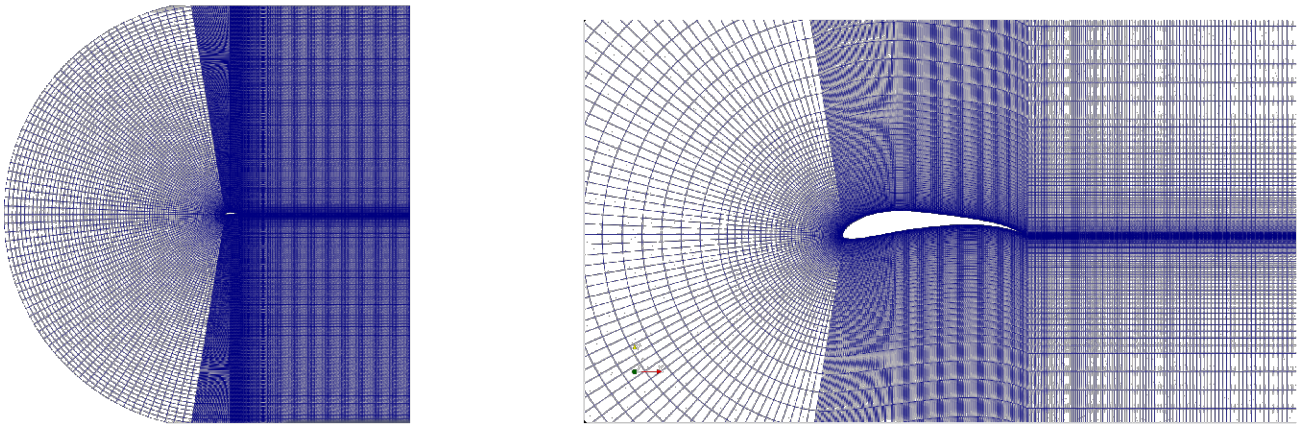

(a) (b)

Figure 15: Mesh

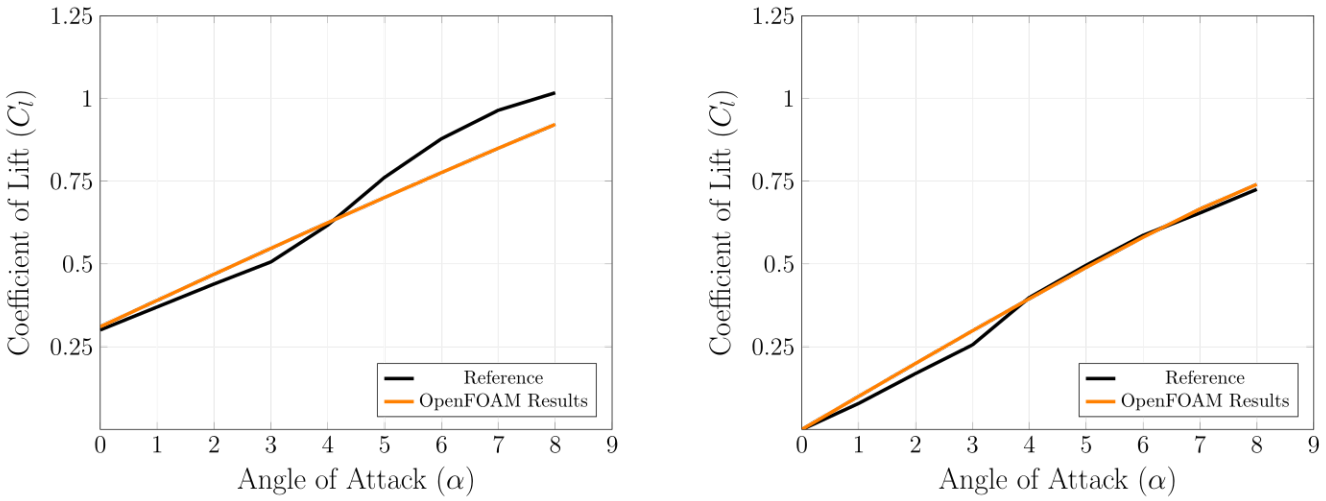

(a) NACA 4412 at Re = 42,100 [34]

(b) SD 8020 at Re = 30,000 [35]

Figure 16: Validation Plots of the Lift Coefficient vs the Angle of Attack

CFD simulations were run on roughly 140 airfoils at various angles of attack, and one of them was finalised. This airfoil has been optimised for maximum propulsive performance under Martian conditions. The finalised airfoil is an interpolation between the NACA 6603 and the Selig S1223 airfoils and was generated using XFLR5.

Figure 17: Airfoil

Its aerodynamic characteristics are given by,

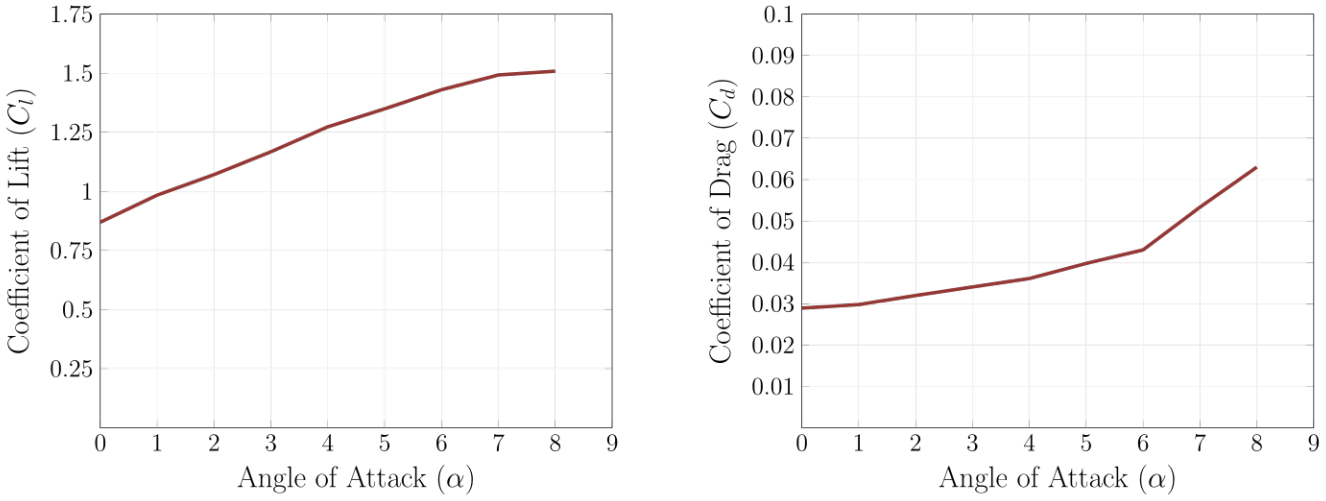

(a) C_l v/s α

(b) C_d v/s α

Figure 18: Aerodynamic Characteristics of the Selected Airfoil

10.5 Hover Performance

For any VTOL aircraft or UAV, the performance estimation usually begins by considering its hover performance. Hover represents the operating state of a rotor system which has no relative velocity with

respect to the air, either vertical or horizontal. The weight of the UAV is sustained by the thrust produced in the upward direction due to the rotating propellers. This results in the acceleration of air downwards with a velocity increment in the wake known as the induced velocity (v_{i_h}). The power required to generate the induced velocity represents the induced power of the UAV. For initial and hover considerations, the thrust required can be assumed to be equal to the weight of the UAV. Initially, the mass is assumed to be the maximum allowable mass of 70 kg. The final mass of the UAV design is iteratively determined through weight distribution analysis later in Sec. 17. (The subscript 'm' in the following equations indicates values on Mars).

$$T_h = W_m = g_m \times m = 3.71 \times 70 = 259.7\ N \tag{13}$$

The induced velocity and, subsequently, the induced power for a conventional helicopter configuration can be determined using the following equations [3]:

$$v_{i_h} = \sqrt{\frac{T_h}{2 \times rho \times A}} \qquad P_i = T_h \times v_{i_h} \tag{14}$$

A coaxial rotor configuration inherently produces more thrust than a single rotor of the same radius. One of the most important design parameters for defining a coaxial propeller is the separation ratio (d_h), which is the ratio of the separation distance between the rotors and the rotor diameter. After passing through the upper rotor, the wake contracts, and the wake swirl loss reduces. Subsequently, a lower rotor positioned at a finite distance below the upper rotor consists of an area (A_{active}) outside the upper rotor wake slipstream that also serves as an active area for the rotor system. Hence, the analytical calculations of a coaxial rotor system can be simplified by approximating to be a single rotor system with a higher effective rotor area (A_{eff}). It has been shown that single rotor theory can be used to calculate coaxial rotor performance as long as wake variations and blade geometry differences have been considered [36].

$$A_{eff} = A_{upper} + A_{active} = (2 - x^2)A \tag{15}$$

where x represents the contraction ratio of the upper rotor wake on the lower rotor radius. The effective area and effective radius, respectively, can be found this way. The contraction ratio is found to be a function of the separation ratio [37].

$$x = \sqrt{\frac{1}{1 + \left[\frac{2d_h}{\sqrt{1+(2d_h)^2}}\right]^{\gamma}}} \tag{16}$$

In Eq. 16, the constant γ represents the influence coefficient which is assumed to be 0.6 according to [37]. For the initially chosen radius of r = 2.5 m, a parametric study of the relationship between the separation ratio and the effective area of the coaxial system is shown below. In general, as the separation between the rotors increases, the effective area of the coaxial system increases, and the rotors tend to behave increasingly like two independent single rotors.

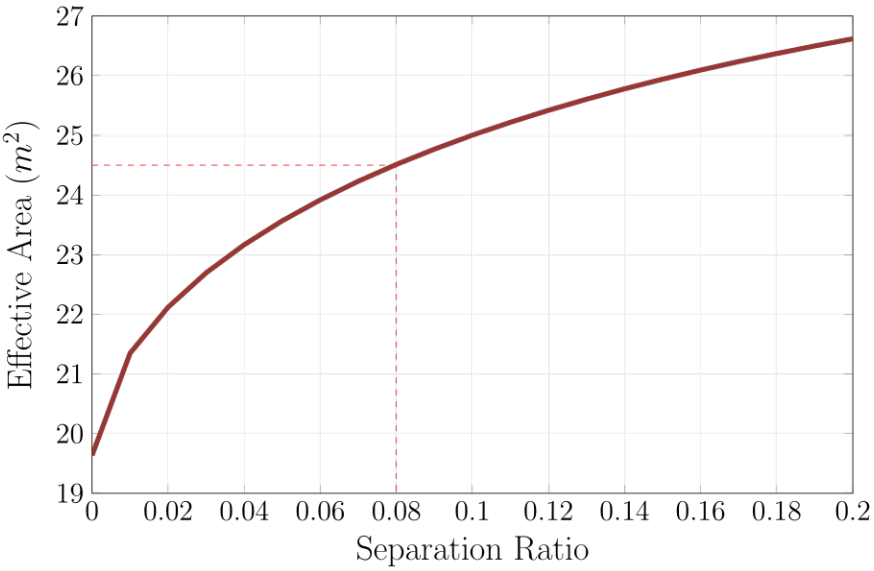

Figure 19: Effective Coaxial Rotor Area v/s Separation Ratio for r = 2.5 m

The separation ratio of most commercial helicopters varies between 0.08 and 0.16 [38]. Subsequently, after iterating the value upon reviewing stowage, aeroshell size and power considerations, an optimum value of d_h = **0.08** was selected [39]. For a radius of 2.5 m, the separation becomes 0.4 m while the effective area of the configuration becomes A_e = **24.5124** m^2. Subsequently, the induced velocity and induced power, respectively, become:

$$v_{i_h} = \frac{259.7}{2 \times 0.015 \times 24.5124} = 18.7924\, m/s \qquad P_i = 256.7 \times 18.7924 = 4880.4\, W \tag{17}$$

Parameter	**Value**
Propeller Separation Ratio, d_h	0.08
Propeller Separation, d	0.4 m
Effective Area, A_e	24.5124 m^2
Effective Radius, R_e	2.7933 m
Induced velocity, v_{i_h}	**18.7924 m/s**
Induced Power (Hover), P_i	**4880.4 W**
Induced Power (single rotor with r = 2.5m)	5453 W

Table 5: Hover Parameters

The induced power of a single rotor configuration with the same radius was also calculated and shown in Tab. 5. It can be inferred that a coaxial system consumes about **12%** lesser induced power than an equivalent single rotor configuration with the same radius [40].

10.6 Thrust Calculation

Analytically derived equations provide satisfactory results for approximate initial estimations. Derived from the blade element theory, the following equations represent the thrust produced by a single-rotor

configuration by considering blade profile drag losses. In order to determine the thrust produced by a Coaxial setup, the effective radius approximation is once again utilised. The lift and drag coefficients, as required in the equation, are obtained from the airfoil Sec. 10.4.

$$\Delta T = \frac{\rho bc(\Omega R_e)^2}{2} \times (C_l cos(\Phi) - C_d sin(\Phi))\Delta R \tag{18}$$

Eq. 18 [41] represents the elemental thrust for the annulus of thickness ΔR at radius R. In the equation, only the lift and drag coefficients can vary with radial distance. However, due to the assumptions involving uniform span-wise flow, these coefficients can be assumed to be constant and the equation can be integrated in terms of the radius 'r'.

$$T = \int_0^R \frac{\rho bc(\Omega R_e)^2}{2} \times (C_l cos(\Phi) - C_d sin(\Phi))dR \tag{19}$$

$$T = \frac{0.015 \times 2 \times 0.2 \times 2.7933 \times (76.8 \times 2.7933)^2}{2} \times (1.43 cos(\Phi) - 0.043 sin(\Phi)) = 549\ N \tag{20}$$

The term Φ represents the inflow angle that can be calculated using the following expression (for a hovering case):

$$\Phi = tan^{-1}\left(\frac{v_{i_h}}{\Omega R}\right) = tan^{-1}\left(\frac{18.7924}{76.8 \times 2.7922}\right) = 5.59^\circ \tag{21}$$

It is inferred that this configuration produces an excess thrust of approximately 290 N more than the weight of the UAV. This excess thrust was provided as a tolerance and for emergencies. Moreover, given the method of estimating the performance of a coaxial propeller using the effective single propeller method, it is preferred to overestimate the tolerance and margin for error. For purely hovering flight, the RPM of the motor can be reduced to match the weight of the UAV.

$$\Omega_{hover} = 52.77 \text{ rad/sec} \qquad RPM_{hover} = 503.99 \qquad M_{hover} = 0.5498 \tag{22}$$

10.7 Hover Power

In order to estimate the required motor power, the total power of the UAV has to be estimated. The total power of a typical helicopter consists of induced power, profile power, parasitic power, and other miscellaneous power sources. During hover and low helicopter velocities, the parasitic power, which represents the power required to move the UAV through the air, is insignificant and is subsequently not considered henceforth. During hover for a helicopter, the ideal induced power at peak motor efficiency constitutes approximately 55-70% of the total hover power. The tail rotor consumes anywhere around 10% of the total power [42]. Given that there is no tail rotor in a Coaxial configuration (as the counter-rotating propellers already generate a net zero torque) and that there are no shaft losses to consider as in a conventional helicopter due to the use of an electric motor, the induced power is assumed to be above 60% of the total hover power.

The other major power component during hover is the profile power P_p. It represents the power required to turn the rotor in air, hence overcoming the viscous forces [43]. It is heavily dependent on the airfoil blade section drag coefficient [44].

$$P_p = \rho b c R_e^4 \Omega^3 C_D = 0.015 \times 2 \times 0.2 \times 2.7933^4 \times 52.77^3 \times 0.043 = 2348.3\ W \tag{23}$$

The total hover power required to turn the propellers can be subsequently estimated. It is important to note that the actuator disc theory of the momentum equation used to determine the induced power assumes ideal rotor operation and uniform wake flow. However, in reality, tip losses exist, and the wake flow will be heavily non-uniform, varying significantly in the radial direction. The former is accounted for by incorporating the tip loss factor, B, into the expression for induced drag. Apart from these losses, other power sources, such as the swirl in the wake, will contribute to the total hover power. These sources are challenging to model analytically. Moreover, scaling is required to obtain realistic values as the momentum theory used till now does not account for inviscid or compressibility effects. Hence, an overestimation of 500 W (approximately 6.5% of the total hover power) is added to account for all the other miscellaneous power sources. The total hover power (P_t) is:

$$P_t = \frac{P_i}{B} + P_p + 500\ W = \mathbf{7828.3\ W} \tag{24}$$

This obtained value will remain the absolute minimum power required by the UAV to sustain level, static, hovering flight. All further calculations involving vertical and forward flight will be carried out using this value as the benchmark. Furthermore, in order to justify the credibility of this result, it is validated in Sec. 10.9. In order to study the variation of the blade and other parameters on the Total Hover power, the following plots are shown below:

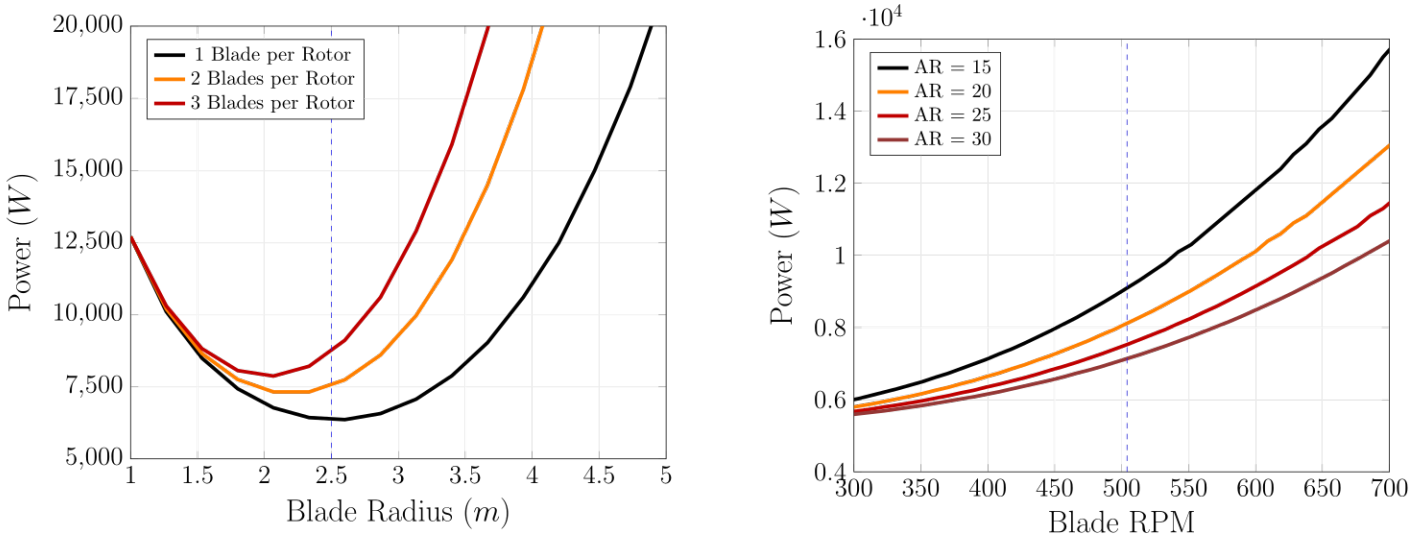

Figure 20: Variation of Power with Blade Radius & RPM

Fig. 20a shows that as the radius of the propeller blades increases, the total power consumption decreases

until it reaches a minimum value, after which it increases with increasing radius. The dotted blue line indicates the chosen blade radius of 2.5 m. As the radius increases, the induced power decreases as the induced velocity also decreases proportionally. However, after the minimum value, the profile drag becomes more significant as the radius is raised to power 4 in Eq. 23. The radius of minimum power also varies with the number of blades per motor. For the chosen configuration (2 blades per rotor), the chosen blade radius (r = 2.5 m) appears near the minima of the total Power required. Furthermore, while increasing the number of blades does increase the thrust produced, it also increases the power required to spin the blades and sustain hovering flight.

On the other hand, Fig. 20a illustrates the variation of total power with Propeller RPM with varying blade aspect ratios. The RPM is varied from a value lower than the hover RPM until the maximum attainable RPM before the blade tip enters the transonic region. The dotted blue line indicates hovering RPM. The graph shows that the total power consumption increases with RPM. Moreover, as the aspect ratio increases, the blade chord length decreases, and while this reduces the total power consumed, it also decreases the thrust produced by the blades.

10.8 Performance and Aerodynamic parameters

Quantities such as power and thrust are often written in non-dimensional units in order to facilitate comparisons and validate the data with existing performance charts. These are good indications of the rotor-craft characteristics during various stages of flight. Moreover, multiple parameters exist that represent the performance and determine the relative efficiency of the motor and propellers in their current operating state. The hover parameters are provided in Tab. 6.

Parameter	**Expression**	**Value**
Thrust Coefficient, C_T	$T/(\rho A_e(R_e\Omega_{hover})^2)$	0.0325
Blade Solidity, σ	$bc/\pi R$	0.0509
Power Coefficient, C_P	$P_t/(\rho A_e(R_e\Omega_{hover})^3)$	0.0066
Induced Power Coefficient,C_{P_i}	$P_i/(\rho A_e B(R_e\Omega_{hover})^3)$	0.0042
Power-Solidity Ratio, CPS	C_P/σ	0.1305
Power Loading, PL	C_T/C_P	4.89
Disk Loading, DL	$T/(2 \times A)$	6.6132 N/m^2
Inflow Ratio, λ	$\sqrt{C_T/2}$ or $v_{i_h}/(\Omega_{hover}R)$	≈ 0.11
Figure of Merit, FOM	$C_T^{3/2}/(\sqrt{2}C_P)$ [45]	≈ 0.6234

Table 6: Hover performance and Aerodynamic parameters

One inference that can be drawn from the table is that both the thrust and power coefficients for the coaxial configuration are higher than their expected values on Earth by an order of 1 significant figure. This is because the density on Mars is significantly lesser than on Earth. Subsequently, if the coefficients have to be maintained around their values on Earth, other variables, such as the blade radius or the angular velocity, will have to be significantly compromised. The former would affect weight and stowage considerations while increasing the latter would result in the formation of shock waves that would significantly increase the drag produced by the blades. Hence, a reasonable compromise between all the parameters had to be achieved using such an iterative procedure.

The disk loading, a parameter that affects hover efficiency, and blade solidity ratio, for example, are extremely important when comparing the performance of two different configurations.

While operating in a hover state, the figure of Merit (FOM) is a useful measure of hover efficiency. It is defined as the ideal power required by the actual power required during hover, and it represents how well a propeller/rotor configuration is implemented. On Earth, the typical values for a helicopter can vary anywhere between 0.6 (standard value) all the way to 0.9 for very well-designed rotors. In our case, the obtained value of 0.6234 indicates the difficulty of designing a good configuration for the Martian conditions.

10.9 Validation

In order to validate whether our initial approximations matched with theory, comparisons were made with values obtained from an online technical calculator providing helicopter performance parameters [46].

Parameter	**Calculated (Momentum Theory)**	**Reference Calculator [46]**	**Error (%)**
Induced velocity, v_{i_h}	18.7924 m/s	18.757 m/s	0.2 %
Total Power (Hover), P_i	7823 W	8426.4 W	7.8 %

Table 7: Hover Parameters Validation

The difference between the Total Power values can be accounted for by the Tail rotor power being included in the calculator, which accounts for approximately 10% of the total hower power in most conventional helicopters [42]. Subsequently, it can be seen that both the calculated induced velocity and total UAV power during hover are in excellent agreement with the values obtained from the calculator. Hence, it was decided that we would progress with these results.

10.10 Vertical Flight

Vertical flight consists of hover (V=0), climb (V>0), and descent (V<0), where V represents the rate of climb. The total power of a UAV during these stages will consist of a combined induced and climbing power, profile power and the other sources of power losses discussed in Sec. 10.7. Intuitively, it can be inferred that the total power required for climb, for any rate of climb, will be greater than the total hover power.

Climb in a helicopter is induced by excess power produced by the motor over the total power required for hovering. There are two main ways to attain this excess power. The most straightforward way is to vary the RPM of the motor. However, it is assumed that during all stages of the mission profile, the motor operates at its RPM of peak efficiency, which for most motors lies approximately at 55-70% of its maximum RPM. Varying the RPM will deviate from the RPM for peak efficiency, resulting in higher power losses. Subsequently, an alternate method is used where the blade angle of attack is varied.

$$\theta = \alpha + \lambda = \alpha + tan^{-1}\left(\frac{v_{i_h}}{\Omega_{hover} R}\right) \tag{25}$$

Eq. 25 [41] represents the total blade pitch angle (θ) in terms of the blade angle of attack (α) and the inflow ratio (λ) during hover. For the hover conditions, the blade pitch angle is calculated to be approximately 14° as the blade angle of attack was set to be 6° (for hover), which is the optimum blade AoA as set in most helicopters from the airfoil study considerations. As in any free-flying helicopter, the blade pitch angle is made to be constant. As shown in Fig. 16, decreasing the blade angle of attack will reduce the lift coefficient, hence also reducing the thrust produced as per Eq. 18. Consequently, in order to maintain the blade pitch angle, the inflow ratio has to increase, as is achieved by attaining a finite climb rate value and increasing the inflow ratio into the propeller by inducing vertical climbing flight. The opposite is true for descent. Eq. 26 represents the total blade pitch angle for descending flight.

$$\theta = \alpha + tan^{-1}\left(\frac{V + v_i}{\Omega_{hover} R}\right) \tag{26}$$

From the momentum theory, the induced velocity (v_i) and the rate of climb for climb at any angle of attack can be determined:

$$v_i = \frac{v_{i_h}^2}{V + v_i} = \frac{v_{i_h}^2}{tan\,(\theta - \alpha)\,\Omega_{hover} R} \tag{27}$$

In all of the previous expressions, the rate of descent is simply the negative value of the rate of climb (V). The variation in the Rate of Climb/Descent (V) with varying angles of attack is shown in Fig. 21.

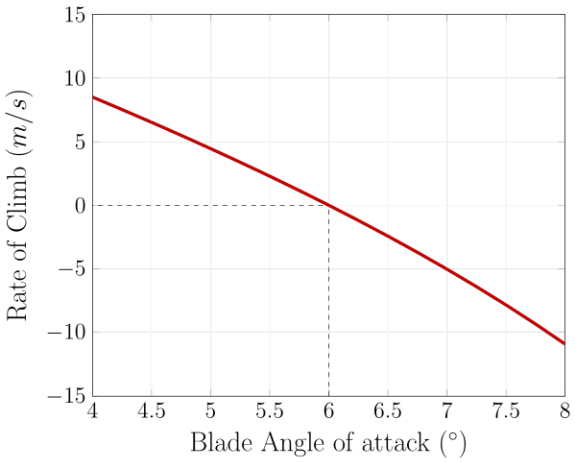

Figure 21: Rate of Climb v/s Blade Angle of Attack

During climbing or descending flight, the profile power remains relatively unchanged (as the RPM is unaltered), while the induced power (P_{i_c}) now additionally constitutes climb power. The total power is represented as:

$$P_t = P_{i_c} + P_p + 200 = T_h(V + v_i) + \rho bcR^4\Omega^3 C_D + 500\,W \tag{28}$$

The variation of the different components of the total power with changing rate of climb is shown in the following graph.

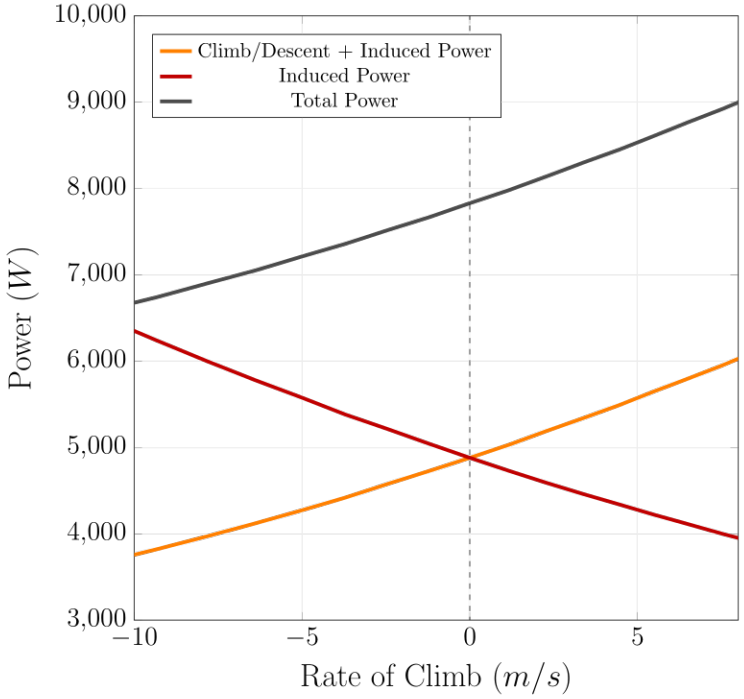

Figure 22: Power consumption v/s Rate of Climb

It can be observed that as the rate of climb increases, the total power also increases with a large increase in the climb power, compensating for the reduction in the induced power. The induced power decreases as the induced velocity decreases. During descent, the free stream velocity is directed upwards. Hence, the induced velocity drastically increases to compensate, thus increasing the induced power. However, during descent, the rotor extracts power from the airstream in excess of the induced power in a flow condition known as the windmill brake state. The different states of operation of a helicopter in vertical flight are elaborated further while analysing the limitations of the momentum theory in Sec. 10.14.

The rate of climb or descent can be varied depending on the type of sortie required or the nature of the mission profile. This is discussed in Sec. 16. As mentioned earlier, the rate of climb effectively depends upon the amount of excess power (ΔP) that the motor can produce during its operation. In later sections, the nature of the motor and its specifications are provided in detail. Until then, it is assumed that the motor produces enough power to sustain vertical non-level flight at a relatively high rate of climbs (≈ 10 m/s), as shown in Fig. 22. The analytical approximation, Eq. 29, can be used to determine the rate of climb as a function of only the excess power produced by the motor [3].

$$V = \frac{\Delta P}{T_h} \frac{\left(2v_{i_h} + \frac{\Delta P}{T_h}\right)}{\left(v_{i_h} + \frac{\Delta P}{T_h}\right)} \tag{29}$$

This is compared with the Rate of climb observed by varying the angle of attack from our previous formulations (Eq. 27).

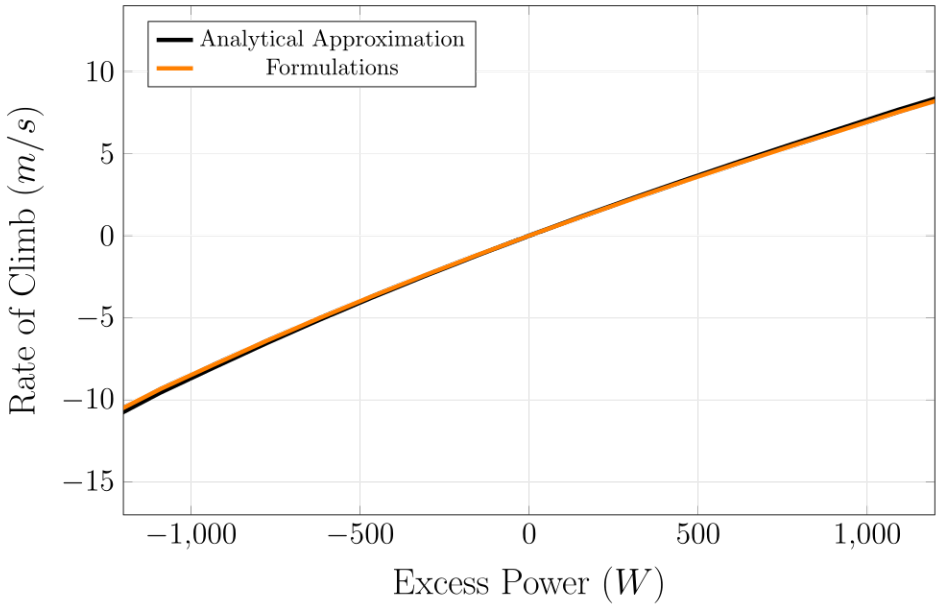

Figure 23: Rate of Climb v/s Excess Power

It can be seen that both the approximation and the lengthy formulations involving the induced velocities are in exceptionally close agreement with each other, subsequently validating the accuracy of the methodology.

As mentioned previously, reducing the angle of attack will reduce the thrust generated by the propellers as the lift coefficient decreases. Hence, the climbing thrust (T_{cl}) will be less than hovering thrust (T_h), while climbing power (P_{cl}) will be higher than hovering power (P_h). The expression governing the ratio of climbing to hover power is shown below [47].

$$\frac{P_{cl}}{P_h} = \left(\frac{v_i + V}{v_{i_h}}\right)\left(\frac{T_{cl}}{T_h}\right) \tag{30}$$

The ratio climbing to hovering thrust can be determined by finding the thrust produced by the propellers at different blade angles at attack by using the airfoil lift curve slope Fig. 16. The variation of the climbing power to hovering power ratio for different rates of climbs is shown in Fig. 24*b*.

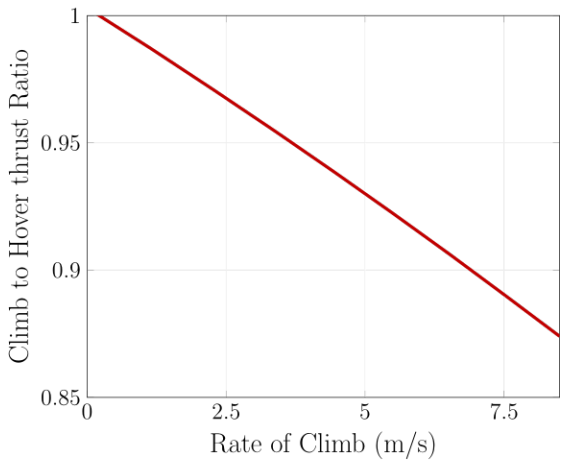

(a) Thrust Ratio

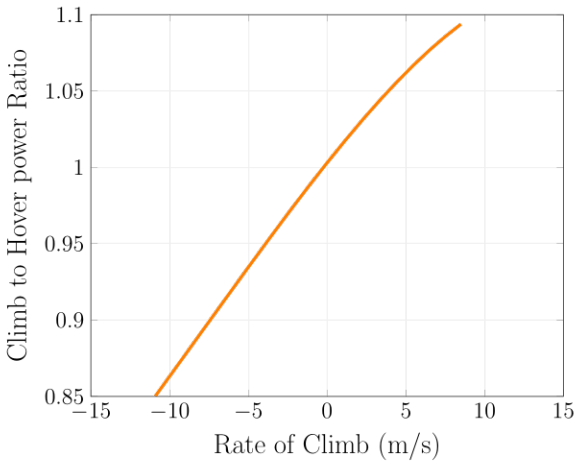

(b) Power Ratio

Figure 24: Thrust & Power Ratio v/s Rate of Climb

Fig. 24 shows that as the angle of attack decreases and the rate of climb increases, the thrust ratio decreases as expected due to decreasing lift coefficient. The power ratio plot (Fig. 24*b*) can be especially useful during the motor and battery selection stage, where the ideal rate of climb can also be finalised.

Throughout the analysis of vertical flight, the decrease in density with increasing altitude is not considered as the variation of density within the short 100 m traverse is insignificant. Subsequently, the density is assumed to be constant throughout ($\rho = 0.015\ kg/m^3$). Furthermore, in our calculations, although the power consumed during the mission profile's descent phase is determined similarly to that used to determine climbing power, there are certain drawbacks associated with this method. This will be evaluated in detail in the Limitations Sec. 10.14.

10.11 Autorotation

Conventional helicopters can still land their craft safely upon the loss of engine power through autorotative techniques. In this state of flight, rather than the propellers pushing air downwards in order to generate thrust, the propellers are oriented in a state such that they rotate by the action of air moving upwards through it such that it operates like an autogyro. While this is generally only employed in emergencies, it can be considered a viable option to facilitate the descent of our UAV, simultaneously saving energy. While for the mission profile, we still incorporate the values generated in Sec. 10.10, the auto-rotative performance of our UAV can still be considered and calculated for reference. During the autorotative descent stage, the rotor operates partially in a 'vortex ring state', where the vertical (descent) velocity is lower than the induced velocity, and partially in the 'windmill brake state', where there exists an upwash and the rotor absorbs more torque from the air, which is then expended in the form of profile drag [41]. Since the formulations involved in determining the auto-rotative performance are lengthy and require the exact radial and spanwise velocity distributions over the theoretical actuator disc, an online calculator [48] is used to estimate the performance. The following equations are implemented in the calculator.

$$2\pi\Big[\theta + \phi\Big] \times sin\phi = C_D cos\phi \qquad r = 0.65R \tag{31}$$

$$\Omega^2 r^2 + (v_z - v_i)^2 = V^2 \qquad tan\phi = \frac{v_z - v_i}{\Omega r} \tag{32}$$

$$0.9 \times M = \frac{\rho R b V^2}{2}\Big[2\pi(\theta + \phi)cos\phi + C_D sin\phi\Big] \tag{33}$$

Where θ represents the total blade pitch, λ is the inflow ratio, C_D is the blade mean drag coefficient and is assumed to be 0.043 from Fig. 18, v_z represents the descent rate, while v_i is the induced velocity. Ω represents the angular velocity of the propeller blades, b, the number of blades, and M is the mass of the UAV on Mars.

Through these calculations, once our input values are substituted, the values obtained for the descent rate and propeller speed for steady autorotative descent are 22.2 m/s and 600 RPM. These values represent an extremely steep descent in order to maintain a stable descent without power. Since our mission profile only requires operation to an altitude of 100 m, it is not high enough to ensure that auto-rotative techniques to save power become viable. Subsequently, the values obtained in Sec. 10.10 for descending flight are still considered for the energy balance of the UAV.

10.12 Forward Flight

During level forward flight, the increase in parasitic power (P_P) and the slight increase in profile power (P_O) is compensated by the decrease in induced power of the UAV such that the forward flight consumes less power than during pure hover. Typically, the minimum consumed by the helicopter occurs during a particular value of forward flight speed. While forward flight is not included in the core mission profile, it is still imperative to determine the performance of the UAV in forward flight, which may arise due to changed mission profiles or any untoward emergencies that may instigate a change in the landing spot.

The induced power in forward flight is the power required to accelerate air downward to create a force normal to the flight path. In forward flight, the resultant velocity (V') of the induced (v_i) and forward (V) velocities can be obtained using the following relation:

$$V' = \sqrt{(V - v_i sin\alpha)^2 + (v_i cos\alpha))} \tag{34}$$

Where α represents the angle of attack of the blades. The induced power equation can be derived from the above equation and non-dimensionalized, including the induced velocity at hover term (v_{i_h}) as follows:

$$\Big(\frac{v_i}{v_{i_h}}\Big)^4 - 2\Big(v\frac{v_i}{v_{i_h}}\Big)^3 \times \Big(\frac{V}{v_{i_h}}\Big)sin\alpha + \Big(\frac{v_i}{v_{i_h}}\Big)^2\Big(\frac{V}{v_{i_h}}\Big)^2 = 1 \tag{35}$$

The above equation is a representation of Wald's equation [49], which though can be solved for the induced velocity, is not straightforward. Subsequently, a major simplification which can be carried out is assuming the angle of attack to be equal to 0 ($\alpha = 0°$). The simplified expression for the induced velocity with

respect to the forward velocity (V) and the thrust produced (T) is shown below:

$$v_i = \left[\frac{-V^2}{2} + \sqrt{(\frac{V^2}{2})^2 + (\frac{T}{2\rho A})^2}\right]^{1/2} \tag{36}$$

The induced power during forward flight for the respective induced velocity value can be calculated using Eq. 14. The expression for the profile power (P_O) of the UAV during forward flight is obtained by modifying Eq. 23 to include the approximation for the normal component of the velocity in the form of the advance ratio (λ).

$$\lambda = \frac{V}{\Omega \times r_e} \tag{37}$$

$$P_O = \left[\rho b c R_e^4 \Omega^3 C_D\right](1 + 4.65\lambda^2) \tag{38}$$

Subsequently, after including the allowance due to compressibility, viscous, parasite power, and other losses, the complete expression for the total power (P_t) generated by the UAV becomes:

$$P_t = P_i + P_O + 500\ W = Tv_i + \left[\rho b c R_e^4 \Omega^3 C_D\right](1 + 4.65\lambda^2) + 500\ W \tag{39}$$

The plot of the total power consumed by the helicopter at different forward speeds is shown below. It can be inferred that the total power decreases as the forward speed increases. Even though the profile power increases, the decrease in induced power compensates for this increase in P_O. Subsequently, it is proven that forward flight consumes less power than a purely hovering flight. When Fig. 25 is extrapolated with velocity, a minimum power velocity ($V_{P_{min}}$) can be found. This is the point at which the decrease in induced power no longer compensates for the increase in profile power due to increasing forward speed. It is important to note that for this study, all other sources of power are assumed to be constant with forward flight. It can be deduced from Fig. 25 that the minimum power for the UAV, approximately 5900 W, occurs at a forward velocity of 42 m/s.

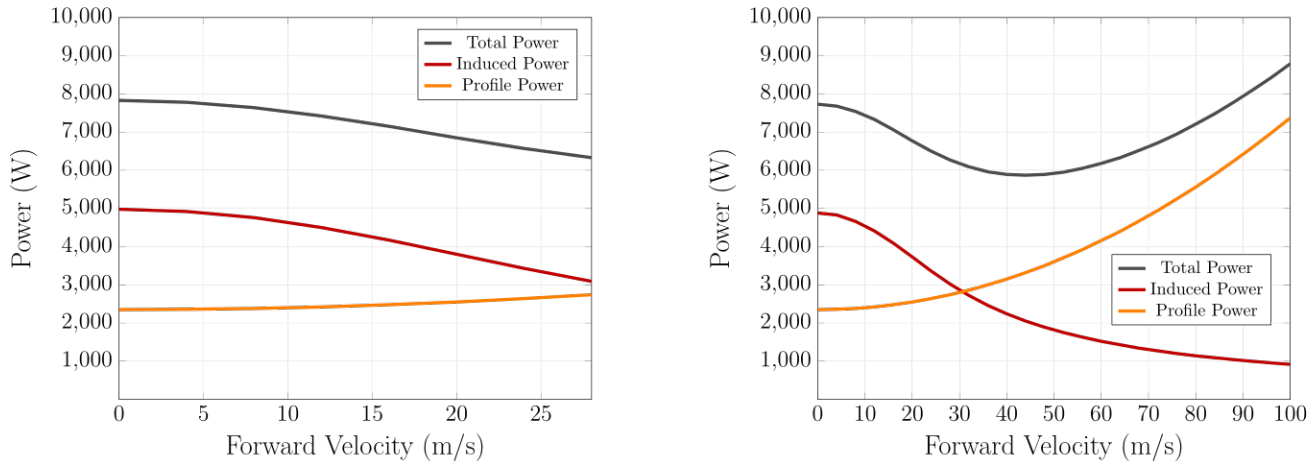

Figure 25: Variation of Total Power with Forward Velocity

Based on these calculations for power consumed during forward flight, and after considering the energy balance between the chosen motor, battery and the total energy available during one full sortie as carried

out in Sec. 16, the range and endurance of the UAV can be determined. Fig. 26 illustrates the variation of the range and the endurance of the UAV with forward velocity.

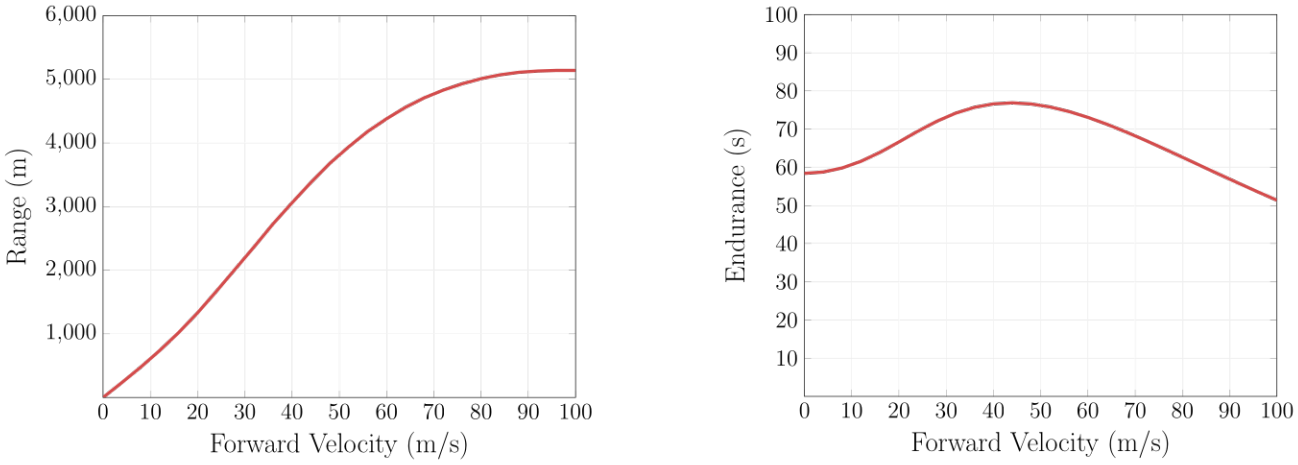

(a) Range

(b) Endurance

Figure 26: Variation of Range and Endurance with Forward Velocity

It is observed that the theoretical range of the UAV increases with forward speed. On the other hand, the calculated endurance of the UAV, is observed to increase until it reaches a maxima point, after which it decreases with forward velocity. The velocity of maximum endurance is numerically equivalent to the velocity of minimum power consumed ($V_{P_{min}}$).

10.13 Propeller Wake Analysis

A comprehensive turbo-machinery unsteady CFD analysis was carried out using the commercially available Simulia XFlow software in order to study the wake produced by the propeller blades in detail. The software comprises a Lattice-Boltzman method (LBM) based solver, which offers a high degree of flexibility and user operability. Unlike conventional CFD solvers and schemes, which use discretization and meshing techniques to iteratively solve the mass, momentum and energy conservation equations to determine the solution for the pressure/velocity fields at each time step, LBM considers fluid particles and models their propagation and collision over a discrete lattice. On the other hand, The Lattice-Boltzmann Method (LBM) tackles many of the drawbacks presented by the traditional CFD methods: the meshing process is removed as the simulation relies on an automatically generated lattice, which is organized in an Octree structure.

One advantage of this method was that the Large Eddy Simulation (LES) turbulence model could be implemented here at low computational costs. In industry, the Reynolds-Average Navier Stokes (RANS) Equations are used to model the turbulent flow, producing reasonably accurate results over a wide range of applications and flow conditions. LES and Direct Numerical Simulations (DNS) schemes are generally not preferred owing to the extreme computation cost required to run the simulations. However, since RANS models have limitations associated with the assumptions made to simplify the Navier-Stokes equation, and since LES simulations could be implemented here without sacrificing computational resources, the Large Eddy Simulation (LES) model was implemented. LES simulations are characterised by considerably lower time steps and higher resolving scales than RANS simulations. The mathematical formulation of the

Boltzmann transport equation is naturally straightforward to resolve numerically and is shown below:

$$\nu_t = \Delta_f^2 \frac{\left(G_{\alpha\beta}^d G_{\alpha\beta}^d\right)^{3/2}}{(S_{\alpha\beta}S_{\alpha\beta})^{5/2} + \left(G_{\alpha\beta}^d G_{\alpha\beta}^d\right)^{5/4}} \tag{40}$$

$$S_{\alpha\beta} = \frac{g_{\alpha\beta} + g_{\beta\alpha}}{2} \tag{41}$$

$$G_{\alpha\beta}^d = \frac{1}{2}\left(g_{\alpha\beta}^2 + g_{\beta\alpha}^2\right) - \frac{1}{3}\delta_{\alpha\beta}g_{\gamma\gamma}^2 \tag{42}$$

$$g_{\alpha\beta} = \frac{\partial u_\alpha}{\partial x_\beta} \tag{43}$$

Using Solidworks, a geometry consisting of some of the important structural elements, such as the propeller blades and the pod, as shown in Fig. 27a, was constructed and imported to XFlow. XFlow uses wall functions to model the near-wall region and boundary layer and employs the Wall-Modeled LES approach (WMLES). The unsteady simulation was carried out with both sets of propeller blades spinning in opposite directions at 550 RPM. The reference density, temperature and dynamic viscosity were assumed to be 288K, $0.015kg/m^3$ and $1.24 \times 10^{-5}\ Pa.s$, respectively. The numerical study was carried out after approximately 30 complete propeller blade rotations in order to develop the flow field fully. The velocity and pressure fields were captured and shown in Fig. 27b and Fig. 28c.

This CFD analysis was carried out for three primary reasons. Firstly, the flow visualisations allowed the validation of sensor placement on the UAV. Secondly, visualising the velocity/pressure contours and the wake interactions (Fig. 28d) between the blades and the pod aided in the aerodynamic optimisation of the shape of the Pod for future storage and other calculations. Thirdly, this numerical analysis could be used to validate some of the performance results obtained using analytical and empirical means.

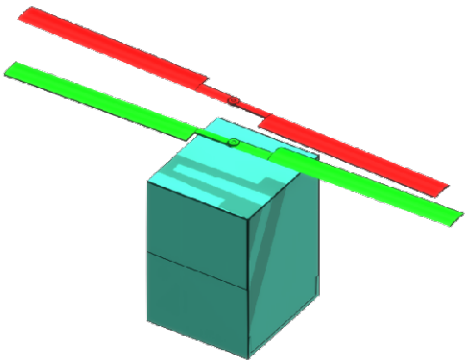

(a) Simulation Model

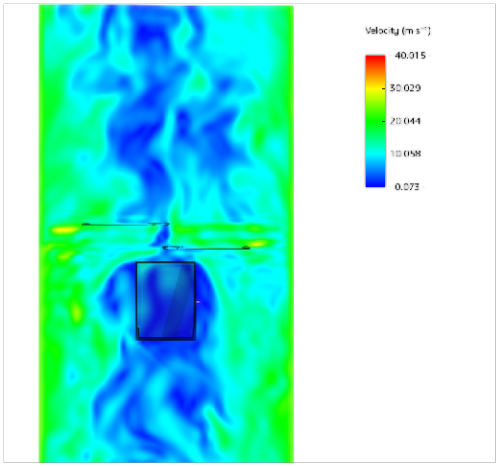

(b) Induced Velocity

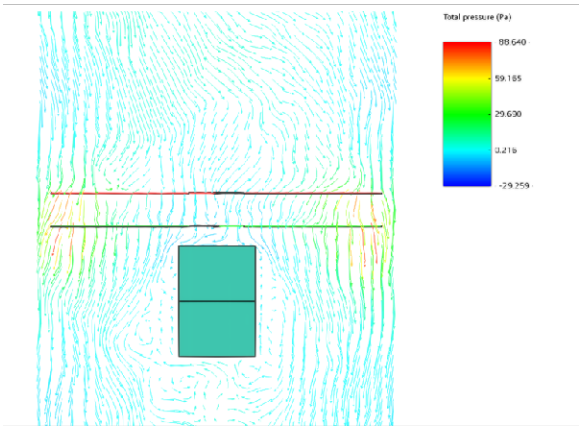

(c) Total Pressure

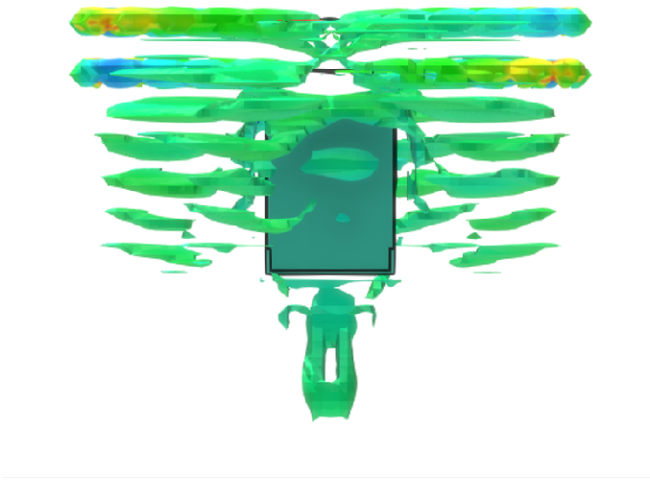

(d) Vortex Core Region

Figure 28: CFD Results

In Sec. 10.7, the value of the induced velocity for the effective single rotor was calculated to be 18.8 m/s ($\approx 19m/s$). This value represents the flow velocity obtained directly under and within the vicinity of the spinning propellers. As inferred from the induced velocity plot in Fig. 27b, the induced flow velocity appears to be around 20m/s, hence validating our analytical performance calculations.

10.14 Limitations

This section addresses some of the limitations present in our study till this stage. This includes some potential disadvantages with the chosen configuration, methodology employed, etc.

- One of the main problems associated with the Coaxial configuration is the mechanical complexity of the rotor, the flag hinges and the rotor hub. The swash plates and rotor linkage elements must be assembled at the top of the rotor shaft as they are required to drive the two rotors in opposite directions. The intricate and compounded mechanism makes the components more susceptible to mechanical failure.
- Aerodynamic issues that are usually associated with Coaxial rotors include swirl recovery, solidity effects and load sharing between the rotors [36].
- One of the limitations in the methodology implemented to determine vertical flight performance is the use of momentum theory for low rates of descent. This can be elaborated graphically using a plot of normalized induced velocity plotted against the normalized climb velocity as shown in Fig. 29.

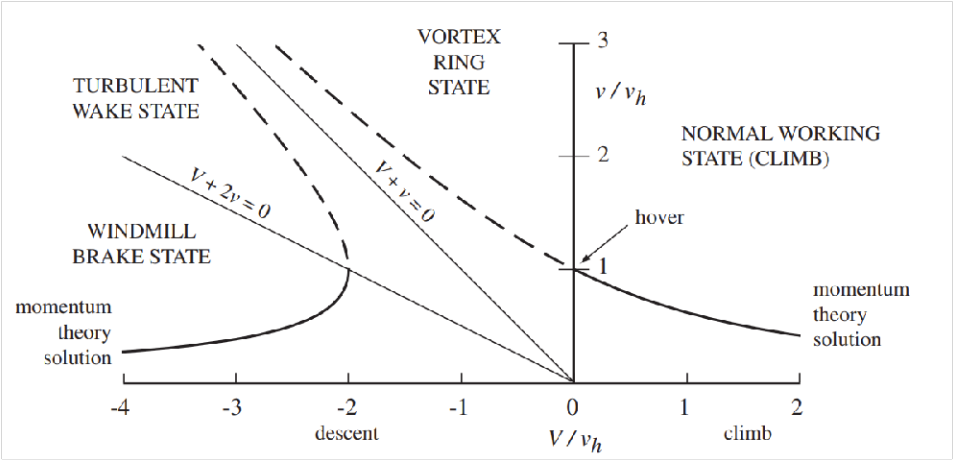

Figure 29: Momentum Theory results in Vertical Flight [3]

According to the normalized rate of descent (ROD), the operation of the rotors can be classified into the vortex ring state, the turbulent wake state and the windmill brake state. At low ROD, the flow through the disc and in the propeller wake is downwards, while the flow outside the slipstream is upwards, which is unrealistic. Subsequently, between values for the Rate of descent between 0 (hover) and $-2v_{i_h}$, as shown in the graph, the momentum theory fails to produce a realizable wake model that can be used to determine the performance of the UAV. Nevertheless, it was still used as it provides very good UAV performance estimations for the rotor in hover, climb and high rates of descent.

11 Stowage Analysis

In order to maximise the usage of the provided aeroshell, a folding mechanism is used for the propellers and the solar panel. By folding the propellers upwards, we are able to maximise the usage of the given 5 m aeroshell height.

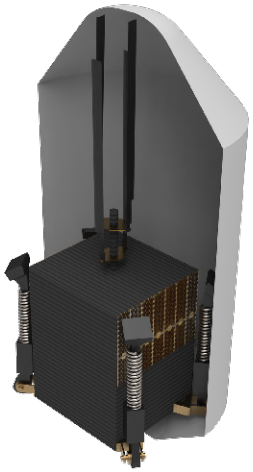

(a) UAV Stowage

(b) Dimensions of payload fairing

Along with the propellers, the solar panels are housed inside the pod itself. This is to ensure rapid panel deployment between sorties and house it safely inside during flights. A rolling shutter mechanism has been employed in order to protect the solar cells from the harsh Martian environment when they are stowed and to prevent airflow through the pod when the UAV is airborne.

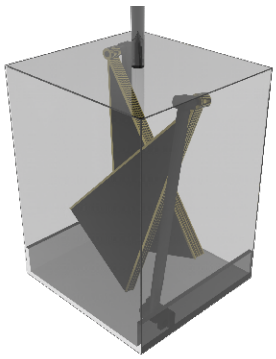

(a) Folded Solar Array

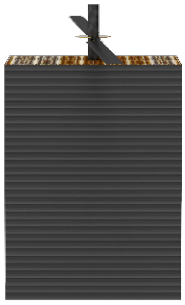

(b) Shutter Mechanism

Figure 31: Subsystems for stowage

12 Final Configuration

The final configuration of the UAV with solar panels deployed and stowed is illustrated in Fig. 32.

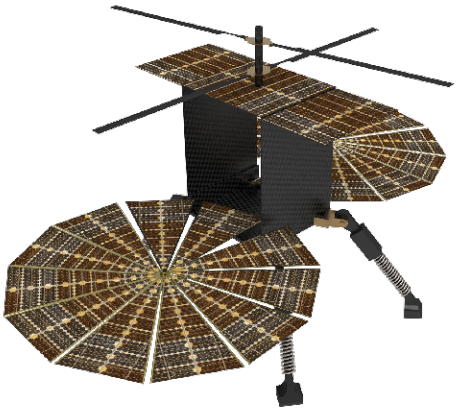

(a) UAV with Solar Panels Deployed

(b) UAV with Solar Panels Stowed

Figure 32: Final UAV Configuration

13 Structural Analysis

The design and construction of a UAV for operation in the Martian atmosphere necessitate an intricate balance between structural integrity and mission-specific requirements. Mars presents an array of formidable environmental challenges, including an atmosphere composed predominantly of carbon dioxide (95.3%) with a surface pressure of only about 610 Pascals, roughly 0.6% of Earth's sea-level pressure. This tenuous atmosphere demands a UAV design capable of generating sufficient lift while minimising structural mass to enhance flight efficiency. Additionally, the extreme diurnal temperature fluctuations, ranging from -125°C at night to 20°C during the day, impose severe thermal stresses on the structural materials, necessitating the use of materials with high thermal stability and low thermal expansion coefficients.

The primary requirement for our UAV is to maintain a rigid yet lightweight structure, ensuring it can endure the mechanical loads encountered during takeoff, flight, and landing while also adhering to the

spatial constraint of fitting the entire craft within a 2.5-meter diameter aeroshell. This dimensional limitation necessitates a compact design, with innovative approaches to material selection and structural configuration to optimise both weight and strength. The UAV must also be capable of multiple flights on the Martian surface, requiring a landing gear system that absorbs impact forces effectively and provides durability across several landing cycles. This demands careful consideration of fatigue resistance, energy dissipation, and material resilience to ensure mission longevity.

Through a rigorous design process, our goal is to develop a UAV structure that can withstand unique Martian conditions while meeting all mission-critical requirements, including structural rigidity, weight minimisation, and reliable landing gear performance.

13.1 Design Methodology

The design of our UAV's structure began with an extensive literature review to evaluate potential materials that could meet the stringent requirements of Martian operations. Our primary focus was identifying materials that could balance strength, weight, thermal stability, and resistance to environmental stressors.

We first considered traditional aerospace materials, such as aluminium alloys, titanium alloys, and high-strength steels. These metals are known for their exceptional strength-to-weight ratios, fatigue resistance, and thermal conductivity. However, despite these advantages, metals and alloys were ultimately deemed unsuitable for this specific application due to their relatively high density, which would have resulted in a significant increase in the overall mass of the UAV. This added weight would have directly impacted the craft's ability to generate sufficient lift in the thin Martian atmosphere and reduced the overall efficiency of multiple flight operations.

Additionally, metals are prone to thermal expansion and contraction under the extreme temperature variations on Mars, which could lead to material fatigue and potential structural failure over multiple flights.

Steel, while known for its exceptional strength and durability, has a significant drawback due to its high density, which makes it an impractical choice for aerospace applications where weight is a critical factor. The density of steel typically ranges from 7.75 to 8.05 g/cm^3, which would significantly increase the overall mass of the UAV, thereby reducing its flight efficiency in Mars' thin atmosphere. Another critical consideration is steel's Ductile-to-Brittle Transition Temperature (DBTT). The DBTT for most steels is around -50°C to -100°C, which is well within the range of Martian surface temperatures. Below this temperature, steel can become brittle, increasing the risk of fracture under mechanical stress or impact during landing, making it unsuitable for the harsh Martian environment.

In contrast, aluminium and its alloys are well-suited for low-temperature applications, as they maintain their ductility and strength even in extremely cold conditions. Unlike many metals, aluminium does not become brittle at low temperatures; its mechanical properties improve as the temperature decreases. This characteristic makes aluminium an excellent material choice for components that must endure

the cold Martian nights. However, despite its advantages in low-temperature performance, aluminium was ultimately not chosen due to the availability of even lighter and more thermally stable composite materials, which better meet the specific demands of our UAV design.

Given these considerations, we turned our attention to composite materials, which offer significant advantages in terms of weight reduction and thermal stability. After evaluating various composite options, we selected carbon fibre reinforced polymer (CFRP) with an aluminium honeycomb core for the construction of the UAV's pod, which houses all critical components, including the RTG, motors, avionics, and sensors. Carbon fibre provides an exceptional strength-to-weight ratio, surpassing that of metals, while the aluminium honeycomb core adds rigidity and impact resistance without adding excessive weight. This combination ensures that the pod is both lightweight and capable of withstanding the mechanical stresses encountered during Martian flight and landing operations.

Furthermore, carbon fibre exhibits excellent thermal stability and low thermal expansion, which minimises the risk of structural deformation due to temperature fluctuations. The low thermal conductivity of the composite material also acts as a protective barrier for the internal components, maintaining a stable internal environment despite the extremes in the external temperature. By choosing this material configuration, we ensured that the UAV's structural design would meet all mission requirements while optimising for performance, durability, and longevity on the Martian surface.

13.2 Manufacturability

The manufacturing of the UAV pod, which serves as the primary housing for all critical components, involves the construction of a sandwich panel with a total thickness of 10 mm. This panel consists of an 8 mm aluminium honeycomb core flanked by 1 mm layers of carbon fibre on each side. The core material is made from 5052-grade aluminium alloy, chosen for its excellent strength-to-weight ratio and corrosion resistance, with a density of 76.9 kg/m^3 and a cell size of 3.2 mm (1/8"). The small cell size enhances the structural rigidity and impact resistance of the core, making it ideal for aerospace applications where weight reduction without compromising strength is paramount.

The carbon fibre used in this structure is sourced from TeXtreme, which is known for its unique fibre architecture and offers significant advantages in weight savings and laminate thickness optimisation. This is particularly beneficial in UAV applications, where minimising mass while maintaining structural integrity is critical. The TeXtreme carbon fibre's thin-ply technology is crucial in suppressing microcracking, a common issue in composite materials subjected to repeated stress and extreme temperature variations. The "thin-ply effect" reduces the likelihood of composite failure, ensuring the longevity and reliability of the UAV's structure.

This advanced material approach has a proven track record, as it was employed in NASA's Ingenuity helicopter, the first aircraft to achieve powered flight on Mars. The use of TeXtreme's carbon fibre in Ingenuity's construction was instrumental in meeting the demanding requirements of the Martian environment. By utilising the same TeXtreme carbon fibre in our UAV design, we are leveraging

cutting-edge aerospace technology that has already demonstrated its effectiveness in the Martian atmosphere. This provides confidence in the material's performance and aligns our design with the proven methodologies of interplanetary exploration.

The manufacturing process involves precise layering and bonding of the carbon fibre with the aluminium honeycomb core, followed by a curing process to achieve the desired mechanical properties. The application of TeXtreme's carbon fibre not only enhances the structural performance of the UAV pod but also provides superior resistance to the large mechanical loads induced by the Martian climate. Mars' extreme temperature variations exert significant thermal stress on exposed composite structures, but the incorporation of TeXtreme materials substantially mitigates the risk of microcrack formation, ensuring longer-lasting and more durable components. This advanced composite construction method allows for the creation of a lightweight yet robust pod optimised for the demanding conditions of Martian exploration.

13.3 Landing Gear Considerations and Design

The design of the landing gear is a critical aspect of the UAV, as it must effectively manage the impact forces during landing while minimising the risk of toppling. The UAV, with a mass of 70 kg, descends at a velocity of 2 m/s, which requires the landing gear to sustain the resulting impact forces without failure or excessive deformation. To meet these demands, the landing gear must be both robust and lightweight, ensuring that it does not compromise the overall weight efficiency of the UAV.

After evaluating various materials, Ti-6Al-4V titanium alloy was selected for the landing gear due to its high strength-to-weight ratio, excellent fatigue resistance, and corrosion resistance. Ti-6Al-4V is well-suited for aerospace applications where structural integrity under repeated loading conditions is crucial.

One traditional approach in aerospace design is the use of crushable honeycomb inserts made from aluminium or titanium [50]. These honeycomb structures are often integrated into landing gear struts to absorb impact energy by deforming upon landing, effectively reducing the forces transmitted to the main structure of the vehicle [51]. While this method is lightweight and highly effective at managing impact loads, it is unsuitable for our UAV due to the requirement for multiple sorties. The irreversible deformation of the honeycomb structure would necessitate replacement after each landing, which is not feasible in a mission requiring repeated operations.

Our design incorporates a damped strut system with built-in elastomeric dampers or springs to address this. This approach allows the landing gear to absorb and dissipate energy upon impact, reducing the risk of bouncing or toppling without the need for single-use components. The dampers work by compressing during landing, effectively managing the kinetic energy and preventing excessive force transmission to the UAV's structure. This reusable system ensures that the landing gear can perform consistently across multiple landings, providing both durability and reliability throughout the mission. By optimising the strut design with elastomeric dampers, we achieve a balance between weight efficiency and impact management, ensuring the UAV's safe operation on the Martian surface.

13.4 Damped Strut System Design

The damped strut system for the UAV landing gear is designed to effectively absorb and dissipate impact energy during landing, ensuring the structural integrity and stability of the UAV while minimising weight. The primary components of this system include the strut itself, constructed from Ti-6Al-4V, and the integrated elastomeric dampers and springs, which manage the kinetic energy generated during landing.

13.4.1 Strut Material and Structure

The strut is constructed from Ti-6Al-4V, a titanium alloy widely recognised for its high strength-to-weight ratio, exceptional fatigue resistance, and corrosion resistance. These properties make it ideal for aerospace applications where both performance and durability are critical. The strut design is tubular, providing the necessary structural stiffness while minimising weight. The tubular structure also allows for the integration of the damping mechanism within the strut, optimising the design for both impact absorption and compactness.

13.4.2 Elastomeric Dampers

The damper within the strut system is made from a high-performance elastomer, such as silicone rubber, chosen for its excellent energy absorption and resilience. Elastomers are particularly suited for damping applications due to their ability to deform under load and then return to their original shape, thereby dissipating energy in the form of heat. In this design, the elastomeric dampers are positioned inside the strut, between the inner and outer sections of the tubular structure. When the UAV lands, the strut compresses, causing the elastomeric dampers to deform and absorb the kinetic energy of the impact. This deformation helps to reduce the peak force transmitted to the UAV's body, thereby preventing excessive stress on the airframe and minimising the risk of toppling.

13.4.3 Spring Mechanism

In addition to the elastomeric dampers, the system incorporates coil springs, which are designed to work in tandem with the dampers. This spring is typically made from high-strength steel or titanium, chosen for its excellent fatigue resistance and ability to store and release energy efficiently. The springs are positioned in parallel with the elastomeric dampers, providing an additional layer of energy absorption. Upon impact, the springs compress along with the elastomeric dampers, further reducing the load on the UAV's structure. The springs also assist in returning the strut to its original position after the impact, ensuring that the landing gear is ready for subsequent landings without any manual reset.

13.4.4 Load Distribution and Redundancy

The combination of elastomeric dampers and springs allows for a highly effective load distribution across the landing gear system. By distributing the impact forces across multiple components, the design ensures that no single element bears the full brunt of the load, thereby enhancing the overall durability and reliability of the system. Additionally, this redundancy helps to safeguard against potential failure; if one component were to degrade or fail, the remaining elements would continue to provide adequate damping, maintaining the UAV's stability.

13.4.5 Housing and Integration

The entire damping system is housed within the Ti-6Al-4V strut, with precision-engineered interfaces between the strut, elastomeric dampers, and springs. The housing is designed to protect the damping components from environmental factors such as dust, temperature fluctuations, and Martian surface conditions. The interface between the damping components and the strut is optimised to ensure smooth operation, minimising friction and wear. Lubrication or coatings, such as PTFE (polytetrafluoroethylene), may be applied to reduce friction and enhance the lifespan of the moving parts.

13.5 Simulation

13.5.1 Pod

To ensure the structural integrity of the UAV pod during landing, we conducted a simulation using ANSYS Composite PrePost (ACP). This simulation aimed to accurately model the behaviour of the composite sandwich panel under the loading conditions expected during touchdown. The sandwich panel, which forms the primary structure of the pod, consists of carbon fibre layers on both sides of an aluminium honeycomb core.

The ACP simulation process began with the creation of individual plies, each representing a single layer of the composite material. For our design, we added eight plies of carbon fibre, each with a thickness of 0.13 mm, resulting in a total thickness of 1 mm. The plies were strategically oriented at 0° and 90° angles to optimise the structural stiffness and resistance to multidirectional loads. The aluminium honeycomb core, positioned between the carbon fibre layers, is 8 mm thick with a cell size of 3.2 mm. This honeycomb structure provides excellent rigidity and impact absorption, which is critical for withstanding the forces encountered during landing.

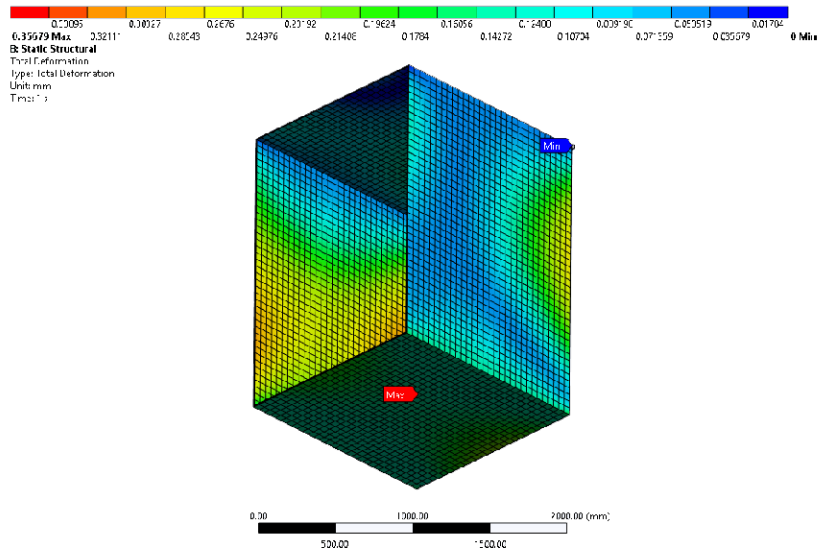

Figure 33: ACP Pod Simulation

After defining the plies, we created a stack representing the full laminate structure of the UAV pod. The stack was designed to replicate the actual construction, with the carbon fibre layers on the outer surfaces and the aluminium honeycomb core sandwiched in between. The stack was then subjected to simulated

landing conditions, replicating the forces generated by the UAV's 70 kg mass descending at 2 m/s.

Using ACP, we analysed the deformation of the composite structure. The simulation confirmed that the combination of carbon fibre plies and the aluminium honeycomb core could withstand the impact forces without compromising the pod's structural integrity.

By utilising ANSYS Composite PrePost for our simulation, we validated the design and material selection, ensuring that the UAV pod is both robust and reliable under the extreme conditions of Martian exploration.

13.5.2 Landing Gear

A structural analysis was conducted on the landing gear to assess its performance under the impact conditions expected during the landing. The analysis aimed to determine the deformation of the landing gear when subjected to the UAV's impact forces. Using finite element analysis (FEA), we applied the landing conditions to the model, where the UAV's mass of 70 kg was simulated, impacting the landing gear at a descent velocity of 2 m/s.

In the simulation, the bottom of the landing gear was held stationary to replicate the moment of contact with the Martian surface, effectively anchoring the gear to assess how it would respond to the impact. The analysis provided a maximum deformation value of 1.34 mm, which falls well within acceptable limits, ensuring that the landing gear maintains its structural integrity without excessive bending or permanent deformation.

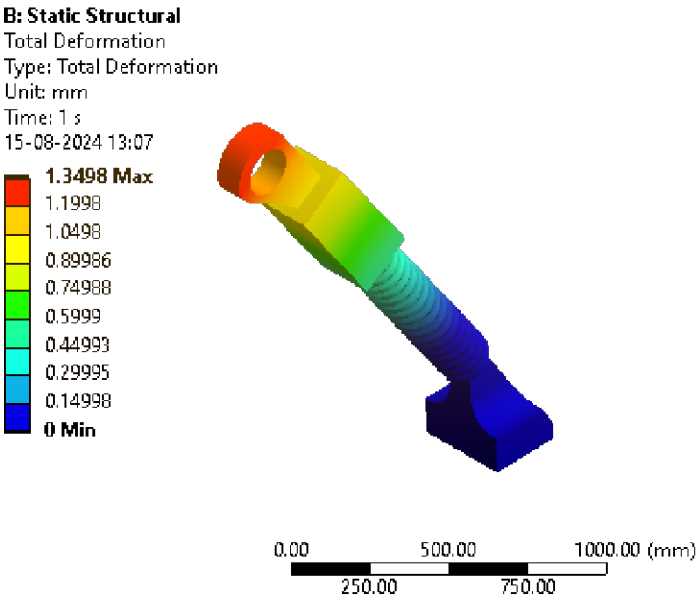

Figure 34: Landing Gear Deformation

The results of this analysis demonstrated that the landing gear can effectively absorb the impact energy, dissipate the forces throughout its structure, and prevent damage to the UAV's main body. The minimal deformation observed confirms that the selected materials and design choices, including the use of Ti-6Al-4V and the incorporation of elastomeric dampers, provide the necessary resilience and durability for repeated landings on Mars.

14 Flight Dynamics

14.1 Introduction

The aim of any flight dynamics modelling is to obtain correlations between the rotorcraft's motion and external forces and moments based on previously carried out aerodynamic and structural analyses. The flight dynamics model is not only the basis of the control system design but is also a powerful tool to simulate and, if required, improve the handling qualities of the rotorcraft. The flight dynamics model paints a complete picture of the capabilities and limitations of the platform. It can also highlight potential design vulnerabilities, allowing for these to be resolved without real-world testing.

Flight dynamic analyses include the prediction of trim states, stability characteristics and open-loop control response characteristics to pilot input and external disturbances. This section presents a literature survey on flight dynamic modelling of coaxial rotorcraft configurations.

14.2 Frames of Reference, Coordinate Transformations and Their Associated Kinematics

Before discussing the flight dynamic modelling methodology, it is imperative that the various frames of reference and their associated coordinate transformations be discussed. Further, the kinematics of the rotorcraft in each of the reference frames is explicated upon. The content in this section has been obtained from Ref. [52].

14.2.1 Inertial Frame of Reference

This section shall elucidate the equations of translational and rotational motion of a helicopter assumed to be a rigid body, subject to an axes system fixed at the centre of mass of the rotorcraft. These axes are elucidated in Fig. 35. These axes move with time-varying velocity components x, y, z and p, q, r under the action of the applied forces and moments X, Y, Z and L, M, N.

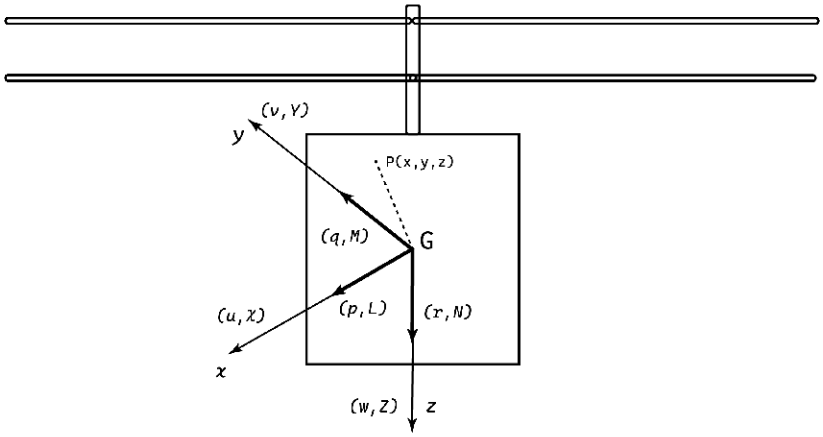

Figure 35: Body Fixed Frame

The preliminary equations of motion can be derived by equating the rates of change of the linear and angular momentum to the applied forces and moments. Assuming a constant mass, the equations can be constructed quite straightforwardly by selecting an arbitrary point P inside the pod and deriving the expression for the absolute acceleration at this point. This acceleration thus obtained can be integrated over the entire volume of the pod to derive the effective change in angular momentum and, hence, the total inertia force. Following a similar approach leads to the derivation of the angular acceleration and its corresponding inertial moment.

The centre of the moving axes is located at the rotorcraft's centre of mass, G. The centre of mass is assumed to be at a fixed position, and its variation due to the flapping and lagging motion of the rotor is neglected. We define the i, j, k unit vectors along the x, y, z directions respectively. We can derive the expression for the absolute acceleration of P relative to G and the acceleration of G relative to the planetary reference frame. This process is initiated by taking the position vector of the point P relative to G,

$$r_{p/g} = xi + yj + zk \tag{44}$$

The velocity can then be written as,

$$v_{p/g} = \dot{r}_{p/g} = (\dot{x}i + \dot{y}j + \dot{z}k) + (xi + yj + zk) \tag{45}$$

Due to the moving nature of the reference axes, the unit vectors change direction and, hence, will have corresponding time derivatives. These can be derived by considering small changes in the angles $\delta\theta$ about each of the axes.

$$\delta i = j\delta\theta_z - k\delta\theta_y \tag{46}$$

and,

$$\frac{di}{dt} = \dot{i} = j\frac{d\theta_z}{dt} - k\frac{d\theta_y}{dt} = rj - qk \tag{47}$$

Defining the angular velocity vector as,

$$\omega_g = pi + qj + rk \tag{48}$$

from Eq. 14.2.1, the unit vector derivative can be written as the vector product

$$\dot{i} = \omega_g \times i \tag{49}$$

this form is also applicable about the j and k axes. Due to the rigid-body assumption, the distance of the arbitrary point P from the centre of mass is fixed, and the velocity of P relative to G can be written as,

$$v_{p/g} = \omega_g \times r_p \tag{50}$$

or in an expanded form,

$$v_{p/g} = (qz - ry)i + (rx - pz)j + (py - qx)k = u_{p/g}i + v_{p/g}j + w_{p/g}k \tag{51}$$

Similarly the acceleration of P relative to G can be written as,

$$a_{p/g} = \dot{v}_{p/g} = \dot{u}_{p/g}i + \dot{v}_{p/g}j + \dot{w}_{p/g}k + u_{p/g}i + v_{p/g}j + w_{p/g} = a_{p/g_{rel}} + \omega_g \times v_p \tag{52}$$

expanding the above equation, we get,

$$a_{p/g} = (\dot{u}_{p/g} - rv_{p/g} + qw_{p/g})i + (\dot{v}_{p/g} - pw_{p/g} + ru_{p/g})j + (\dot{w}_{p/g} - qu_{p/g} + pv_{p/g})k \tag{53}$$

we can write the velocity of P relative to the planet reference as,

$$v_p = (u - ry + qz)i + (v - pz + rx)j + (w - qx + py)k \tag{54}$$

Similarly, acceleration takes the form,

$$a_p = a_{p_{rel}} + \omega_g \times v_p \tag{55}$$

or

$$a_p = a_x i + a_y j + a_z k \tag{56}$$

with components,

$$a_x = \dot{u} - rv + qw - x(q^2 + r^2) + y(pq - \dot{r}) + z(pr + \dot{q}) \tag{57}$$

$$a_y = \dot{v} - pw + ru - x(p^2 + r^2) + z(qr - \dot{p}) + x(pq + \dot{r}) \tag{58}$$

$$a_z = \dot{w} - qu + pv - z(p^2 + q^2) + x(pr - \dot{q}) + y(qr + \dot{p}) \tag{59}$$

These are the components of acceleration at point P (x, y, z) from the centre of mass when the velocity components are given by $u(t)$, $v(t)$, $w(t)$ and $p(t)$, $q(t)$, $r(t)$.

We can now assume that the sum of all the external forces acting on the aircraft can be written in component form such that they act on the centre of mass, given by,

$$F_g = Xi + Yj + Zk \tag{60}$$

If the material point P consists of an elemental mass dm, then the total inertia force acting on the pod is the sum of all elemental forces. Thus, the equations of motion take on elemental forms given by,

$$X = \int_{body} a_x dm \tag{61}$$

$$Y = \int_{body} a_y dm \tag{62}$$

$$Z = \int_{body} a_z dm \tag{63}$$

Since G is the centre of mass, then by definition,

$$\int_{body} x dm = \int_{body} y dm = \int_{body} z dm = 0 \tag{64}$$

and the mass of the rotorcraft is given by,

$$M_r = \int_{body} dm \tag{65}$$

The translational equations of motion of the rotorcraft are given by the relatively simple equations,

$$\begin{aligned} X &= M_r(\dot{u} - rv + qw) \\ Y &= M_r(\dot{v} - rv + qw) \\ Z &= M_r(\dot{w} - rv + qw) \end{aligned} \tag{66}$$

In addition to the linear acceleration of the centre of mass, the inertial loading is composed of centrifugal terms when the aircraft is manoeuvring with rotational motion. For the rotational motion itself, the external moment vector about the centre of mass can be written as,

$$M_g = Li + Mj + Nk \tag{67}$$

This integrated inertial moment can be written as,

$$\int_{body} = r_p \times a_p dm = \left[\int_{body} (ya_z - za_y)dm\right] i + \left[\int_{body} (za_x - xa_z)dm\right] j + \left[\int_{body} (xa_y - ya_x)dm\right] k \tag{68}$$

Taking into consideration the rolling motion about the x-axis, we obtain,

$$L = \int_{body} (ya_z - za_y)dm \tag{69}$$

Substituting for a_y and a_z we obtain,

$$\begin{aligned} L = \dot{p} \int_{body} (y^2 + z^2)dm - qr \int_{body} (z^2 - y^2)dm + (r^2 - q^2) \int_{body} yzdm \\ -(pq + \dot{r}) \int_{body} xzdm + (pr - \dot{q} \int_{body} xydm \end{aligned} \tag{70}$$

We can define the moments and the product (I_{xz}) of inertia as,

$$x\text{-axis: } I_{xx} = \int_{body} (y^2 + z^2) dm \tag{71}$$

$$y\text{-axis: } I_{yy} = \int_{body} (x^2 + z^2) dm \tag{72}$$

$$z\text{-axis: } I_{zz} = \int_{body} (x^2 + y^2) dm \tag{73}$$

$$xz\text{-axes: } I_{xz} = \int_{body} xz dm \tag{74}$$

The external moments can be equated to the inertial moments to obtain the rotational equations of motion of the rotorcraft.

$$\begin{aligned} L &= I_{xx}\dot{p} - (I_{yy} - I_{zz})qr - I_{xz}(pq + \dot{r}) \\ M &= I_{yy}\dot{q} - (I_{zz} - I_{xx})pr - I_{xz}(p^2 - r^2) \\ N &= I_{zz}\dot{r} - (I_{xx} - I_{yy})pq - I_{xz}(\dot{p} - rq) \end{aligned} \tag{75}$$

The product of inertia (I_{xz}) is applicable only when there is an asymmetry in pod geometry in the x-z plane. However, due to symmetry, even in the x-z plane, in our case, these equations reduce to,

$$\begin{aligned} L &= I_{xx}\dot{p} - (I_{yy} - I_{zz})qr \\ M &= I_{yy}\dot{q} - (I_{zz} - I_{xx})pr \\ N &= I_{zz}\dot{r} - (I_{xx} - I_{yy})pq \end{aligned} \tag{76}$$

14.2.2 Angular Orientation of the Rotorcraft

The rotorcraft can change its angular orientation by rotating about three independent directions. The standard sequence used in flight dynamics is yaw, ψ, pitch θ and roll, ϕ. This is represented in Fig. 36. We can consider a general initial position and rotate the pod about the z-axis (unite vector k_0) through the yaw angle ψ. The unit vectors in the rotated frame can be related to those in the original frame by the transformation Ψ.

$$\begin{bmatrix} i_1 \\ j_1 \\ k_0 \end{bmatrix} = \begin{bmatrix} cos\psi & sin\psi & 0 \\ -sin\psi & cos\psi & 0 \\ 0 & 0 & 1 \end{bmatrix} \begin{bmatrix} i_0 \\ j_0 \\ k_0 \end{bmatrix} \text{ or } \{b\} = \Psi\{a\} \tag{77}$$

Next, the pod is rotated about the new y-axis (unit vector j_1) through the pitch angle, θ.

$$\begin{bmatrix} i_2 \\ j_1 \\ k_1 \end{bmatrix} = \begin{bmatrix} cos\theta & 0 & -sin\theta \\ 0 & 1 & 0 \\ sin\theta & 0 & cos\theta \end{bmatrix} \begin{bmatrix} i_1 \\ j_1 \\ k_0 \end{bmatrix} \text{ or } \{c\} = \Theta\{b\} \tag{78}$$

Finally, the rotation about the x-axis through the roll angle ϕ and is given by,

$$\begin{bmatrix} i_2 \\ j_2 \\ k_2 \end{bmatrix} = \begin{bmatrix} 1 & 0 & 0 \\ 0 & cos\phi & sin\phi \\ 0 & -sin\phi & cos\phi \end{bmatrix} \begin{bmatrix} i_2 \\ j_1 \\ k_1 \end{bmatrix} \text{ or } \{d\} = \Phi\{c\} \tag{79}$$

Any arbitrary vector d in the new axes system can, therefore, be related to the components of the old axis system by,

$$\{d\} = \Phi\Theta\Psi\{a\} = \Gamma\{a\} \tag{80}$$

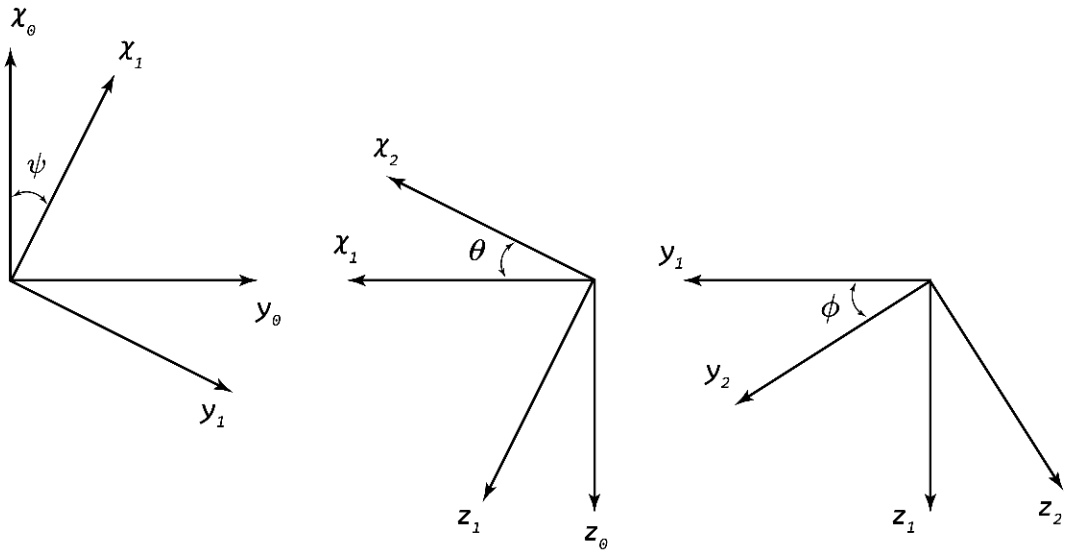

Figure 36: Pod Euler Angles

All the transformation matrices are orthogonal in themselves, and hence, it follows,

$$\Psi^T = \Psi^{-1}, \text{ etc.} \tag{81}$$

The product is also orthogonal, and hence,

$$\Gamma^T = \Gamma^{-1} \tag{82}$$

where,

$$\Gamma = \begin{bmatrix} cos\theta\ cos\psi & cos\theta\ sin\psi & -sin\theta \\ sin\phi\ sin\theta\ cos\psi - cos\phi\ sin\psi & sin\phi\ sin\theta\ sin\psi + cos\phi\ cos\psi & sin\phi\ cos\theta \\ cos\phi\ sin\theta\ cos\psi + sin\phi\ sin\psi & cos\phi\ sin\theta\ sin\psi - sin\phi\ cos\psi & cos\phi\ cos\theta \end{bmatrix} \tag{83}$$

The relationship between the time rate of change of the orientation angles and the angular velocities of the pod in the body axes system is given by,

$$\omega_g = pi_2 + qj_2 + rk_2 = \dot{\psi}k_0 + \dot{\theta}j_1 + \dot{\phi}i_2 \tag{84}$$

Using Eq. 77, Eq. 78 and Eq. 79 we can derive the following results.

$$\begin{aligned} p &= \dot{\phi} - \dot{\psi}sin\ \theta \\ q &= \dot{\theta}cos\ \phi + \dot{\psi}sin\ \phi cos\ \phi \\ r &= -\dot{\theta}sin\ \phi + \dot{\psi}cos\ \phi cos\ \theta \end{aligned} \tag{85}$$

14.2.3 Components of Gravitational Acceleration along the Rotorcraft Axes

The relations derived in Sec. 14.2.2 are especially important in flight dynamics as the gravitational components appear in the equations of motion in terms of the Euler angles, θ, ϕ and ψ. The corresponding aerodynamic forces are referenced directly to the pod's angular motion. We assume that in rotorcraft flight dynamics, the gravitational force always acts in the vertical sense, and the components of the body fixed axes are therefore easily obtained with reference to the transformation matrix given in Eq. 83. The gravitational acceleration components along the pod's x, y and z axes can be then written in terms of the Euler roll and pitch angles as,

$$\begin{aligned} a_{x_g} &= -gsin\theta \\ a_{y_g} &= gcos\theta sin\phi \\ a_{z_g} &= gcos\theta cos\phi \end{aligned} \tag{86}$$

14.2.4 The Rotor System - Kinematics of the Blade Element

The components of velocity and acceleration of blade elements relative to the external environment and the inertial axes system are crucial for calculating the loads acting on the blades and their associated dynamics. The only acceleration experienced by a flapping blade when the hub is fixed is due to the centrifugal forces and the out-of-plane motion. However, when the hub is free to translate and rotate, the velocities and accelerations of the hub contribute to the overall acceleration of the blade element. We begin with an analysis of the transformations between vectors in the non-rotating hub reference system and vectors in the blade-axis system. Fig. 37 illustrates the hub reference axes with the x and y directions oriented parallel to the body fixed axes centred at the centre of mass.

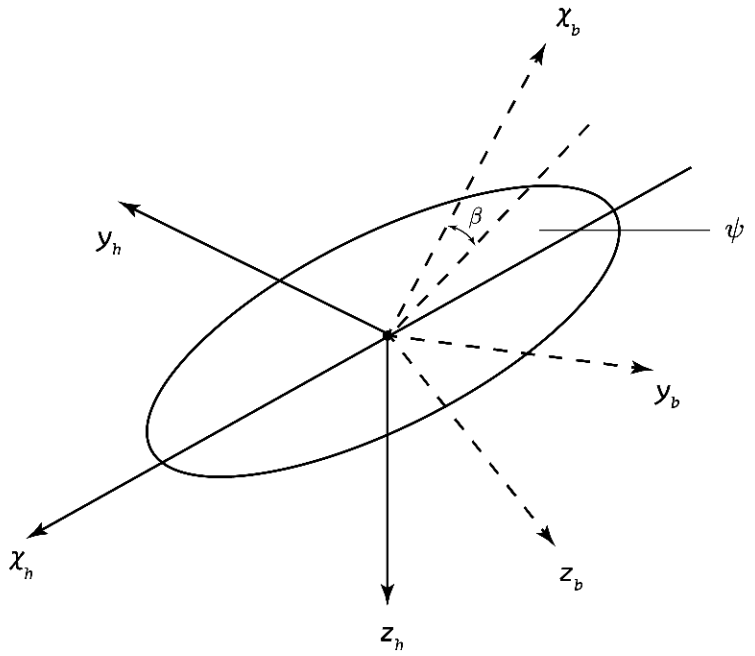

Figure 37: Hub and Blade Reference Frames

The z direction is directed downwards along the rotor shaft, which in turn is tilted relative to the pod's z axis by an angle γ_s. The blade-referenced axes system has the positive x direction along the blade quarter chord line. The zero azimuth position is conventionally at the rear of the disc, as shown in Fig. 37, with the positive rotation anticlockwise when viewed from above, i.e., platform view. In other words, a negative sense about the z axis. Positive flapping is upwards. The positive y and z directions are such that the blade and hub systems align when the flapping is zero and the azimuth angle is 180°.

The relationship between components in the rotating and non-rotating systems is derived by considering the unit vectors. The orientation sequence is first azimuth and then flap. Translational and angular velocities and accelerations in the hub system can be related to the blade system by the transformation,

$$\begin{bmatrix} i_h \\ j_h \\ k_h \end{bmatrix} = \begin{bmatrix} -cos\psi & -sin\psi & 0 \\ sin\psi & -cos\psi & 0 \\ 0 & 0 & 1 \end{bmatrix} \begin{bmatrix} cos\beta & 0 & sin\beta \\ 0 & 1 & 0 \\ -sin\beta & 0 & cos\beta \end{bmatrix} \begin{bmatrix} i_b \\ j_b \\ k_b \end{bmatrix} \tag{87}$$

expanding this further, we obtain,

$$\begin{bmatrix} i_h \\ j_h \\ k_h \end{bmatrix} = \begin{bmatrix} -cos\psi\ cos\beta & -sin\psi & -cos\psi\ sin\beta \\ sin\psi\ cos\beta & -cos\psi & sin\psi\ sin\beta \\ -sin\beta & 0 & cos\beta \end{bmatrix} \begin{bmatrix} i_b \\ j_b \\ k_b \end{bmatrix} \tag{88}$$

The hub and velocity components in the hub reference system are related to the velocities of the centre of mass, u, v and w through the transformation,

$$\begin{bmatrix} u_h \\ v_h \\ w_h \end{bmatrix} = \begin{bmatrix} -cos\ \gamma_s & 0 & sin\ \gamma_s \\ 0 & 1 & 0 \\ -sin\ \gamma_s & 0 & cos\ \gamma_s \end{bmatrix} \begin{bmatrix} u - qh_R \\ v + ph_R + rx_{cg} \\ w - qx_{cg} \end{bmatrix} \tag{89}$$

where γ_s is the forward tilt of the rotor shaft, h_R and x_{cg} are the distances of the rotor hub relative to the rotorcraft's centre of mass, along the negative z and forward x directions respectively.

During the derivation of rotor kinematics and loads, it is more convenient to refer to a non-rotating hub axes system that is aligned with the resultant velocity in the plane of the rotor disc. This is referred to as the hub-wind system, with the subscript hw. The translational velocity of the hub can then be written with two components as,

$$v_{hw} = u_{hw} i_{hw} + w_{hw} k_{hw} \tag{90}$$

Subsequently, the angular velocity of the hub takes the form,

$$\omega_{hw} = p_{hw} i_{hw} + q_{hw} j_{hw} + r_{hw} k_{hw} \tag{91}$$

The hub-wind velocities are given by the relations,

$$\begin{aligned} u_{hw} &= u_h cos\ \psi_w + v_h sin\ \psi_w = \sqrt{u_h^2 + v_h^2} \\ v_{hw} &= 0 \\ w_{hw} &= w_h \end{aligned} \tag{92}$$

$$\begin{bmatrix} p_{hw} \\ q_{hw} \end{bmatrix} \begin{bmatrix} cos\ \psi_w & sin\ \psi_w \\ -sin\ \psi_w & cos\ \psi_w \end{bmatrix} \begin{bmatrix} p \\ q \end{bmatrix} \tag{93}$$

$$r_{hw} = r + \dot{\psi}_w \tag{94}$$

where the rotor sideslip angle ψ_w is defined by the expressions,

$$cos\ \psi_w = \frac{u_h}{\sqrt{u_h^2 + v_h^2}},\ sin\ \psi_w = \frac{v_h}{\sqrt{u_h^2 + v_h^2}} \tag{95}$$

We can now write the angular velocity components transformed to the rotating system as,

$$\begin{bmatrix} \omega_x \\ \omega_y \end{bmatrix} \begin{bmatrix} cos\ \psi & -sin\ \psi \\ sin\ \psi & cos\ \psi \end{bmatrix} \begin{bmatrix} p_{hw} \\ q_{hw} \end{bmatrix} \tag{96}$$

Using the transformation matrix obtained in Eq. 88 and assuming that the flapping angle β remains small such that $cos\ \beta \approx 1$ and $sin\ \beta \approx \beta$, we note that the velocities of the blade at the blade station r_b, in the blade axes system can be written as,

$$u_b = -u_{hw}\ cos\ \psi - w_{hw}\beta$$

$$
\begin{aligned}
v_b &= -u_{hw}\ sin\ \psi - r_b(\Omega - r_{hw} + \beta\omega_x) \\
w_b &= -u_{hw}\beta\ cos\ \psi + w_{hw} + r_b(\omega_y - \dot{\beta})
\end{aligned}
\tag{97}
$$

In a similar fashion, the blade accelerations can be derived, but in this case, the number of terms increases drastically. The dominant effects are due to the acceleration of the blade element relative to the hub, with the centrifugal and Coriolis inertial forces. Blade normal accelerations are an order of magnitude smaller than this but are still an order of magnitude greater than the mean accelerations of the rotorcraft centre of mass and the rotor hub.

The translational acceleration of the hub and many of the smaller nonlinear terms shall be neglected due to the products of hub and blade velocities. The approximate acceleration components at the blade station are given by,

$$
\begin{aligned}
a_{x_b} &= r_b\left(\underline{-(\Omega - r_{hw})^2} + 2\dot{\beta}\omega_y - 2(\Omega - r_{hw})\beta\omega_x\right) \\
a_{y_b} &= r_b\left(-(\dot{\Omega} - \dot{r}_{hw}) - \beta(\dot{q}_{hw}\ sin\ \psi - \dot{p}_{hw}\ cos\ \psi) + r_{hw}\beta\omega_y\right) \\
a_{z_b} &= r_b\left(\underline{2\Omega\omega_x} + \underline{\left(\dot{q}_{hw}\ cos\ \psi + \dot{p}_{hw}\ sin\ \psi\right)} - r_{hw}\omega_x - \underline{(\Omega - r_{hw})^2\beta} - \underline{\ddot{\beta}}\right)
\end{aligned}
\tag{98}
$$

The underlined terms in the equations are the primary effects due to the centrifugal and Coriolis forces and angular accelerations of the hub, although the latter are also quite small in most cases. For practical considerations, we can make the additional assumption that the speed of the rotor is much higher than the pod's yaw rate and hence,

$$
(\Omega - r_{hw}) \ \approx\ \Omega \tag{99}
$$

14.2.5 Rotor Reference Frames: Hub, Tip, Path and No Feathering

Three natural reference axes systems have been found to be applicable in rotor dynamics analyses. These are the hub (or shaft) system, the tip-path plane (or no flapping) system and the no-feathering system. These are illustrated in Fig. 38, where the hub plane has been assumed to be horizontal for convenience.

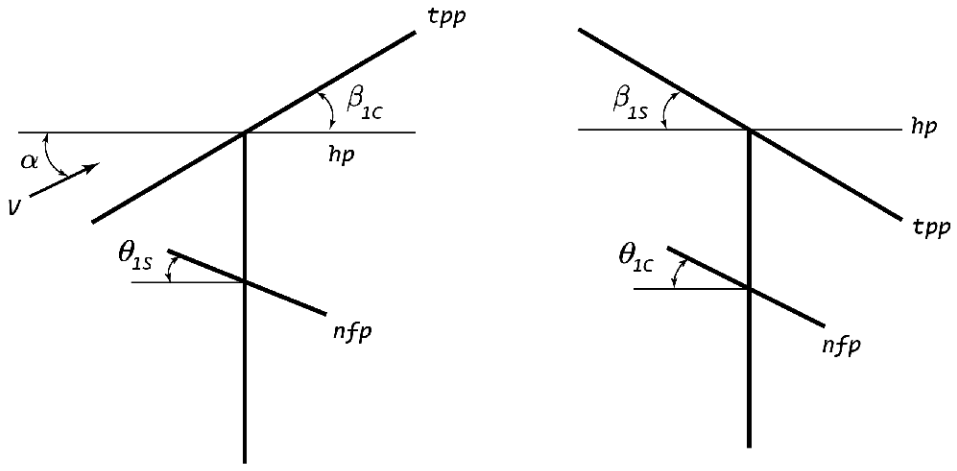

Figure 38: Longitudinal and Lateral Planes of Reference

Understanding the physical significance of these planes is of utmost importance. The motivation for adopting the rotor-oriented no-flapping or no-feathering plane is that it greatly simplifies the expressions

for the rotor X and Y forces. The no-feathering axes are the equivalent of the so-called control axes when the rotor pitch/flap coupling is zero. The control axes are aligned along the swashplate. Assuming small angles, the normalized velocities in the rotor systems are related to those in the hub system by the following approximate relations.

$$\begin{aligned} \mu_{tp} &= \mu_h + \mu_{zh}\beta_{1c} \\ \mu_{ztp} &= \mu_{zh} - \mu_h\beta_{1c} \end{aligned} \tag{100}$$

and,

$$\begin{aligned} \mu_{nf} &= \mu_h - \mu_{zh}\theta_{1s} \\ \mu_{znf} &= \mu_{zh} + \mu_h\theta_{1s} \end{aligned} \tag{101}$$

Similarly, the disc incidences are given by,

$$\begin{aligned} \alpha_{tp} &= \alpha_h - \beta_{1c} \\ \alpha_{nf} &= \alpha_h + \theta_{1s} \end{aligned} \tag{102}$$

and the non-rotating forces are given by,

$$\begin{aligned} X_{nf} &= X_h - T\theta_{1s} \\ X_{tp} &= X_h + T\beta_{1c} \end{aligned} \tag{103}$$

$$\begin{aligned} Y_{nf} &= Y_h - T\beta_{1s} \\ Y_{tp} &= Y_h + T\theta_{1c} \end{aligned} \tag{104}$$

It is assumed that the rotor thrust T and the Z forces in the three systems have the same magnitude and opposite directions.

In hover, the alignment of the tip-path plane and the no-feathering plane highlights the equivalence of flapping and feathering. It is to be noted that these expressions are only valid for rotors with flap articulation at the centre of rotation. These rotor axes systems cannot describe the elastic motion of hingeless rotors and the flapping of articulated rotors with offset flap hinges. The induced inflow, λ, is strictly referred to in the tip-path plane, giving the inflow normal to the hub plane as,

$$\lambda_h = \lambda_{tp} - \mu\beta_{1c} \tag{105}$$

The small flap angle, while negligible for trim flight, could be significant during manoeuvres when the flapping angles are large.

14.3 Mathematical Modelling Techniques

The rotorcraft flight dynamics mathematical models have been developed from the simple six-degree-of-freedom (DoF) rigid body model to complex multi-DoF models. These have been applied all the way from steady flight to large amplitude manoeuvring flight analyses. The models elaborated upon

in this section have been obtained from Ref. [53].

14.3.1 Linear Modelling

The six DoF model is given by a set of six second-order differential equations derived based on Newton's laws of motion. These are given by the following force equations,

$$\dot{u} = -(wq - vr) + \frac{X}{m_h} - gsin\ \theta \tag{106}$$

$$\dot{v} = -(ur - wp) + \frac{Y}{m_h} + gcos\ \theta\ sin\ \phi \tag{107}$$

$$\dot{w} = -(vp - uq) + \frac{Z}{m_h} + gcos\ \theta\ cos\ \phi \tag{108}$$

Moment equations:

$$I_{xx}\dot{p} = (I_{yy} - I_{zz})rq + I_{xz}(\dot{r} + pq) + L \tag{109}$$

$$I_{yy}\dot{q} = (I_{zz} - I_{xx})rp + I_{xz}(r^2 - p^2) + M \tag{110}$$

$$I_{zz}\dot{r} = (I_{xx} - I_{yy})pq + I_{xz}(\dot{p} - rq) + N \tag{111}$$

The linear six DoF model assumes the rotorcraft to be a rigid body, which is a convenient way to get the essential control and stability characteristics of the rotorcraft. It can be used during the preliminary stages of the design process. One limitation of this model is that it fails to take into account the non-linear effects of the dynamics of the system.

14.3.2 Non-Linear Modelling

There are primarily two kinds of non-linear rotorcraft flight dynamics models. The first one describes the non-linearity using the differential equation of rotorcraft motion. The linearity and non-linearity of the subsystems are implicitly expressed in this model. This model provides a relatively accurate and reliable foundation for rotorcraft control system design. An example of this model is the ARMCOP model [54]. This low-order model adopts a static-inflow model and uses the blade element theory to calculate the forces and moments of the rotor system.

The second type of modelling technique takes into account the non-linearity in the rotorcraft's motion while simultaneously considering the non-linearity in each subsystem.The modelling method is widely used for simulating rotorcraft flight. The GENHEL simulation package [55] developed by the Sikorsky helicopter company is one example that uses this modelling technique. While it assumes that the rotorcraft is a rigid body, it incorporates additional DoFs in addition to the six DoF system. These additional DoFs include the DoFs of rotor motion, including flapping, lagging and torsion, as well as the DoFs of the rotor's rotational motion.

This model uses empirical relations to fit the torsion motion of the blade. Its rotor aerodynamic model

combines the static non-uniform inflow model and the blade element theory to calculate model blade aerodynamics. The rotor downwash on other parts of the rotorcraft and other aerodynamic interference effects are also included based on the results of the experimental and theoretical analysis. The accuracy of this modelling technique is well understood, and this method has been widely used. According to flight test data, the GENHEL model has a relatively high precision in mid-speed forward flight range, but its accuracy in hover and high-speed ranges requires further improvement.

Helium 2, an improved flight dynamics simulation code developed by the University of Maryland, was developed to overcome the limitations of the GENHEL code [56]. It includes flexible rotors and free-vortex wake models to improve its accuracy across the flight envelope. It has also been expanded to include flexible wings and multi-rotor calculation capabilities. This model allows for flight dynamics investigation of various rotorcraft configurations, from single-rotor helicopters to compound helicopters and tilt-rotor aircraft.

The HeliUM 2 software has improved accuracy in the longitudinal control comparison, indicating increased precision in the aerodynamic interference calculation between the rotor wake and other parts of the rotorcraft. However, the accuracy of the collective pitch is lower than the GENHEL model. This is due to the fact that the aerodynamic interference inside the coaxial rotor system is significant. Hence, the rotor wake calculation method used in HeliUM 2 (free wake model) may introduce additional errors.

Tuning the flight dynamics model using empirical factors to improve the accuracy in steady and small amplitude manoeuvring flight is a viable option. However, the aerodynamic characteristics are significant in large amplitude manoeuvres, especially for advanced rotorcraft due to their multi-rotor system. Establishing an accurate model using empirical factors in such scenarios can be a challenging task.

Energy methods have been the primary approach to studying rotorcraft manoeuvring. This method is based on the theory of energy conservation, leading to the calculation of the trajectory of manoeuvring flight. While considering real conditions and specific circumstances, the accuracy of the energy method has been found to be relatively low. In the late 1980s, the inverse simulation method was developed to analyse the manoeuvrability of the rotorcraft.

The inverse simulation method uses mathematical description to input the flight trajectory and then obtains the control input during the manoeuvre by inversely calculating the flight dynamics equations. Although this method is successful in the context of manoeuvring flight and can yield meaningful results, the inverse simulation method still needs improvement in practical application due to the increasing complexity of the rotorcraft flight dynamics model.

Non-linear optimization methods and other manoeuvrability analysis methods have their inefficiencies from a practical standpoint. Hence, methods to investigate manoeuvring flight characteristics are still a key issue in the research of rotorcraft flight dynamics.

14.4 Rotorcraft Flight Dynamics Modelling

Rotorcraft flight dynamics modelling consists of rotor aerodynamic modelling, rotorcraft aerodynamic interference modelling, and the manoeuvring flight analysis method. This subsection elucidates the methods to carry out the aforementioned analyses.

14.4.1 Rotor Aerodynamic Modelling

The rotor provides the lift, the control power, and the propulsion that the rotorcraft needs. These are dependent on its aerodynamic characteristics. While modelling rotorcraft flight dynamics, three critical aspects of rotor aerodynamic modelling become extremely crucial. These are the airfoil aerodynamic model, the rotor wake model, and the blade dynamics model. These three aspects are interdependent and coupled with each other, increasing the complexity of modelling these systems.

14.4.1.1 Airfoil Aerodynamic Model

The airfoil aerodynamic model is the basis of the rotor aerodynamics model, determining the lift and drag of each blade element (airfoil) during different flight conditions. An extremely simplified airfoil aerodynamic modelling method is the 2D lift-curve slope theory, which calculates the lift coefficients at the corresponding angle of attack in conjunction with an empirical equation to calculate the drag coefficient. This method has been widely utilised to estimate initial flight dynamics and calculate performance. However, it fails to consider unique features of the helicopter airfoil aerodynamics, such as reverse flow and dynamic stall.

The airfoil aerodynamic characteristics of a rotor are quite in contrast to fixed-wing aircraft due to phenomena of dynamic stall, compressibility effects, reverse flow, and the radial flow effect. These features are illustrated in Fig. 39. The determination of the appropriate modelling method to simulate these features is of utmost importance in maintaining the accuracy of the airfoil aerodynamic model.

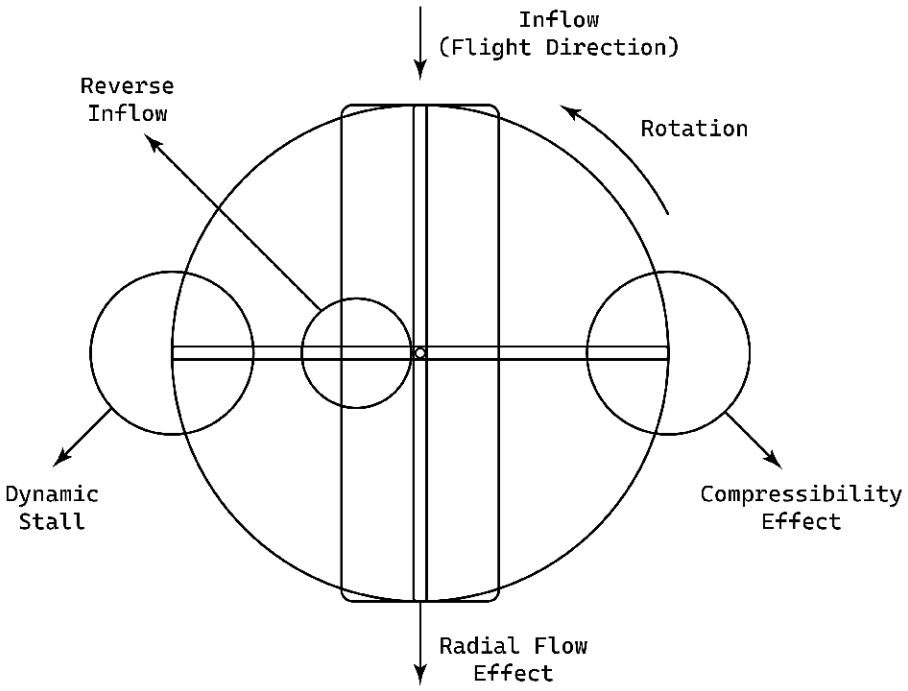

Figure 39: Features of Rotor Aerodynamics

Dynamic stall occurs due to the leading-edge vortex, which provides additional suction over the upper airfoil surface as it converts downstream. This increased suction leads to performance gains in lift and stall delay, but it quickly becomes unstable and detaches from the airfoil, leading to a rapid decrease in lift.

This phenomenon usually occurs at the blade tip of the retreating side of the rotor and is more significant in advanced rotorcraft as the increase of the forward speed exaggerates the flapping motion. Calculating the dynamic stall effect on a blade section, even with a detailed CFD method, is challenging, and therefore, a series of empirical or semi-empirical methods were developed based on experimental results, including an unsteady/dynamic stall aerodynamic model constructed by Leishman and Beddoes [57–59].

The calculation process is composed of three parts, the bound flow aerodynamics calculation, the trailing separation estimation, and the dynamic stall (advancing separation) aerodynamics calculation. An exponential response method is adopted to calculate the airfoil aerodynamics in the bound flow aerodynamics calculation.

The pressure on the leading edge is used to estimate the occurrence of airflow separation based on the correlation between the vertical force coefficient and the critical vertical force coefficient of the airflow separation. The critical coefficient is a function of the Mach number, which can be empirically determined according to steady airfoil aerodynamic test data.

Further, The French Aerospace Lab (ONERA) developed a 2-D dynamic stall model based on the Hopf bifurcation [60–62]. The lift and moment coefficients are calculated based on non-linear ordinary differential equations, and the relevant parameters in those equations are also based on wind tunnel experiments.

The compressibility effect and reverse flow have a substantial impact on airfoil aerodynamics. As forward speed increases, the local Mach number near the blade tip on the advancing side approaches the speed of sound, leading to a significant decrease in aerodynamic efficiency and a sharp rise in drag. Additionally, the reverse flow region expands with increasing forward speed, resulting in angles of attack in this area that are much higher than the stalling angle, making any simplistic calculation of lift and drag characteristics for the blade section inaccurate. The maximum forward speed of an advanced rotorcraft is significantly higher than that of a conventional rotorcraft, meaning that the compressibility effect and reverse flow greatly influence its flight dynamics.

Radial flow significantly impacts the aerodynamic characteristics of an airfoil, particularly during high-speed flight. Experimental results indicate that radial flow can generate an additional normal force on the inboard sections of the blade due to centrifugal and Coriolis forces, which in turn modifies the airfoil's aerodynamics and affects flight dynamics. As a result, radial flow can potentially delay the onset of stall on the rotor disc to some degree.

14.4.1.2 Rotor Wake Model

The rotor wake model calculates the induced velocity, which influences both rotor aerodynamics and flight dynamics characteristics. The aerodynamic interaction between rotor discs plays a crucial role in affecting

the induced velocity on each disc, thereby altering the overall flight dynamics. Consequently, to accurately simulate the flight dynamics of a rotorcraft, the interactions within a multi-rotor system should also be accounted for in the rotor wake model.

Two key requirements for a rotor wake model are accuracy and computational efficiency. The accuracy of the rotor wake model directly impacts the validity of the flight dynamics model. At the same time, its computational efficiency determines how effectively the flight dynamics model can be used for practical analysis. A high time cost restricts the model's ability to assess control responses and handling characteristics.

Different types of wake models have been developed, such as the most straightforward rotor disc uniform-induced velocity model, the finite-state inflow, the fixed wake method, the free wake model, and higher-resolution wake models developed recently.

The uniform-induced velocity model is a simplified rotor wake model known for its computational efficiency, which is based on the correlation between induced velocity and aerodynamic loading on the rotor disc. This model can be considered to be a wake model derived from momentum theory. However, its feasibility is limited. During forward flight, the helicopter's wake tilts backwards, leading to a non-uniform distribution of induced velocity, which reduces the accuracy of the uniform-induced velocity model.

Carpenter and Friedovich [63] extended the momentum theory into the dynamic inflow model, incorporating the additional inertia effects caused by disturbances on the rotor disc. This dynamic inflow model can simulate the dynamic variations in induced velocity, which is expressed using first-order ordinary differential equations.

Pitt, Peters, and He developed the Pitt-Peters dynamic inflow model [64] and its generalized version, the Pitt-He finite-state (high order) inflow model, based on the acceleration potential theory. This wake model has been widely applied in flight dynamics analysis and control response calculations. However, these models require that the inflow velocity be significantly greater than the induced velocity on the rotor disc. Consequently, the dynamic inflow model is applicable only for rotors with low loading or during mid to high-speed forward flight. Additionally, Ferguson [65] used a modified dynamic inflow model to study the flight dynamics of a coaxial compound helicopter. Despite this, empirical corrections are necessary to adjust the parameters in the dynamic inflow model, limiting its broader application.

Peters further refined the finite state inflow method using the Galerkin approach to potential flow equations, enabling it to compute induced flow throughout the entire flow field. This suggests its potential use in determining aerodynamic interactions within multi-rotor systems. Comparisons with flight test data indicate that the method provides acceptable accuracy for flight dynamics analysis, making it a promising candidate for incorporation into flight dynamics models for advanced rotorcraft, such as coaxial compound helicopters and tilt-rotor aircraft. However, this method has only been validated in the hover state for coaxial helicopter configurations, and issues with numerical convergence present a significant challenge to its further development.

Based on rotor vortex theory, the free-wake model calculates the helicopter's rotor wake by directly solving for wake geometry without the need for experimental data. This method typically divides the wake system into two main parts: the near wake, consisting of trailed and shed vorticity behind each blade, and the far wake, comprising rolled-up tip vortices. The free-wake problem is solved by integrating a system of ordinary differential equations derived from the spatial discretization of partial differential equations governing the tip vortex positions. By applying the Biot-Savart law, local velocities at specific points on the vortex filaments are calculated, allowing the vortex elements to move with the local airflow and simulate wake self-induction and distortion. The induced velocity vector throughout the flow field can be determined using this method, making it suitable for advanced rotorcraft modelling, including multi-rotor aerodynamic interactions and wake distortion effects during flight. While the explicit Euler time-marching method was initially used, its numerical stability issues led to the development of two alternative methods: the classical relaxation free-wake method, which introduces a periodic condition constraint, and the time-accuracy free-wake method, which combines forecast-correction with a high-order time-marching approach to reduce numerical oscillations.

The line vortex discrete embedded free wake model is a well-established method for helicopter flight dynamics modelling. It offers both high precision and reduced computational time, with a significant advantage in efficiently calculating aerodynamic interference between rotors—an essential factor in advanced rotorcraft modelling. However, this model is based on potential flow theory, which does not account for viscous effects. To enhance accuracy, researchers have incorporated empirical coefficients into the vortex core model and used the position of tip vortex distortion to account for viscosity. Despite these improvements, the reliance on empirical coefficients limits the model's effectiveness in analyzing manoeuvrability and control response.

Yuan, Chen, and Li developed the multi-transmutable-vortex-ring (MTVR) wake model based on the rotor disc assumption and fixed wake theory. This model can calculate the induced velocity throughout the flow field with improved computing efficiency, meeting real-time requirements. Validation results accurately simulate the induced velocity distribution for coaxial compound helicopters at various forward speeds. However, the extensive wake variables involved in this method can create challenges with convergence during calculations.

The fast multipole method (FMM) has recently been combined with high-resolution vortex methods to improve rotor wake modelling. The vortex transport method (VTM) and the viscous vortex particle method (VVPM) have been developed for accurate rotor wake calculations, incorporating both non-viscous and viscous effects. While these methods offer improvements, they often use simplified models like lift-line or lift-surface, which can reduce accuracy in capturing airflow around the blade. Rotor CFD methods provide detailed simulations of airflow separation, dynamic stalling, and shock waves, but they face numerical dissipation issues that can lead to excessive vorticity attenuation. To address this, some researchers have integrated CFD with wake methods to achieve precise wake calculations, capturing flow details and wake viscous dissipation. However, this combined approach is computationally intensive, impacting the efficiency

of flight dynamics modelling.

14.4.1.3 Blade Dynamics Model

Blade motion in helicopters comprises three components: flapping, lagging, and torsion (pitching). Flapping motion is crucial for helicopter flight dynamics as it governs the rotor system's control power and propulsion. Advanced rotorcraft often have different blade motions compared to conventional helicopters to enhance performance. For example, coaxial compound helicopters like the X2TD and SB-1 use rigid rotors to delay dynamic stall at high speeds, while tilt-rotor aircraft use gimbal rotors to address aeroelastic instability in high-speed aeroplane mode. These adaptations significantly alter blade motion characteristics and, in turn, impact the flight dynamics of advanced helicopters.

In steady flight, the aerodynamic characteristics of the blades are consistent because their motion trajectories are identical, and the tip planes of the rotor blades maintain the same shape. Thus, the flapping motion of the blades can be fully described using the coning angle, longitudinal flapping angle, and lateral flapping angle, which is known as the rotor plane method. This method effectively determines the orientation of aerodynamic forces and their impact on the vehicle's motion. However, during large amplitude manoeuvres, the aerodynamic and inertia forces on each blade vary, and turbulent conditions can cause the trajectories of rotor blades to diverge from a single plane. This results in reduced accuracy of the rotor plane method. To address this, two alternative approaches have been developed to improve the accuracy of blade motion calculations during manoeuvring flight. The first method is to assume that the rotor blades still have the same dynamic trajectory. The second method abandons the hypothesis that each blade should be kept in the same plane and separately investigates the flapping motion of each blade in rotational coordinates. Compared to the first method, this approach can sufficiently capture the Coriolis force derived from the vehicle's angular motion and the inertia force from manoeuvring flight.

14.4.2 Modelling of Aerodynamic Interference

The downwash and side wash effects of the rotor impact the dynamic pressure, angle of attack, and sideslip angle of other parts of the helicopter. Analyzing rotor wake instability and time-varying characteristics analytically can be challenging, so wind tunnel data is commonly used to predict these effects. Determining which parts of the helicopter are affected by the rotor wake and quantifying the additional influence from this interference is a significant challenge in the modelling process. Additionally, during manoeuvring flight, the dynamic motion of the rotor wake increases the effects of aerodynamic interference. Both of these factors must be considered in the modelling process.

14.4.3 Integration and Calculation of Non-Linear Systems

Helicopters exhibit a variety of nonlinear effects that create distinct dynamic characteristics. Calculating and integrating these nonlinear systems poses a significant challenge in flight dynamics modelling. Additionally, the presence of extra components in advanced rotorcraft raises the demands on the integration and calculation processes.

Firstly, the motion of the helicopter's body exhibits low-frequency characteristics and strong coupling, resulting in nonlinear governing differential equations. Additionally, aerodynamic interference significantly impacts these nonlinear characteristics. The downwash or side wash from the rotor wake causes discontinuities in the aerodynamics of the fuselage, horizontal, and vertical tail, further complicating the calculation process.

Secondly, the flight dynamics model must include a rotor wake model to account for aerodynamic interference. However, current rotor wake models face challenges with numerical instability and calculation inefficiency. When integrated with the flight dynamics model, these issues become more pronounced. A loose coupling method is required to reduce numerical instability and improve calculation efficiency.

Thirdly, the unsteady and dynamic stall characteristics of the airfoil affect the air loading on the rotor blade. These unsteady aerodynamic characteristics are primarily influenced by the effect of shed vortices in the wake. When using both the rotor wake model and the airfoil unsteady aerodynamics model to model helicopter flight dynamics, it is important to avoid double-counting the unsteady effects from the shed vortices.

Fourth, the governing equations of the helicopter flight dynamics model must be formatted specifically due to the coupling effects between blade dynamics and the interaction between the rotor and fuselage, which complicates the use of traditional solving methods. Tornour and Celi [66] employed analytical solutions to separate the inertia coupling related to vehicle acceleration from the rotor/fuselage coupling dynamic functions, reformulating it into a first-order ordinary differential equation. This approach has become widely used for flight dynamics analysis and simulation.

As the complexity of rotor aerodynamics and aerodynamic interference models grows, more effort will be needed to develop effective integration and calculation methods. The key challenge for high-confidence helicopter flight dynamics modelling is balancing modelling accuracy with computing time to ensure that accuracy and efficiency are maintained across all flight conditions.

14.4.4 Manoeuvrability Analysis

As flight dynamics modelling accuracy improves, several new methods for manoeuvrability analysis have emerged, including the nonlinear optimal control (NOC) method and the inverse simulation method.

The NOC method, which relies on collocation and numerical optimization, has been used for manoeuvrability analysis in conventional helicopters and tilt-rotor aircraft. It incorporates a human-operator model to account for pilot biometric lag and improve simulation accuracy. However, this method can experience internal numerical instability and convergence issues, particularly when using discrete modelling techniques like the rotor-free wake model. As a result, the NOC approach is best suited for task profile investigations (such as flight range and duration calculations) and small-to-moderate amplitude manoeuvrability analysis.

The inverse simulation method is still under development. It relies on a pre-determined trajectory,

meaning that a mathematical description of the manoeuvring task must be provided in advance. However, some manoeuvres, including certain mission-task elements (MTEs) from rotorcraft handling qualities requirements, do not have fixed trajectories and are difficult to describe mathematically. Additionally, inverse simulation calculates control inputs by solving the helicopter flight dynamics equations, which can yield multiple solutions in some flight states. Additional constraints are needed to find an optimized solution, but these constraints may not always align with realistic piloting strategies. While inverse simulation can generate cockpit inputs that meet performance requirements, these inputs are just one of many possible control methods that could achieve the desired MTEs. Furthermore, advanced rotorcraft often have redundant control inputs, such as rudder and elevator, which can affect the results of inverse simulation.

Recent manoeuvre studies have focused on evaluating handling quality ratings using control input results from NOC or inverse simulation methods. Wavelet analysis has become popular due to its excellent time-frequency resolution. This method uses a finite-length bandpass filter to show signal energy across different frequencies and time histories. With wavelet analysis, the main frequency components of the control input can be identified. Research indicates that pilot workload and handling quality ratings depend on these primary frequency components. Consequently, a numerical correlation between the main frequency range and handling qualities ratings can be established, allowing for straightforward calculation of handling qualities ratings once control input data is available.

15 Electronics

To fulfil the power demands during hover and vertical flight phases, a solar-powered system consisting of a brushless direct current (BLDC) motor was chosen as the primary power source. The motor receives electrical power from a battery, which, in turn, is replenished by an onboard solar power system. This solar power system charges the battery, and the stored energy powers the motor, facilitating the rotation of co-axial propellers to generate essential thrust.

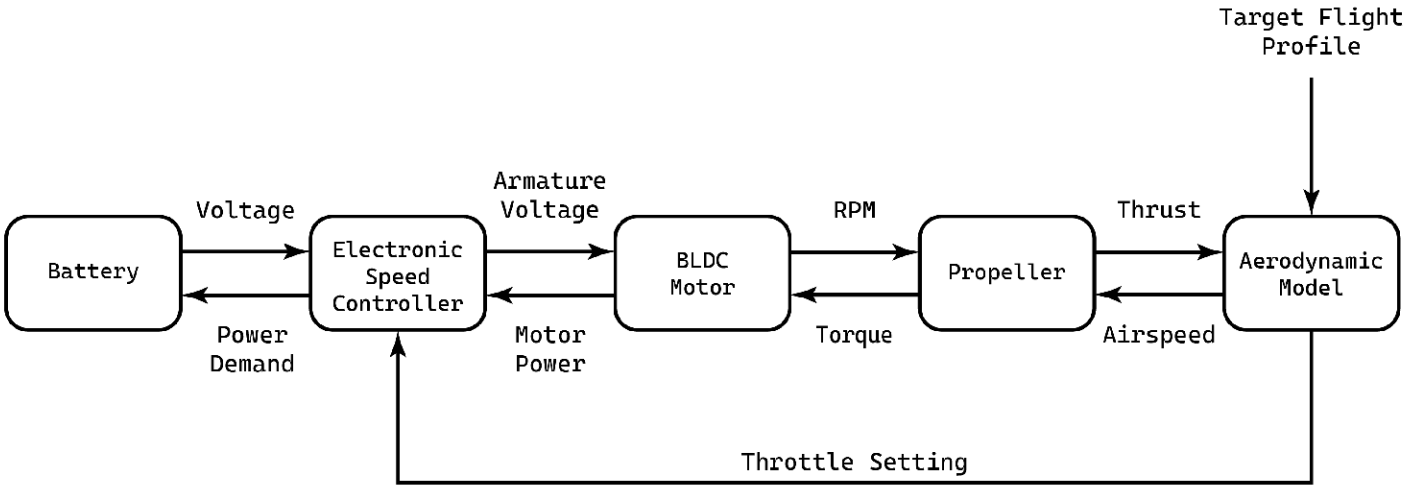

Figure 40: UAV Power Model Block Diagram

The subsequent sections delve into the integration of solar panels, batteries, and motors to power the UAV and aim to provide a comprehensive overview of the design considerations, technical specifications, and performance assessment of the proposed power generation setup (Fig. 40).

15.1 Solar Power System

Traditionally, UAVs rely on replaceable batteries as their primary energy source. However, for this particular mission, solar energy has been selected as the primary energy source on Mars to recharge the onboard battery. The fundamental principle revolves around harvesting energy from sunlight using a series of photovoltaic cells which convert solar energy into usable electrical energy through the photovoltaic effect.

The photovoltaic effect is a phenomenon by which certain semiconductor materials absorb the photons from sunlight, excite the electrons and create electron-hole pairs, thus creating a photocurrent inside the material. Therefore, the semiconductor layer is the most important layer in a solar cell. There are several technologies involved with the manufacturing process of photovoltaic cells, using material modification with different photoelectric conversion efficiencies in the cell components.

Due to the emergence of many non-conventional manufacturing methods for fabricating functioning solar cells, photovoltaic technologies can be divided into four major generations [67], as depicted in Fig. 41. The first generation of solar cells was based on Monocrystalline and Polycrystalline Silicon and Gallium Arsenide. Crystalline Silicon cells are the most widely used cells for residential purposes and are one of the most efficient and durable cells. However, they have poor high-temperature characteristics and, most importantly, have a high mass density, which is unsuitable for the current mission considering an all-up mass constraint of 70 kg.

Therefore, second-generation solar cells were chosen for the mission due to their significantly lower mass density and material requirement owing to their thin-film nature. Some commonly used semiconductor materials for thin films are Amorphous Silicon, CdTe (Cadmium Telluride), CIGS (Copper Indium Gallium Selenide) and Organic polymers. All of these materials have attributes like low weight and lower cost-to-power ratio. However, only CIGS cells have conversion efficiency suitable for the mission (15-20%) [68] whereas a-Si and CdTe cells have a much lower conversion efficiency ($\leq$10%) [68] and thus a thin-film solar cell with CIGS as its semiconductor was chosen.

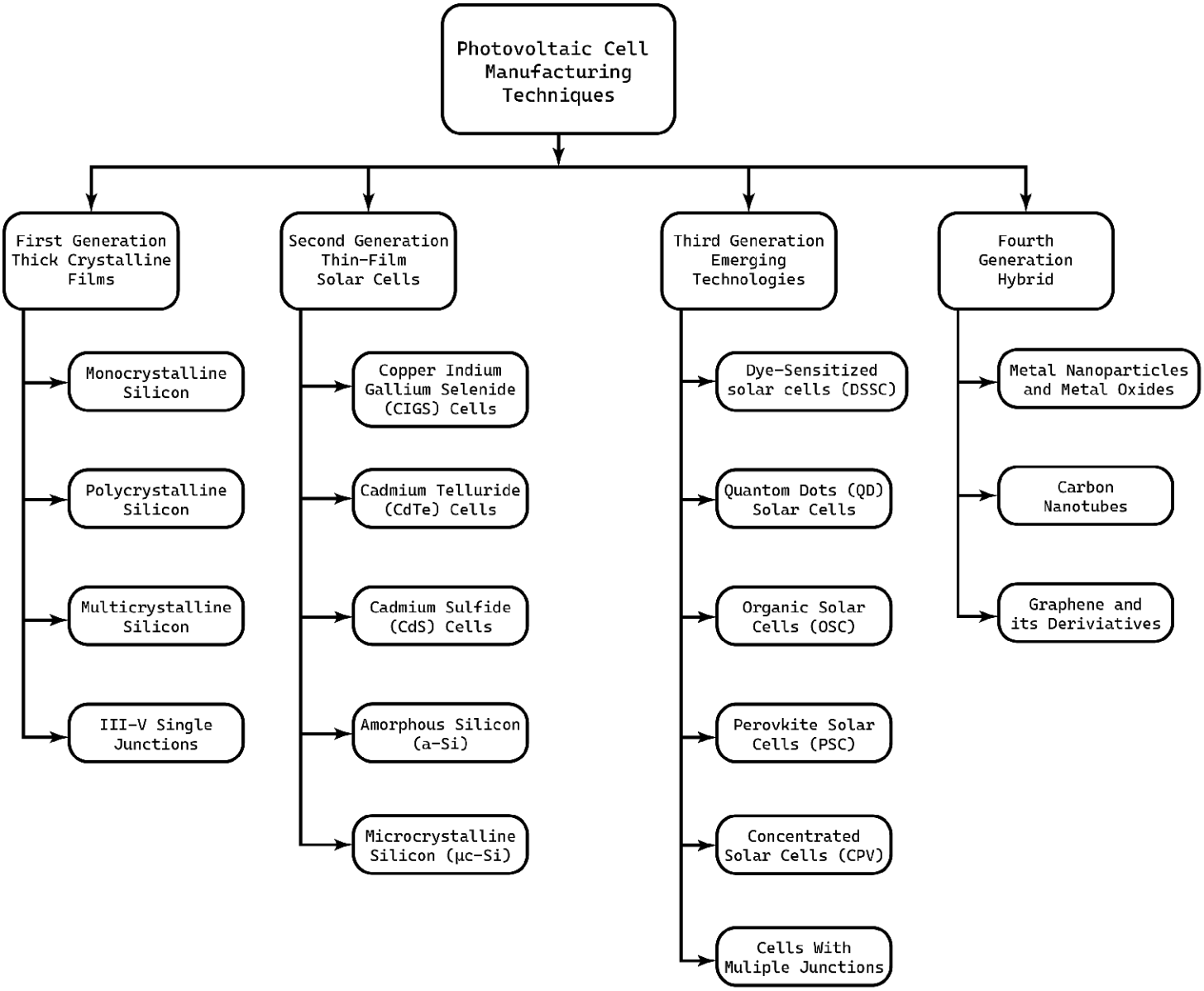

Figure 41: Classification of PV cells [4]

15.1.1 Solar Cell Structure

A typical cell structure of a thin film consists of the following layers:

- Substrate Layer
- Back Contact
- Semiconductor Absorber Layer
- Buffer Layer
- Front Contact/Transparent Conductive Oxide (TCO) Layer

This structure is given by the following diagram (image only for representational purposes):

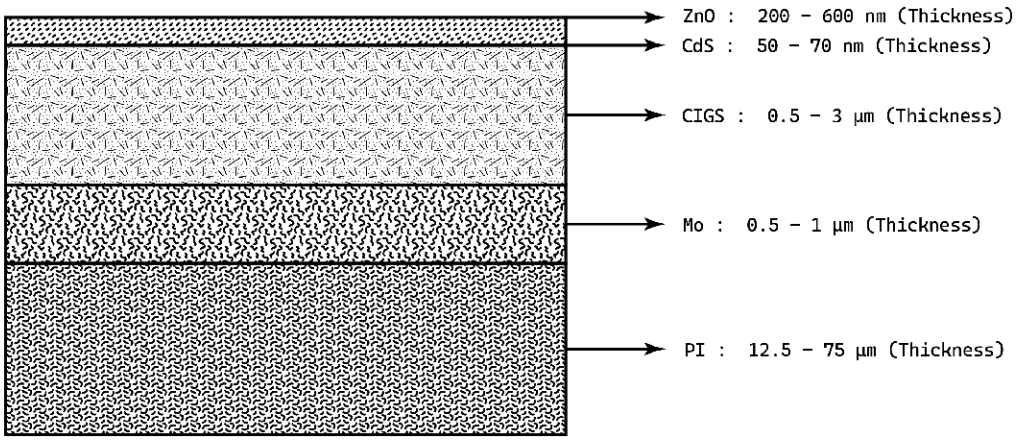

Figure 42: Schematic of the Solar Cell Structure

The substrate layer plays a crucial role in supporting the subsequent layers responsible for converting sunlight into electricity. The substrate serves as a foundation upon which thin films of semiconductor materials are deposited to create the photovoltaic device. One of the primary functions of the substrate layer is to provide mechanical stability, and it must be rigid enough to handle manufacturing processes like layer deposition and sputtering. Additionally, this layer serves other critical functions like thermal stability, nucleation performance and optical enhancement. Substrates used for CIGS cells are of two types, rigid and flexible. For rigid substrates, Soda-Lime Glass (SLG) is used, and for flexible substrates, Metal foils and Polymers like Polyamides are used [69]. The substrate material chosen for the mission is Polyamide polymer, which acts as a rigid support while still being extremely flexible and thin.

The back contact layer plays a pivotal role in facilitating electron collection and current flow, thereby contributing to the overall efficiency and performance of the solar cell. Situated beneath the active semiconductor layer, the back contact layer serves as the electrode through which the generated electrons are extracted and transferred to an external circuit for utilization. Furthermore, the back contact layer also acts as a reflective surface to redirect any photons that penetrate through the active semiconductor layers back into the cell for additional absorption. Molybdenum (Mo) is a preferred back contact material for CIGS solar cells because it does not react strongly with CIGS, forms low-resistivity Ohmic contact to CIGS, and the conductivity of Mo does not degrade during deposition of CIGS at high substrate temperature [70] and is thus chosen as the suitable material for the back contact layer of the solar cell to be used in the mission.

The semiconductor layer is a fundamental component of thin-film solar cells, serving as the active material responsible for converting sunlight into electricity by absorbing photons. This absorption capability allows the semiconductor to efficiently capture solar radiation and convert it into electron-hole pairs within the material. Moreover, this layer is responsible for separating the charge carriers, i.e., electrons and holes, and facilitating their transport to their respective electrodes for utilisation. The layer is made of copper indium gallium (CIG) before going through the selenization process. During the selenization process, Selenium (Se) vapour reacts with CIG to become CIGS and reacts with Mo to form the $MoSe_2$ layer. This interfacial layer between Mo and CIGS is beneficial for a wider bandgap.

The buffer layer is a critical component of thin-film solar cells positioned between the semiconductor absorber layer and the Transparent Conductive Oxide (TCO) layer, preventing unwanted chemical reactions or diffusion of materials that could degrade the solar cell's performance. Moreover, the buffer layer can also serve as a doping layer to adjust the electrical properties of the absorber layer, particularly in CIGS thin-film cells. For CIGS cells, a buffer layer made of Cadmium Sulfide (CdS) is considered suitable due to the difference in the energies of electron affinity E_A of n-type CdS and p-type CIGS.

The front contact layer facilitates the extraction of charge carriers from the semiconductor layer. This layer also functions as a transparent Conductive Oxide (TCO) layer that allows the penetration of sunlight into the absorber layer. Materials with high optical transparency and electrical conductivity, which enable effective light transmission and charge carrier extraction, like Indium Tin Oxide (ITO) and Zinc Oxide (ZnO), are preferred for this layer. Zno was chosen as the TCO layer material due to its compatibility with the CIGS layer with respect to its deposition using either sputtering or chemical vapour deposition (CVD) without causing any adverse reactions.

Layer	**Material**	**Thickness**
Substrate Layer	Polyamide	75 μm
Back Contact Layer	Molybdenum	2 μm
Semiconductor Absorber Layer	Copper Indium Gallium Selenide	3 μm
Buffer Layer	Cadmium Sulfide	70 nm
Front Contact Layer	Zinc Oxide	600 nm
Total Thickness		80.67 μm

Table 8: Description of the Solar Cell Layer

15.1.2 Solar Panel Mechanism

With its distinctive environmental characteristics, Mars presents formidable challenges for the operational efficacy of solar power systems. These challenges chiefly stem from its dusty atmosphere, which undergoes continual alterations in both the spectral composition and intensity of incident solar illumination throughout the diurnal cycle. Moreover, the degradation of array performance due to the accumulation of dust particles poses a significant impediment, further compounded by the imperative for low-temperature operation in the Martian environment. Solar panels have emerged as the primary energy source for powering UAVs for Martian exploration. Designing an efficient deployment mechanism for these solar arrays demands meticulous consideration of various factors. The solar panel deployment mechanism utilises a sophisticated yet robust approach to optimise space utilisation and facilitate efficient deployment and retraction of the solar panels.

Initially, a concept involving solar arrays folding in a zigzag pattern and attaching to the UAV's sides

was explored. However, practical constraints, particularly concerning the weight of telescopic arms and scissor mechanisms, rendered this approach impractical. In pursuit of a lightweight solution, the current deployment mechanism prioritises simplicity and efficiency. The deployment mechanism derives inspiration from the principles of NASA's InSight mission while incorporating novel adaptations tailored to UAV requirements. It involves a single base plate affixed to the UAV body, from which an arm extends outward, carrying the folded solar panel. The solar panel configuration takes the form of a circular shape, segmented into eight distinct sections to ensure structural stability and support. During the stowing process, these segments fold inward from the centre, allowing for compact storage and efficient utilization of space. An articulated arm, interconnected to a motorised assembly integrated into the UAV's framework, facilitates the extension and retraction of the solar panels through a pulley system. A graphic reference for the aforementioned mechanism is shown below.

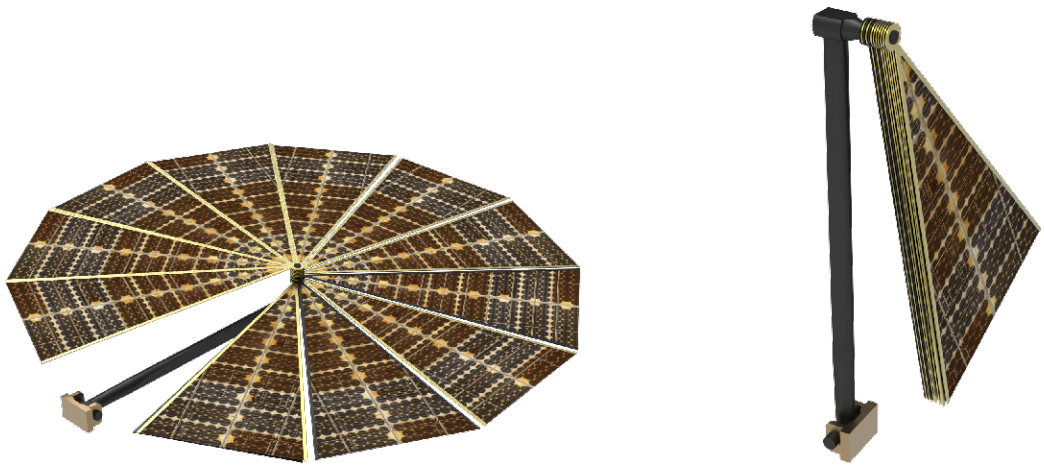

(a) Deployed (b) Folded

Figure 43: Solar Panel Mechanism

Recognising the detrimental impact of dust deposition on array performance, proactive measures are essential. Consequently, plans include applying an anti-dust coating to the solar panels. This coating, serving as a self-cleaning layer, aids in maintaining the surface cleanliness of solar cells [71][72]. Additionally, strategic spacing between folded panels allows dust clearance during retraction, preventing long-term efficiency degradation due to dust accumulation. The determination of the 25 m^2 solar panel area for the UAV involved a comprehensive assessment of critical factors essential for optimal performance in the Martian environment.

Primarily, consideration was given to the UAV's energy requirements, encompassing essential functions such as propulsion, charging batteries, and heating. This analysis facilitated a precise estimation of the necessary power generation capacity. With the determined panel and type of solar cells to be used, the solar power output can be calculated in the following way.

$$\text{Solar Power O/P } (W) = \text{Panel Area } (m^2) \times \text{Irradiance } (W/m^2) \times \text{Panel Efficiency} \tag{112}$$

The solar panel efficiency mentioned in the equation above is taken to be 17% as suggested in the problem

statement. Additionally, a thorough evaluation of solar irradiance patterns on Mars was conducted, accounting for diurnal variations. Using both empirical data and sophisticated modelling techniques, an accurate assessment of average daily insolation levels was attained, informing the sizing of the solar panel array to ensure consistent energy capture. Efforts were also directed towards selecting high-efficiency solar cell technologies and balancing performance with weight and spatial constraints. This deliberation aimed to maximise energy conversion efficiency while optimising resource allocation.

Moreover, measures were integrated into the design to mitigate the impact of dust accumulation on panel performance. This included the application of specialised coatings and incorporating self-cleaning mechanisms, ensuring sustained energy production over the mission's duration. The solar panel deployment mechanism was assessed to ensure structural integrity and operational reliability. In summary, the sizing of the solar panel area for the UAV involved a comprehensive analysis of energy requirements, solar irradiance variability, cell efficiency, and dust mitigation strategies. This diligent approach ensures the UAV's readiness for prolonged and effective missions on the Martian surface.

In summary, the proposed deployment mechanism for solar power systems in Mars exploration UAVs addresses the intricate challenges the Martian environment poses. Through a combination of innovative design and proactive maintenance strategies, the efficiency and longevity of solar panels can be maximized, ensuring reliable power generation for sustained flight on the Red Planet.

15.2 Battery

The energy collected and converted from the solar panels must now be stored so that it can be used to power the motor to generate the required thrust during the flying phase. Lithium-Polymer (LiPo) batteries are traditionally used to power UAV motors due to their high energy density, lightweight construction, high discharge rates and fast charging capability. They are thus chosen as the battery for the UAV to be used in the mission. It is based on the technology using a solid polymer as the electrolyte instead of a liquid electrolyte. The positive electrode material uses conductive polymers or inorganic compounds, the negative electrode often uses lithium metal or lithium-carbon intercalation compounds, and the electrolyte uses solid or colloidal polymer electrolytes or organic electrolytes.The specifications of the battery are shown in Tab. 9.

Some of the parameters, like Energy Density and Depth of Discharge, are constrained by the problem statement. In contrast, other parameters have been fabricated with suitable values for the mission while also keeping technical feasibility in mind.

- **Energy Density**: Refers to the amount of energy it can store per unit weight and is a critical parameter in determining the performance and suitability of a battery.
- **Depth of Discharge**: Refers to the fraction of total battery capacity that can be depleted and affects the battery's health and lifespan.
- **State of Charge**: It is the ratio of the current battery energy to the maximum energy of the battery and is crucial in understanding the energy availability at any given time.

Parameter	Value
Energy Density	650 kJ/kg (180 Wh/kg)
Number of Battery Packages	2
Battery Mass	2× 1.5 kg
Total Energy Capacity	2× 270 Wh
Max. Depth of Discharge	75%
Packing Configuration	24S
Working Voltage	100 V
Battery Ah Rating	2× 2.7 Ah
Charge C Rating	1
Discharge C Rating	20
Cycle Life	$\geq$ 300
Dimensions	108 mm x 108 mm x 190 mm

Table 9: Battery Parameters

One of the most crucial phases of the mission is the charging of the battery, as it takes up most of the mission time. Minimizing this charging time would amplify the level of success of the mission since having a lower charge time increases the number of sorties that can be carried out in the given mission time. The charging time of a battery can be obtained through the following relations.

$$\text{Battery Ah} = \frac{\text{Total Battery Energy}}{\text{Battery Voltage}} \tag{113}$$

$$\text{Charge Current, I } (A) = \frac{0.5 \times \text{Solar Power O/P}}{\text{Battery Voltage}} \tag{114}$$

$$\text{Charge Time (mins)} = \%\text{DOD} \times \frac{\text{Battery Ah}}{\text{Charge Current}} \times 60 \tag{115}$$

Firstly, the Ah rating of the battery is obtained from the total energy capacity and operating voltage of the battery using Eq. 113. The charging current of the battery is calculated using Eq. 114 from the solar power outputted from the solar panels and the voltage of the battery. It can be seen in the equation that half of the solar power is considered since there are two batteries to be charged. These batteries will be used to power two motors which will eventually power two respective rotors. This will be discussed in detail in the coming sections. After the battery has depleted the required energy for the mission, it needs to be replenished by the same amount of energy. In Eq. 115, %DOD is a good way of expressing the discharged energy that needs to be recharged, and it represents the percentage of Battery Ah value that has to be charged. The charge time is obtained in minutes using battery Ah and charge current.

15.3 Motor

Now that energy has been collected, converted, and stored, we must use it to generate thrust to lift the UAV. Traditionally, in UAVs, a BLDC (Brushless DC) motor is used to draw energy from the battery and supply it to the rotors due to their efficiency, reliability and precise control capabilities. BLDC motors are known for their high power-to-weight ratio, making them well-suited for UAVs where minimising weight is crucial for maximising flight endurance and payload capacity.

The power requirement of the rotors to generate the necessary thrust during the Hover phase, as mentioned to be 7828 W in Fig. 20a, must be met by the motor by matching the power output with the required power for hover. Similarly, for vertical phases of flight like Climb and Descend, the power requirements varying with the rate of climb are shown in Fig. 21. The motor is selected while keeping in mind its specifications and capability to fulfil the following power requirements of the rotors to be outputted from the motor,

- Hover Power = 7828 W
- Climb Power (for ROC = $2m/s$) = 8100 W
- Descend Power (for ROC = -$2m/s$) = 7571 W

As mentioned in Sec. 10.10, the power required to climb and descend depends on the rate of climb and descend with which the UAV performs these vertical phases. A feasible rate of climb and descent is chosen to be 2 m/s and is thus being considered for now. Moreover, it must be noted that an additional power of 50W must be added to the power requirements of all phases. This additional 50 W is required for the functioning of onboard payload sensors. The aforementioned power values are the power requirements of the rotors and need to be supplied to the rotors by the motor. As mentioned earlier, two batteries are used to facilitate the operation of two separate motors to power the two counter-rotating rotors. An equal split of power is assumed for both the rotors, thus the power calculations are halved for each motor. Moreover, the operating efficiency of the motors needs to be considered in order to understand the input power required by the motors themselves. The efficiency is taken to be around 85%, and all the values can be found in Tab. 11. The input power values for the motors are thus obtained as follows,

- Hover Power = $0.5 \times 7828 \times 1/0.85 = 4604.7$ W
- Climb Power = $0.5 \times 8100 \times 1/0.85 = 4764.7$ W
- Descend Power = $0.5 \times 7571 \times 1/0.85 = 4453.53$ W

The motor specifications were finalised based on the power and other requirements of the mission while keeping feasibility and realism in mind. The motor specifications are mentioned below. It can be observed that the previously stated power input to the motor required for the hover and vertical phases of flight lies in the throttle range of 50-55%.

(a) Motor

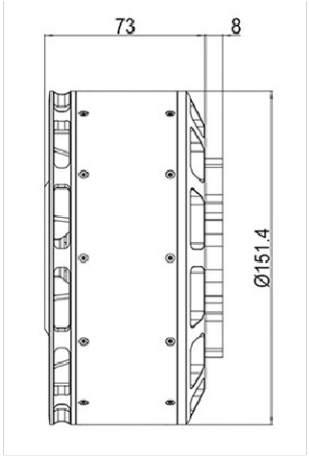

(b) Motor Dimensions

Figure 44: Motor Specifications

Parameter	**Value**
KV Rating	43
Mass	2× 2.5 kg
Configuration	36N30P
Max. Current	238 A
Nominal Voltage	24S
Internal Resistance	20.3 mΩ
Max. Power	23 kW
Max. Torque	47.7 $N-m$
Max. Operating Temperature	125 °C

Table 10: Motor Specifications

From the motor data presented in Tab. 11, the following graphs showcasing the trend of various operational motor parameters can be obtained.

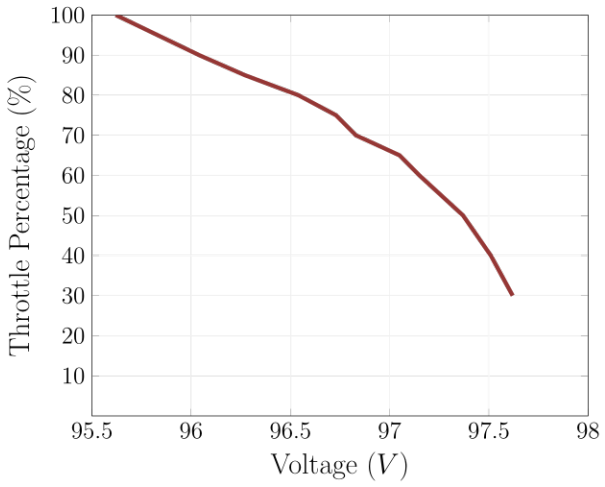

(a)

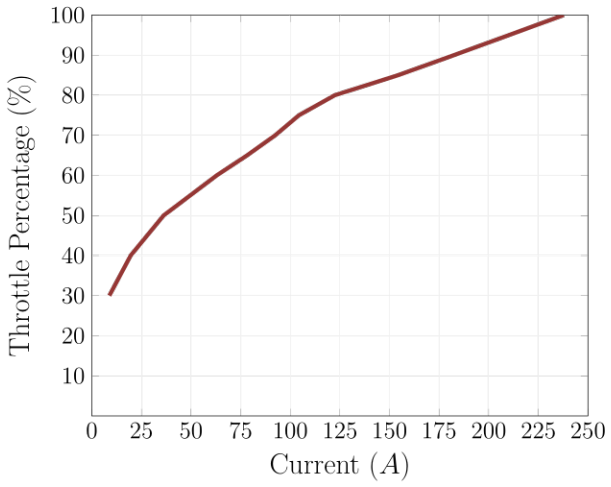

(b)

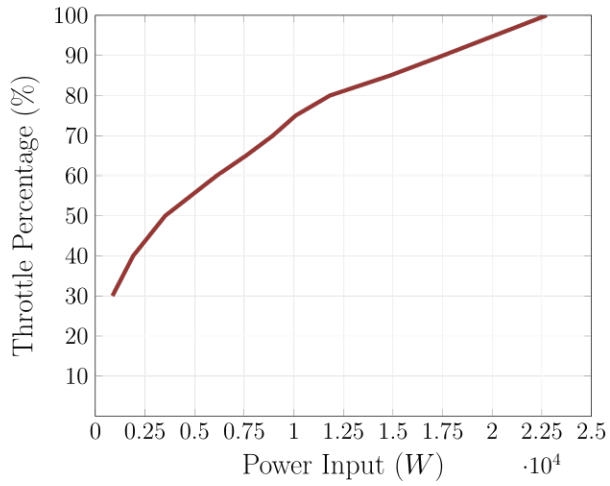

(c)

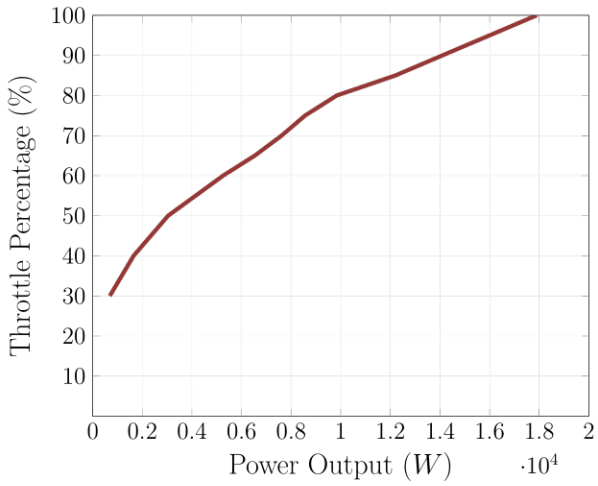

(d)

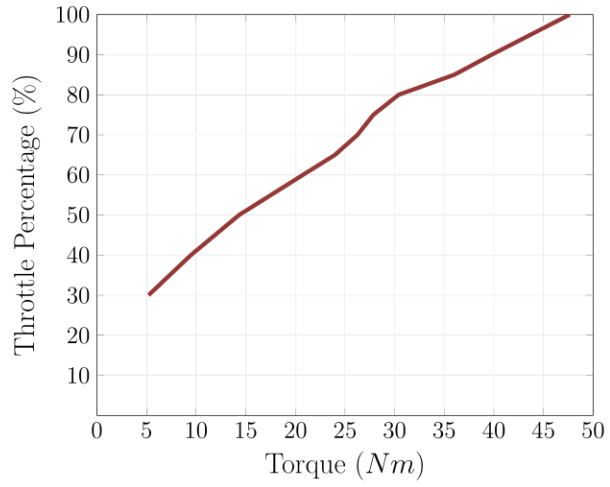

(e)

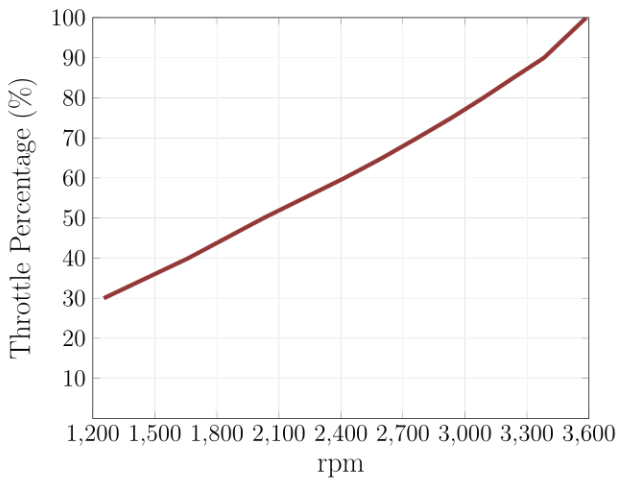

(f)

Figure 46: Motor Performance

Motor performance parameters are presented below at a reference voltage of 98 V with varying throttle levels.

Throttle (%)	**Voltage** (V)	**Current** (A)	**Input Power** (W)	**Output Power** (W)	**Torque** ($N-m$)	**RPM**	**Efficiency** (%)
40	97.51	19.58	1909.2	1647.7	9.468	1662	86.3
50	97.37	36.2	3524.8	3038.4	14.322	2026	86.2
60	97.15	62.96	6116.6	5254.1	20.75	2418	85.9
65	97.05	78.27	7596.1	6532.6	23.99	2600	85.1
70	96.83	92.43	8950	7616.4	26.26	2770	85.1
75	96.73	104.38	10096.7	8562	27.86	2935	84.8
80	96.54	122.47	11823.3	9836.9	30.41	3089	83.2
85	96.27	154.38	14862.2	12201.8	36.02	3235	82.1
90	96.04	182.54	17531.4	14095	39.79	3383	80.4
100	95.62	237.86	22744.2	17899.7	47.65	3587	78.7

Table 11: Theoretical Motor Data, Data obtained from reference [1]

A few observations can be made from the graphs, like the direct correlation between throttle and current, input power, output power, RPM, and Torque. Another inference to be drawn from the graphs is the RPM of the motor while delivering the output power for hover, climb and descent, which are all close to 2200 RPM. Similarly, the currents to be drawn during these phases are approximately 50 A.

15.4 Electronic Speed Control (ESC)

The speed of an electric motor is controlled and regulated with the help of an Electronic Speed Control (ESC), and it does so by adjusting the voltage and current supplied to the motor by the battery. It plays a crucial role in applications like UAVs, where precise speed regulation and motor control are of the essence. The speed of the motor can be controlled remotely by transmitting a signal from a radio transmitter. This signal is received by a receiver onboard the UAV and then sent to the flight controller board, which generates another appropriate signal, which is fed to the ESC. The signal fed to ESC determines the input voltage and current to the motor, thus changing the rotor speed and, accordingly, the lift generated [73]. The ESC chosen for the mission is the 'MAD AMPX300A HV ESC' [74] as the selected ESC unit to pair with the chosen motor.

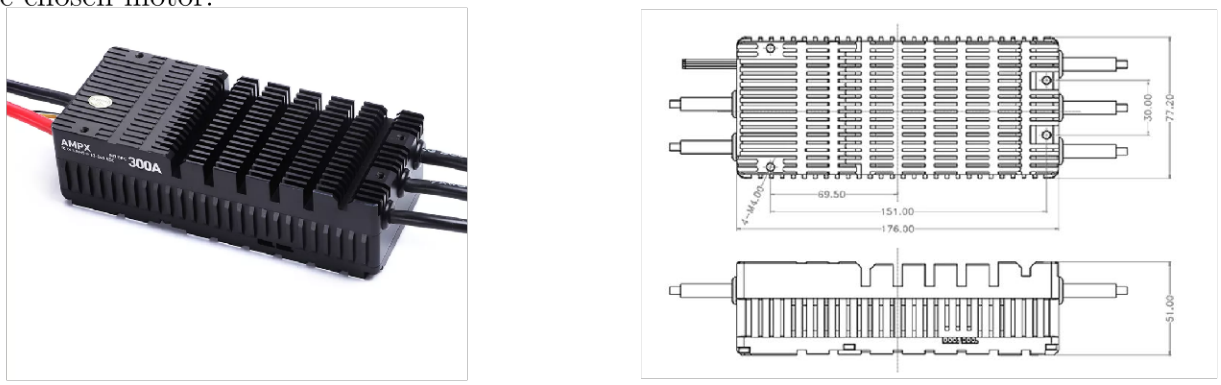

(a) ESC (b) ESC Dimensions

Figure 47: Electronic Speed Controller (ESC)

The specifications of the ESC are shown below.

Parameter	**Value**
Current Limit	300 A
Supported Lithium Cell Count	12-24S
Throttle Loss Protection	Supported
Temperature Protection	Supported
Compatible Signal Frequency	50-500 Hz
Operating Temperature	-20°C to 65°C
Dimensions	176 $mm\times$ 77.2 $mm\times$ 52 mm
Mass (excl. wires)	0.975 kg

Table 12: ESC Specifications

15.5 Payload Sensors

As stated earlier, the mission's objective is to study the deep layer of the Martian boundary layer, and accordingly, the payload to be carried is multiple sensors that will carry out high-resolution vertical profiling. The following sensors will be included in the payload.

Temperature Sensor: Crucial to capture temperature profiles to derive thermal processes, atmospheric stability and vertical transport processes in the Martian boundary layer. It makes use of a small bead thermistor for high-precision temperature measurements (Fig. 48). The expected mass of the sensor is 0.15 kg, and its power requirement is around 0.5 W.

Figure 48: Spherical Bead Thermistors

Pressure Sensor: Crucial to understanding global atmospheric dynamics, topography-driven pressure effects, CO_2 and dust cycles. It is made of a micro-machined capacitive pressure sensor head and transducer electronics for high-resolution vertical pressure profile measurements (Fig. 49). The expected mass of the sensor is 0.04 kg, and its power requirement is around 0.015 W.

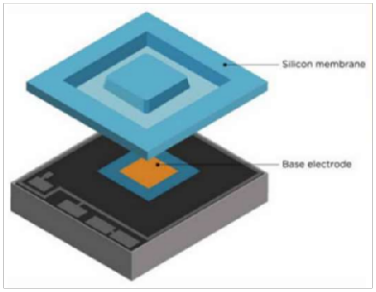

Figure 49: Pressure Sensor

Trace Species and Dust Sensor: Crucial to obtain the vertical distribution of dust aerosols and trace species such as CH_4, H_2O, H_2O_2 and N_2O and to gain new insights on the composition and dynamics of the boundary layer. It makes use of multiple low-powered diode lasers coupled with a multi-reflection optical cavity that enables the detection of extremely low concentrations (Fig. 50). The expected mass of the sensor is 2 kg, and its power requirement is around 20 W.

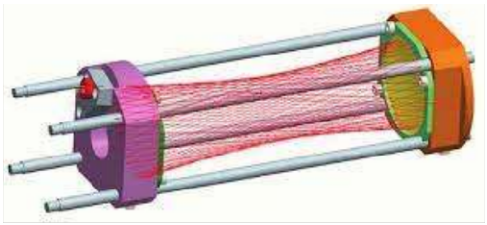

Figure 50: Herriott Cell-based Tunable Laser Spectrometer

Humidity Sensor: Crucial to understanding the distribution of H_2O in the atmosphere, the likelihood of stable near-surface ice and the habitability potential of Mars by measuring relative humidity in the near-surface layer. It makes use of an active polymer that changes sensor head capacitance as a function of relative humidity (Fig. 51). The expected mass is 0.045 kg, and its power requirement is around 0.02 W.

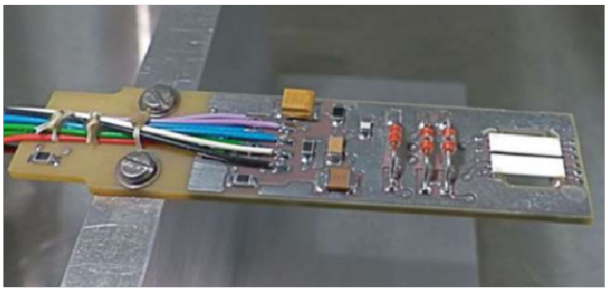

Figure 51: Humidity Sensor

Wind Sensor: Crucial to obtaining information on large-scale wind patterns, atmospheric waves, dust storms and insights on future Mars aerial vehicles by measuring wind speed and wind direction in the near-surface layer. It makes use of any of the three configurations, ranging from hot-wire anemometers to sonic anemometers and laser Doppler anemometers. The expected mass of the sensor is approximately 1 kg, and its power requirement is around 2 W.

Electric Field Sensor: Crucial to understanding the frictional charging of dust particles, which plays a significant role in the atmosphere chemistry and dynamics by measuring the atmospheric electric field. It makes use of a spherical electrode that obtains the atmospheric electric field by measuring the electric signal between a spherical electrode and the UAV (Fig. 52). The expected mass of the sensor is 1 kg, and its power requirement is around 20 W.

Figure 52: Electric Field Sensor

It must be noted that the total mass of the payload is considered to be 5 kg, as stated in the problem statement, and the total payload power requirement is observed to be 42 W, which is rounded off to 50 W for the sake of power calculations. All the data mentioned in the section are referenced from the updated

information on the payload sensors discussed in the 3^{rd} Webinar of NACDeC-7 on the MARtian Boundary Layer (MARBLE) Payload Suite.

16 Energy Balance

Since all the aspects of the UAV pertaining to aerodynamics, structures, and electronics have been discussed so far, have been discussed, we must now finalise the mission profile. A mission profile of a UAV includes a detailed plan outlining the sequence of activities and tasks that the UAV will perform during the mission. Before discussing the exact nature of our flight operation and its phases, we must understand the goal of the mission. As stated in the problem statement, the mission's goal is to maximise the total number of sorties while fulfilling the objective of studying the Martian boundary layer's Deep Roughness layer ($\leq 100\ m$) through multiple climbs and descents. The phases of flight are the climbing and descending phases, throughout which the sensors record data like pressure, temperature, humidity, wind speed, vertical distribution of dust aerosols, and electric field in this layer.

After understanding the goal and objectives of the mission, detailed characteristics of each phase must be discussed. We assume that the UAV starts the mission at sunrise with only a reserve battery that is 25% of the total battery capacity.

16.1 Climb

The climbing phase is crucial, considering the recording of the aforementioned data through various sensors. In order to ensure the proper functioning of sensors and accurate gradient data collection, a gradual rate of climb must be selected. After performing calculations for a range of rates of climb, it was decided to use 2 m/s as the rate of climb. Thus, the time to climb is around 50 seconds. The energy to climb is calculated using the required climb power from Fig. 20a, matching it to the output power from the motor and then getting the corresponding input power to the motor from Tab. 11 using the equation shown below.

$$\text{Climb Energy } (Wh) = \text{Motor Input Power } (W) \times \text{Climb Time } (h) \tag{116}$$

The energy to climb is observed to be around 132.35 Wh for two motors. It must be noted that this energy gets depleted from the batteries while climbing.

16.2 Hover

The hovering phase is a relatively insignificant phase of flight with respect to the mission since it is the vertical flight that is of the essence for data collection. However, the hover phase must be present, albeit short, to collect data at the peak altitude of 100 m. It was decided that the hover time would be 2 seconds, during which the UAV would slow down its ascent, hover for a while and then reverse the direction of flight by starting to descend. The energy to hover thus is calculated using the required hover power from Eq. 24, matching it to output power from the motor and then getting the corresponding input power to

the motor from Tab. 11 using the equation shown below.

$$\text{Hover Energy } (Wh) = \text{Motor Input Power } (W) \times \text{Hover Time } (h) \tag{117}$$

The energy to climb is observed to be around 5.11 Wh for two motors. It must be noted that this energy gets depleted from the battery while hovering.

16.3 Descent

The descending phase is very similar to the climbing phase in terms of data collection, the difference being that it will measure the gradient from 100 m - 0 m. Therefore, the rate of descent is chosen to be 2 m/s, which is the same as in the climb phase but in the opposite direction. Similarly, the descent time will also be 50 seconds. The energy to descend thus is calculated using the required descent power from Sec. 10.10, matching it to output Power from the motor and then getting the corresponding input power to the motor from Tab. 11 using the equation shown below.

$$\text{Descent Energy } (Wh) = \text{Motor Input Power } (W) \times \text{Descent Time } (h) \tag{118}$$

The energy to descend is observed to be around 123.71 Wh for two motors. It must be noted that this energy gets depleted from the battery while descending. The discussed mission profile is presented in a graphic manner below.

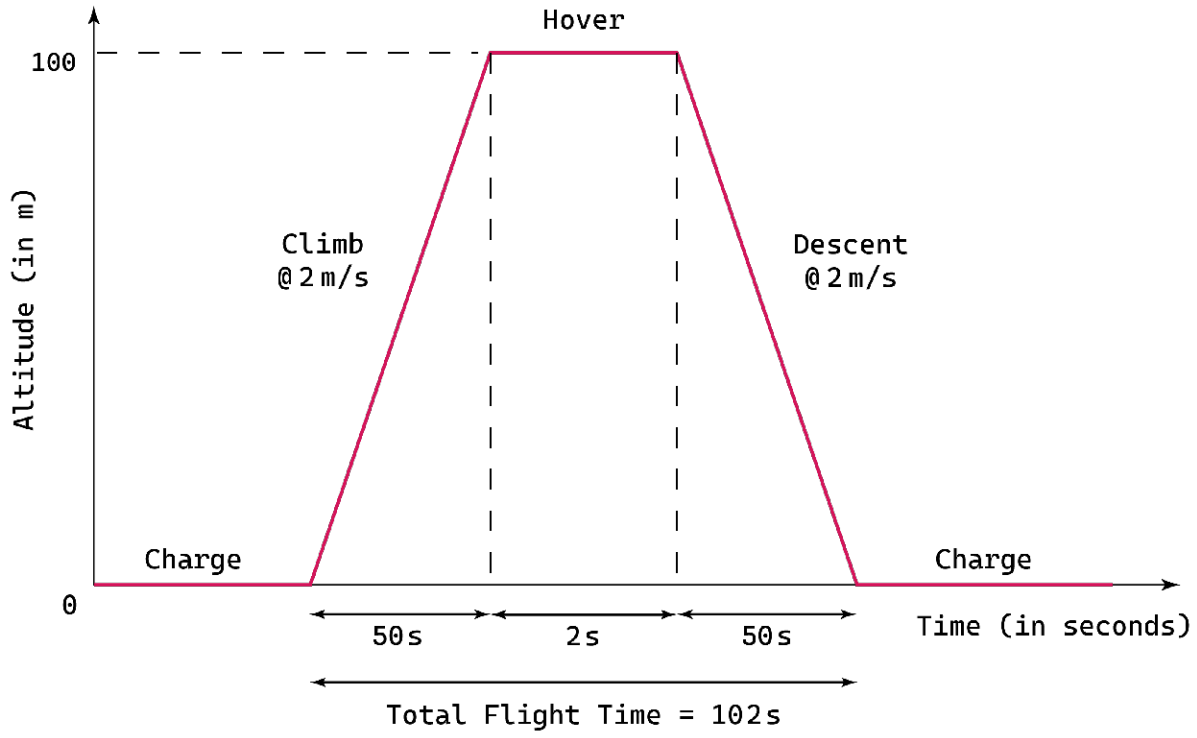

Figure 53: Mission Profile

This particular mission profile gives a flight time of 102 seconds and, in the process, depletes 261.17 Wh of energy from the battery. Since the total battery capacity of the two batteries is 540 Wh, this means

that the average depth of discharge of the battery is around 48%. By ensuring a DOD of only 48%, the battery health is improved by not draining it substantially, which in turn extends the life of the battery, allowing for more cycles of charging/discharging.

A detailed timeline of the charging and flying phases for half a Martian sol is provided in Sec. 19. The timeline takes into account the solar panel deployment and retraction time, as well as the waiting period before deploying the solar panels to allow the dust kicked up due to the rotors to settle. A waiting time of 100 seconds is also considered after the batteries have been charged, as suggested in the problem statement. From the timeline, it can be inferred that the total number of sorties in a sol is 20, and the total flight time in a sol is around 40 minutes. A typical mission day starts the day with the UAV being charged at 25%. Solar panels are deployed at sunrise, and batteries are allowed to charge fully. The UAV continues to perform flying (discharging) and charging phases while taking into account other waiting times. At sunset, the UAV batteries are 70% charged after completing the 20^{th} sortie.

16.4 Forward Flight

The usual mission profile consists of only the climb, hover and descent phases. However, forward flight is also considered an additional optional phase of flight that can be performed when needed. This can prove to be useful if there is a need to relocate to a different location for data collection or even if there is an emergency. Thus, it is crucial for the UAV to boast a long range while maintaining endurance.

This forward phase of flight is meant to replace the hover phase, and therefore, the modified mission profile then consists of the climb, forward and descent phases. In the previous case, the hover phase only lasted for 2 seconds, but for the forward flight phase, all the remaining energy will be depleted, i.e. the energy remaining after subtracting Climb Energy and Descent Energy from the Available Energy.

$$\text{Forward Energy} = \text{Available Energy - Climb Energy - Descent Energy} \tag{119}$$

$$\text{Forward Energy} = 405\ Wh \text{ - } 132.35\ Wh \text{ - } 123.71\ Wh = 148.94\ Wh \tag{120}$$

The forward flight velocity greatly affects the range and endurance of the UAV, and this was highlighted in detail in Fig. 25 of Sec. 10.12. The aforementioned can be used completely for forward flight, and the desired forward flight velocity, range, and endurance can be found. The modified timeline for this particular optional mission profile can be found in Sec. 19. In this timeline, it has been considered that forward flight is being performed in every sortie to obtain the minimum number of sorties. Since the depth of discharge in this case is 75% for every sortie, the charging time is increased, and thus, the number of sorties goes down to 15 sorties. At sunset, the UAV batteries are 100% charged after completing the 15^{th} sortie.

17 Mass Distribution

A detailed overview of the mass fraction of all the components used in the UAV is highlighted below.

Component	Mass (kg)
Avionics System	3.5
Battery Health Management System	7
Solar Panels (Including Mechanism)	18
Structure (Including Landing Gear)	18
Motors	5
Batteries	3
ESC	1
Payload	5
Propeller	6
Others	3.5
Total	70

Figure 54: Mass Breakdown

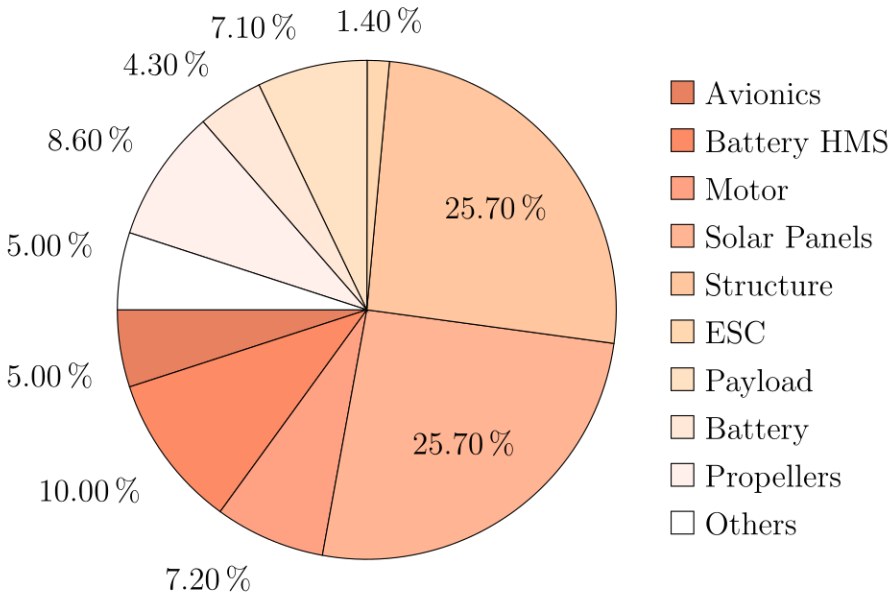

Figure 55: Mass Breakdown

18 Conclusion

The report started by defining the problem statement, followed by a preliminary analysis. Henceforth, Martian reference atmosphere and solar irradiance models were explicated upon. This was followed by proposing an expected mission profile and considering the features and limitations of the configurations proposed previously until we eventually selected the coaxial single-rotor system to be the most suitable configuration for our problem statement and the anticipated mission profile. Further, the entry, descent and landing (EDL) of our UAV were considered, and the challenges faced were elaborated on in Sec. 6. The analytical performance calculations were justified and validated, some with numerical results. Moreover, autorotative descent was considered and was deemed to be impractical for our mission profile. Furthermore, the forward flight performance was also studied, which allowed for the parametric study of the range and endurance of our UAV with forward flight speed.

Unsteady propeller CFD analysis was carried out using XFlow to study flow interactions and validate certain analytical results. Once the stowage and final configuration were determined, a comprehensive structural analysis was carried out. This included an investigation of possible materials that could be incorporated, consideration of the manufacturability of the UAV, design of the landing gear, and integration of all the electronics and other components into the UAV pod.

Furthermore, the structural integrity of both the pod and the landing gear was carried out to determine if the deformations sustained during the continuous operation of the UAV would remain within safe and acceptable operating limits. Thereafter, an extensive study of the flight dynamics, introducing the potential reference frames and detailing the various mathematical modelling techniques that could be implemented

to study the kinematic behaviour and dynamic response of our UAV, was proposed. Finally, the energy balance of the UAV was reworked to adhere as closely as possible to the intended mission profile.

Overall, the purpose of this report was to provide a comprehensive methodology for the conceptual design of a UAV which could be feasibly operated on Mars, adhering to the required mission profile, to be able to perform 100 m sorties in the Martian atmosphere multiple times a sol.

19 Appendices

Appendix A: Sample Calculations for Mission Timeline

This section highlights the calculations done to obtain battery charging time, charging current, and other parameters that are crucial for developing a precise timeline for the mission. The calculations shown below are performed for one set of battery-motor combinations and for the usual mission profile (hover).

$$\text{Battery Ah} = \frac{1.5\ kg \times 180\ Wh}{100\ V} = 2.7\ Ah \tag{121}$$

In order to calculate the solar power being collected from the panels, the average irradiance during the charging period must be obtained first. This is done by assuming a certain time period, taking its average irradiance, and then calculating the charge time it results in. If the charge time matches the earlier assumed time period, then we take it as the actual charging time or else repeat it till it matches. Therefore, the average irradiance between two time points, t1 and t2, is given by,

$$\text{Avg. Irradiance} = \frac{Irr_1 + Irr_2}{2} \tag{122}$$

For the sake of this calculation, let us consider the 1st charging period from 06:02 to 08:02, as shown in Sec. 19. Therefore, referring to Fig. 5, the average irradiance in this time period comes out to be around 48 W/m^2.From this value of average irradiance, the solar power can be calculated,

$$\text{Solar Power} = 17\% \times 25\ m^2 \times 48\ W/m^2 = 204\ W \tag{123}$$

The solar power obtained from the panels will be then split equally to supply energy to the two batteries. The charging current of each battery is calculated in the following way,

$$\text{Charge Current} = \frac{0.5 \times 204}{100\ V} = 1.02\ A \tag{124}$$

The charge time of the battery can then be calculated in the following way,

$$\text{Charge Time} = \frac{\%DOD \times 2.7\ Ah}{1.02\ A} = 1.98\ hrs \tag{125}$$

It must be noted that %DOD was taken as 75% in this case because the UAV starts the mission day with only 25% reserve battery, and %DOD would be around 48% for other sortie cycles.

Appendix B: Detailed Mission Profile (Hover)

Time (hrs)	Activity	Time (hrs)	Activity
06:00 - 06:02	Solar Panel Deployment	10:33 - 10:35	100s Wait
06:02 - 08:02	Charging	10:35 - 10:37	Solar Panel Retraction
08:02 - 08:04	100s Wait	10:37 - 10:39	**6th Sortie**
08:04 - 08:06	Solar Panel Retraction	10:39 - 10:44	Dust Settling Time
08:06 - 08:08	**1st Sortie**	10:44 - 10:46	Solar Panel Deployment
08:08 - 08:13	Dust Settling Time	10:46 - 10:56	Charging
08:13 - 08:15	Solar Panel Deployment	10:56 - 10:58	100s Wait
08:15 - 08:45	Charging	10:58 - 11:00	Solar Panel Retraction
08:45 - 08:47	100s Wait	11:00 - 11:02	**7th Sortie**
08:47 - 08:49	Solar Panel Retraction	11:02 - 11:07	Dust Settling Time
08:49 - 08:51	**2nd Sortie**	11:07 - 11:09	Solar Panel Deployment
08:51 - 08:56	Dust Settling Time	11:09 - 11:19	Charging
08:56 - 08:58	Solar Panel Deployment	11:19 - 11:21	100s Wait
08:58 - 09:16	Charging	11:21 - 11:23	Solar Panel Retraction
09:16 - 09:18	$100\,s$ Wait	11:23 - 11:25	**8th Sortie**
09:18 - 09:20	Solar Panel Retraction	11:25 - 11:30	Dust Settling Time
09:20 - 09:22	**3rd Sortie**	11:30 - 11:32	Solar Deployment Time
09:22 - 09:27	Dust Settling Time	11:32 - 11:41	Charging
09:27 - 09:29	Solar Panel Deployment	11:41 - 11:43	$100\,s$ Wait
09:29 - 09:44	Charging	11:43 - 11:45	Solar Panel Retraction
09:44 - 09:46	$100\,s$ Wait	11:45 - 11:47	**9th Sortie**
09:46 - 09:48	Solar Panel Retraction	11:47 - 11:52	Dust Settling Time
09:48 - 09:50	**4th Sortie**	11:52 - 11:54	Solar Panel Deployment
09:50 - 09:55	Dust Settling Time	11:54 - 12:03	Charging
09:55 - 09:57	Solar Panel Deployment	12:03 - 12:05	$100\,s$ Wait
09:57 - 10:09	Charging	12:05 - 12:07	Solar Panel Retraction
10:09 - 10:11	$100\,s$ Wait	12:07 - 12:09	**10th Sortie**
10:11 - 10:13	Solar Panel Retraction	12:09 - 12:14	Dust Settling Time
10:13 - 10:15	**5th Sortie**	12:14 - 12:16	Solar Panel Deployment
10:15 - 10:20	Dust Settling Time	12:16 - 12:25	Charging
10:20 - 10:22	Solar Panel Deployment	12:25 - 12:27	$100\,s$ Wait
10:22 - 10:33	Charging	12:27 - 12:29	Solar Panel Retraction

Table 13: Timeline of the Mission Profile (since Sunrise)

12:29 - 12:31	**11th Sortie**	14:53 - 14:55	**17th Sortie**
12:31 - 12:36	Dust Settling Time	14:55 - 15:00	Dust Settling Time
12:36 - 12:38	Solar Panel Deployment	15:00 - 15:02	Solar Panel Deployment
12:38 - 12:47	Charging	15:02 - 15:20	Charging
12:47 - 12:49	100 s Wait	15:20 - 15:22	100 s Wait
12:49 - 12:51	Solar Panel Retraction	15:22 - 15:24	Solar Panel Retraction
12:51 - 12:53	**12th Sortie**	15:24 - 15:26	**18th Sortie**
12:53 - 12:58	Dust Settling Time	15:26 - 15:31	Dust Settling Time
12:58 - 13:00	Solar Panel Deployment	15:31 - 15:33	Solar Panel Deployment
13:00 - 13:10	Charging	15:33 - 15:56	Charging
13:10 - 13:12	100 s Wait	15:56 - 15:58	100 s Wait
13:12 - 13:14	Solar Panel Retraction	15:58 - 16:00	Solar Panel Retraction
13:14 - 13:16	**13th Sortie**	16:00 - 16:02	**19th Sortie**
13:16 - 13:21	Dust Settling Time	16:02 - 16:07	Dust Settling Time
13:21 - 13:23	Solar Panel Deployment	16:07 - 16:09	Solar Panel Deployment
13:23 - 13:33	Charging	16:09 - 16:49	Charging
13:33 - 13:35	100 s Wait	16:49 - 16:51	100 s Wait
13:35 - 13:37	Solar Panel Retraction	16:51 - 16:53	Solar Panel Retraction
13:37 - 13:39	**14th Sortie**	16:53 - 16:55	**20th Sortie**
13:39 - 13:44	Dust Settling Time	16:55 - 17:00	Dust Settling Time
13:44 - 13:46	Solar Panel Deployment	17:00 - 17:02	Solar Panel Deployment
13:46 - 13:57	Charging	17:02 - 18:18	Charge
13:57 - 13:59	100 s Wait	18:18 - 18:20	Solar Panel Retraction
13:59 - 14:01	Solar Panel Retraction		
14:01 - 14:03	**15th Sortie**		
14:03 - 14:08	Dust Settling Time		
14:08 - 14:10	Solar Panel Deployment		
14:10 - 14:22	Charging		
14:22 - 14:24	100 s Wait		
14:24 - 14:26	Solar Panel Retraction		
14:26 - 14:28	**16th Sortie**		
14:28 - 14:33	Dust Settling Time		
14:33 - 14:35	Solar Panel Deployment		
14:35 - 14:49	Charging		
14:49 - 14:51	100 s Wait		
14:51 - 14:53	Solar Panel Retraction		

Table 14: Timeline of the Mission Profile (till Sunset)

Appendix C: Detailed Mission Profile (Forward Flight)

Time (hrs)	Activity	Time (hrs)	Activity
06:00 - 06:02	Solar Panel Deployment	11:03 - 11:05	100 s Wait
06:02 - 08:02	Charging	11:05 - 11:07	Solar Panel Retraction
08:02 - 08:04	100 s Wait	11:07 - 11:10	**6th Sortie**
08:04 - 08:06	Solar Panel Retraction	11:10 - 11:15	Dust settling Time
08:06 - 08:09	**1st Sortie**	11:15 - 11:17	Solar Panel Deployment
08:09 - 08:14	Dust Settling Time	11:17 - 11:32	Charging
08:14 - 08:16	Solar Panel Deployment	11:32 - 11:34	100 s Wait
08:16 - 08:46	Charging	11:34 - 11:36	Solar Panel Retraction
08:46 - 08:48	100 s Wait	11:36 - 11:39	**7th Sortie**
08:48 - 08:50	Solar Panel Retraction	11:39 - 11:44	Dust Settling Time
08:50 - 08:53	**2nd Sortie**	11:44 - 11:46	Solar Panel Deployment
08:53 - 08:58	Dust Settling Time	11:46 - 12:00	Charging
08:58 - 09:00	Solar Panel Deployment	12:00 - 12:02	100 s Wait
09:00 - 09:26	Charging	12:02 - 12:04	Solar Panel Retraction
09:26 - 09:28	100 s Wait	12:04 - 12:07	**8th Sortie**
09:28 - 09:30	Solar Panel Retraction	12:07 - 12:12	Dust Settling Time
09:30 - 09:33	**3rd Sortie**	12:12 - 12:14	Solar Panel Deployment
09:33 - 09:38	Dust Settling Time	12:14 - 12:28	Charging
09:38 - 09:40	Solar Panel Deployment	12:28 - 12:30	100 s Wait
09:40 - 10:00	Charging	12:30 - 12:32	Solar Panel Retraction
10:00 - 10:02	100 s Wait	12:32 - 12:35	**9th Sortie**
10:02 - 10:04	Solar Panel Retraction	12:35 - 12:40	Dust Settling Time
10:04 - 10:07	**4th Sortie**	12:40 - 12:42	Solar Panel Deployment
10:07 - 10:12	Dust Settling Time	12:42 - 12:58	Charging
10:12 - 10:14	Solar Panel Deployment	12:58 - 13:00	100 s Wait
10:14 - 10:32	Charging	13:00 - 13:02	Solar Panel Retraction
10:32 - 10:34	100 s Wait	13:02 - 13:05	**10th Sortie**
10:34 - 10:36	Solar Panel Retraction	13:05 - 13:10	Dust Settling Time
10:36 - 10:39	**5th Sortie**	13:10 - 13:12	Solar Panel Deployment
10:39 - 10:44	Dust Settling Time	13:12 - 13:27	Charging
10:44 - 10:46	Solar Panel Deployment	13:27 - 13:29	100 s Wait
10:46 - 11:03	Charging	13:29 - 13:31	Solar Panel Retraction

Table 15: Timeline of the Mission Profile (since Sunrise)

13:31 - 13:34	**11th Sortie**	15:14 - 15:17	**14th Sortie**
13:34 - 13:39	Dust Settling Time	15:17 - 15:22	Dust Settling Time
13:39 - 13:41	Solar Panel Deployment	15:22 - 15:24	Solar Panel Deployment
13:41 - 13:58	Charging	15:24 - 16:00	Charging
13:58 - 14:00	100 s Wait	16:00 - 16:02	100 s Wait
14:00 - 14:02	Solar Panel Retraction	16:02 - 16:04	Solar Panel Retraction
14:02 - 14:05	**12th Sortie**	16:04 - 16:07	**15th Sortie**
14:05 - 14:10	Dust Settling Time	16:07 - 16:12	Dust Settling Time
14:10 - 14:12	Solar Panel Deployment	16:12 - 16:14	Solar Panel Deployment
14:12 - 14:32	Charging	16:14 - 18:00	Charging
14:32 - 14:34	100 s Wait	18:00 - 18:02	Solar Panel Retraction
14:34 - 14:36	Solar Panel Retraction		
14:36 - 14:39	**13th Sortie**		
14:39 - 14:44	Dust Settling Time		
14:44 - 14:46	Solar Panel Deployment		
14:46 - 15:10	Charging		
15:10 - 15:12	100 s Wait		
15:12 - 15:14	Solar Panel Retraction		

Table 16: Timeline of the Mission Profile (till Sunset)

Appendix D: Planform Drawing of the UAV

TOP VIEW

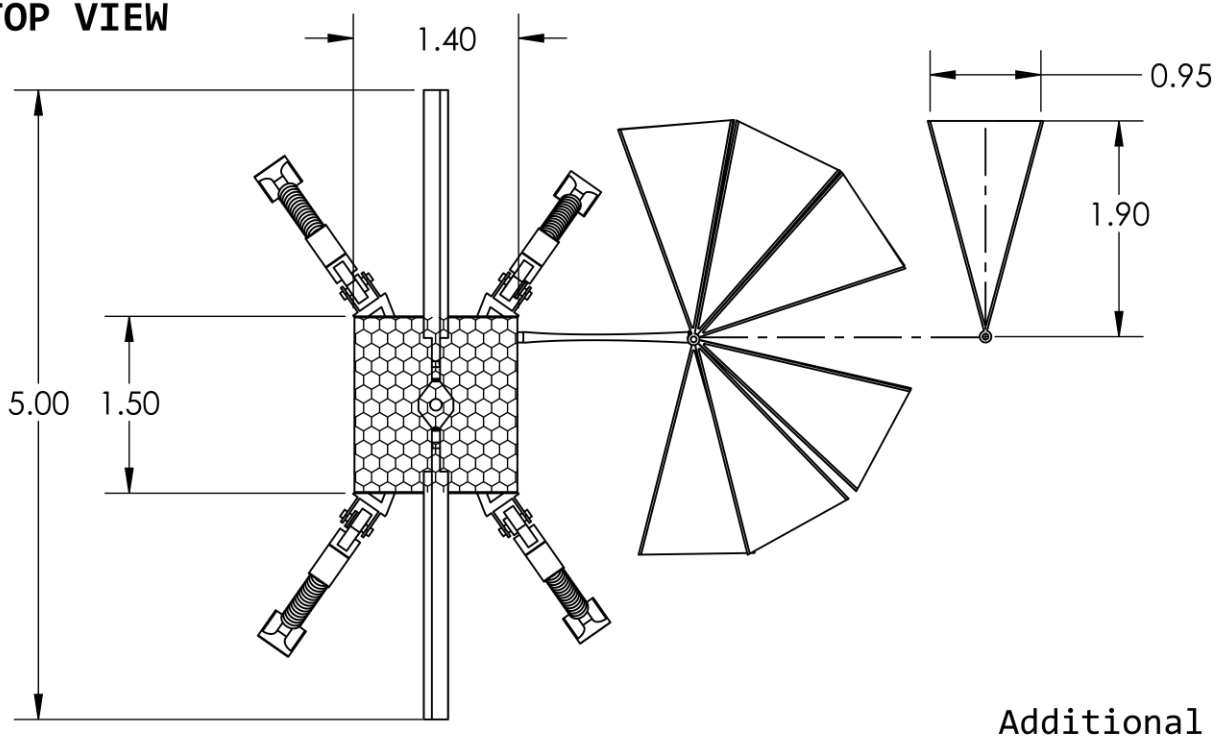

Team Name: FLIGHTFORGE

Manipal Institute of Technology

Parameter	Value
Total UAV Mass	70 kg
Rotor Diameter	5 m
Total Panel Area	25 sq. m
No. of Solar Panel Sections	11+11+2+1 = 25

LEFT VIEW

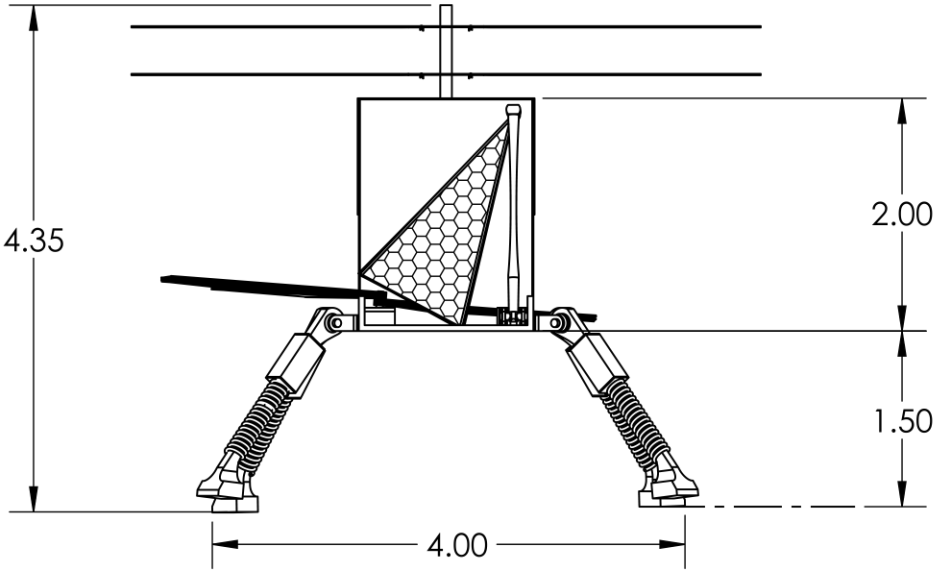

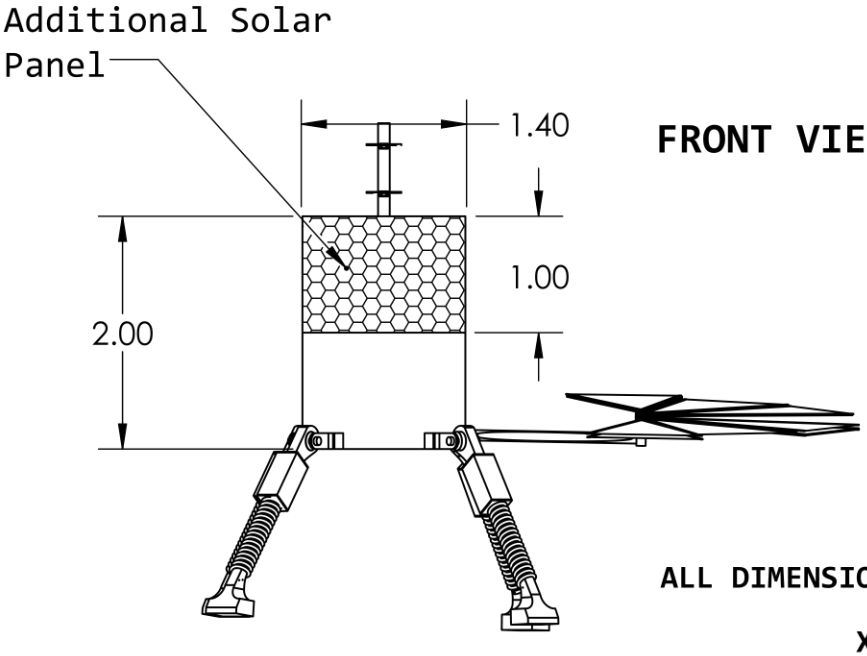

FRONT VIEW

SCALE 1:65
ALL DIMENSIONS IN METER
TOLERANCE:
X.X = ± .2 m
X.XX = ± .20 m

Appendix E: References

[1] "MAD M40C30 PRO IPE Brushless Motor," `https://www.mad-motor.com/products/mad-components-m40c30-pro-ipe.html`, 2015. [Online; Accessed: January 2024].

[2] Braun, R. D., and Manning, R. M., "Mars Exploration Entry, Descent, and Landing Challenges," *Journal of Spacecraft and Rockets*, Vol. 44, No. 2, 2007, pp. 310–323. https://doi.org/10.2514/1.25116.

[3] Johnson, W., *Rotorcraft Aeromechanics*, Cambridge, 2013.

[4] Dambhare, M. V., Butey, B., and Moharil, S. V., "Solar photovoltaic technology: A review of different types of solar cells and its future trends," 2021. URL https://iopscience.iop.org/article/10.1088/1742-6596/1913/1/012053.

[5] Shefali, U., Deepak, S., and Varun, S., "Tangential winds of a vortex system in a planetary surface layer," *Journal of Earth System Science*, Vol. 129, 2020. https://doi.org/10.1007/s12040-019-1268-5.

[6] Patrick L., B., and Dr. Tony, P., "The Lure of Hematite," https://web.archive.org/web/20100114043500/http://science.nasa.gov/headlines/y2001/ast28mar_1.htm, 3 2001. Accessed: February 2024.

[7] "Mariner 4," https://science.nasa.gov/mission/mariner-4/, 11 2023. Accessed: February 2024.

[8] Mason, P., "The History of Mars Exploration," https://sci.esa.int/documents/33745/35957/1567254235744-04_Masson.pdf, 2 2005. Accessed: February 2024.

[9] "Mars Fact Sheet," https://web.archive.org/web/20200317184127/https://nssdc.gsfc.nasa.gov/planetary/factsheet/marsfact.html, 9 2018. [Online; Accessed: February 2024].

[10] "Mars Facts," https://science.nasa.gov/mars/facts/, 1 2024. [Online; Accessed: February 2024].

[11] Authors, "Abundance and Isotopic Composition of Gases in the Martian Atmosphere from the Curiosity Rover," *Science*, Vol. 341, No. 6143, 2013, pp. 263–266. https://doi.org/10.1126/science.1237966, the authors aren't explicitly mentioned due to the sheer number of authors (449).

[12] Jakosky, B. M., "How did Mars lose its atmosphere and water?" *Physics Today*, Vol. 75, No. 4, 2022, pp. 62–63. https://doi.org/10.1063/PT.3.4988.

[13] Authors, "In situ recording of Mars soundscape," *Nature*, Vol. 605, 2022. https://doi.org/10.1038/s41586-022-04679-0, the authors aren't explicitly mentioned due to the sheer number of authors.

[14] "Mars Facts," https://mars.nasa.gov/all-about-mars/facts/, 2000. [Online; Accessed: February 2024].

[15] "Mars Exploration Rover – Spirit," https://science.nasa.gov/mission/mer-spirit/, 2024. [Online; Accessed June 2024].

[16] "Mars Exploration Rover – Opportunity," https://science.nasa.gov/mission/mer-opportunity/, 2024. [Online; Accessed June 2024].

[17] "Mars Science Laboratory – Curiosity Rover," https://science.nasa.gov/mission/msl-curiosity/, 2024. [Online; Accessed June 2024].

[18] "Mars 2020 – Perseverance Rover," https://science.nasa.gov/mission/mars-2020-perseverance/, 2024. [Online; Accessed June 2024].

[19] Nazari-Sharabian, M., Aghababaei, M., Karakouzian, M., and Karami, M., "Water on Mars—A Literature Review," *Galaxies*, Vol. 8, No. 2, 2020. https://doi.org/10.3390/galaxies8020040.

[20] Authors, "The Mars Climate Database (Version 6.1)," *Europlanet Science Congress 2022*, 2022. https://doi.org/10.5194/epsc2022-786, the authors aren't explicitly mentioned due to the sheer number of authors.

[21] Rau, H. E., *Solar Energy Fundamentals and Systems*, Springer, 1999.

[22] Woolf, R., *Introduction to Renewable Energy*, Elsevier, 2008.

[23] Kreith, F., *Principles of Solar Engineering*, Taylor & Francis Group, 2015.

[24] Munk, M. M., "Mars Entry, Descent and Landing (EDL)," https://www.kiss.caltech.edu/workshops/access2mars/presentations/Munk.pdf, 3 2021. [Online; Accessed June 2024].

[25] Grover, M. R., Cichy, B. D., and Desai, P. N., "Overview of the Phoenix Entry, Descent, and Landing System Architecture," *Journal of Spacecraft and Rockets*, Vol. 48, No. 5, 2011, pp. 706–712. https://doi.org/10.2514/1.46548.

[26] Desai, P. N., Prince, J. L., Queen, E. M., Schoenenberger, M. M., Cruz, J. R., and Grover, M. R., "Entry, Descent, and Landing Performance of the Mars Phoenix Lander," *Journal of Spacecraft and Rockets*, Vol. 48, No. 5, 2011, pp. 798–808. https://doi.org/10.2514/1.48239.

[27] Richard G. Lee, S. A. S., Koushil Sreenath, "Modeling and Control of Coaxial UAV with Swashplate Controlled Lower Propeller," 2016. URL https://api.semanticscholar.org/CorpusID:18561117.

[28] Sørensen, J. N., "2.07 - Aerodynamic Analysis of Wind Turbines," *Comprehensive Renewable Energy (Second Edition)*, edited by T. M. Letcher, Elsevier, Oxford, 2022, second edition ed., pp. 172–193. https://doi.org/https://doi.org/10.1016/B978-0-12-819727-1.00127-8.

[29] Gudmundsson, S., "Chapter 14 - The Anatomy of the Propeller," *General Aviation Aircraft Design*, edited by S. Gudmundsson, Butterworth-Heinemann, Boston, 2014, pp. 581–659. https://doi.org/https://doi.org/10.1016/B978-0-12-397308-5.00014-3.

[30] Landgrebe, A. J., "An Analytical and Experimental Investigation of Helicopter Rotor Hover Performance and Wake Geometry Characteristics," Tech. rep., UNITED AIRCRAFT RESEARCH LABS EAST HARTFORD CT, 1969.

[31] Koning, W., Romander, E., and Johnson, W., "Optimization of Low Reynolds Number Airfoils for

Martian Rotor Applications Using an Evolutionary Algorithm," 2020. https://doi.org/10.2514/6.2020-0084.

[32] Schmitz, F. W., "Aerodynamics of the model airplane. Part 1 - Airfoil measurements," Tech. rep., NASA Marshall Space Flight Center, 1967.

[33] Witold J. K. Koning, W. J., Ethan A. Romander, "Low Reynolds Number Airfoil Evaluation for the Mars Helicopter Rotor," 2018.

[34] Eastman N. Jacobs, A. S., "Airfoil Section Characteristics As Affected by Variations of the Reynolds Number," Tech. rep., NACA-NRTS, 1937. Accessed: January 2024.

[35] Selig, M. S., "Summary of low speed airfoil data," 1995. URL https://api.semanticscholar.org/CorpusID:108726509.

[36] Coleman, C. P., "A Survey of Theoretical and Experimental Coaxial Rotor Aerodynamic Research," Tech. rep., Ames Research Center, 1997.

[37] Rand, O., and Khromov, V., "Aerodynamic optimization of coaxial rotor in hover and axial flight," *27th Congress of the International Council of the Aeronautical Sciences 2010, ICAS 2010*, Vol. 2, 2010.

[38] Prior, S. D., "Reviewing and Investigating the Use of Co-Axial Rotor Systems in Small UAVs," *International Journal of Micro Air Vehicles*, Vol. 2, No. 1, 2010, pp. 1–16. https://doi.org/10.1260/1756-8293.2.1.1.

[39] Fernandes, S. D., "Performance analysis of a coaxial helicopter in hover and forward flight," , 2017.

[40] Kim, H., and Brown, R., "A Comparison of Coaxial and Conventional Rotor Performance," *Journal of the American Helicopter Society*, Vol. 55, 2010, pp. 12004–1. https://doi.org/10.4050/JAHS.55.012004.

[41] *Engineering Design Handbook, Helicopter Engineering, Part 1, Preliminary Design*, US Army Material Command, 1974.

[42] "Airbus service Technical report (3297-S-00)," https://www.airbus.com/sites/g/files/jlcbta136/files/2021-10/3297-S-00-Rev-0-EN.pdf, 2019. [Online; Accessed May 2024].

[43] Kim, K. C., "Analytical Calculations of Helicopter Torque Coefficient and Thrust Coefficient Values for the Helicopter Performance (HELPE) Model," Tech. rep., Army Research Laboratory, 1999.

[44] Gessow, A., and Tapscott, R. J., "Charts for estimating performance of high-performance helicopters, Technical note 3323," Tech. rep., National Advisory Committee for Aeronautics, 1955.

[45] Lim, J., McAlister, K., and Johnson, W., "Hover Performance Correlation for Full-Scale and Model-Scale Coaxial Rotors," *Journal of the American Helicopter Society*, Vol. 54, 2009, pp. 32005–1. https://doi.org/10.4050/JAHS.54.032005.

[46] "Helicopter hover power calculator," https://www.spinningwing.com/hover-power-calculator/, 2021.

[47] Jr., R. M. M., "Experimental Studies in Helicopter Vertical Climb Performance," Tech. rep., NASA, 1996.

[48] "Autorotation Calculator," https://www.spinningwing.com/autorotation-calculator/, 2021.

[49] Wald, Q. R., "The aerodynamics of propellers," *Progress in Aerospace Sciences*, Vol. 42, No. 2, 2006, pp. 85–128. https://doi.org/https://doi.org/10.1016/j.paerosci.2006.04.001.

[50] Sahinoz, A., "Landing Gear Design and Stability Evaluation of a Lunar Lander," Ph.D. thesis, 04 2012. https://doi.org/10.13140/RG.2.2.13160.83202.

[51] Talekar, A., Dabholkar, A., Thombe, A., Jethwa, K., and Bhopale, N., "Design and Analysis of a Lunar Lander's Landing System," *Journal of Aircraft and Spacecraft Technology*, Vol. 5, 2021, pp. 41–50. https://doi.org/10.3844/jastsp.2021.41.50.

[52] Padfield, G. D., *Helicopter Flight Dynamics: The Theory and Application of Flying Qualities and Simulation Modelling, Second Edition*, Wiley-Blackwell, 2007.

[53] Chen, R., Yuan, Y., and Thomson, D., "A review of mathematical modelling techniques for advanced rotorcraft configurations," *Progress in Aerospace Sciences*, Vol. 120, 2020. https://doi.org/10.1016/j.paerosci.2020.100681.

[54] Bailey, J. E., Prasanth, R. K., and Krishnakumar, K., "ARMCOP Helicopter Flight and Engine Model for the UH-1 TRS Simulator," https://www.worldcat.org/title/armcop-helicopter-flight-and-engine-model-for-the-uh-1-trs-simulator/oclc/25517551, 1991.

[55] Howlett, J. J., "UH-60A Black Hawk Engineering Simulation Program. Volume 1: Mathematical Model," https://ntrl.ntis.gov/NTRL/dashboard/searchResults/titleDetail/N8428806.xhtml, 1981.

[56] Celi, R., "HeliUM 2 Flight Dynamic Simulation Model: Development, Technical Concepts, and Applications," *Proceedings of the 71st Annual Forum of the American Helicopter Society*, 2015.

[57] Leishman, J. G., and Beddoes, T. S., "A Generalised Model for Airfoil Unsteady Aerodynamic Behaviour and Dynamic Stall Using the Indicial Method," *Proceedings of the 42nd Annual Forum of the American Helicopter Society*, Washington, DC, 1986.

[58] Leishman, J. G., "Modeling Sweep Effects on Dynamic Stall," *Journal of the American Helicopter Society*, Vol. 34, No. 3, 1989, pp. 18–29. https://doi.org/10.4050/JAHS.34.3.18.

[59] Leishman, J. G., and Beddoes, T. S., "A Semi-Empirical Model for Dynamic Stall," *Journal of the American Helicopter Society*, Vol. 34, No. 3, 1989, pp. 3–17. https://doi.org/10.4050/JAHS.34.3.3.

[60] Truong, V. K., "A 2-D Dynamic Stall Model Based on a Hopf Bifurcation," *Proceedings of the 19th European Rotorcraft Forum*, ERF, Cernobbio, 1993, p. 23.

[61] Ortun, B., et al., "Rotor Loads Prediction on the ONERA 7A Rotor Using Loose Fluid/Structure Coupling," *Journal of the American Helicopter Society*, Vol. 62, No. 3, 2017, pp. 1–13. https://doi.org/10.4050/JAHS.62.032005.

[62] Truong, K.-V., Yeo, H., and Ormiston, A. R., "Structural Dynamics Modeling of Rectangular Rotor Blades," *Aerospace Science and Technology*, Vol. 30, No. 1, 2013, pp. 293–305. https://doi.org/10.1016/j.ast.2013.08.014.

[63] Carpenter, P. J., and Bernard, F., "Effect of a Rapid Blade-Pitch Increase on the Thrust and Induced-Velocity Response of a Full-Scale Helicopter Rotor," https://ntrs.nasa.gov/citations/19930083686, 1953.

[64] Pitt, D. M., and Peters, D. A., "Theoretical Prediction of Dynamic-Inflow Derivatives," *16th European Rotorcraft and Powered Lift Aircraft Forum*, Bristol, England, 1980.

[65] Ferguson, K., and Douglas, T., "Examining the Stability Derivatives of a Compound Helicopter," *The Aeronautical Journal*, Vol. 121, No. 1235, 2017, pp. 1–20. https://doi.org/10.1017/aer.2016.101.

[66] Turnour, S. R., and Celi, R., "Modeling of Flexible Rotor Blades for Helicopter Flight Dynamics Applications," *Journal of the American Helicopter Society*, Vol. 41, No. 1, 1996, pp. 52–66. https://doi.org/10.4050/JAHS.41.52.

[67] "Understand the Advantages, Disadvantages of Different Solar Cells," https://www.solar-facts-and-advice.com/solar-cells.html, 1 2012. [Online; Accessed: February 2024].

[68] Pflaum, C., Riffelmacher, T., and Jocher, A., "Design and route optimisation for an airship with onboard solar energy harvestin," *International Journal of Sustainable Energy*, 2023. https://doi.org/10.1080/14786451.2023.2189488.

[69] Kim, H., and Xu, D., "Effects of Layer Thickness on the Residual Stresses of CIGS Solar Cells with Polyimide Substrate," *Scientific Research Publishing (SCIRP)*, 2022. https://doi.org/10.4236/ampc.2022.129014.

[70] Ong, K. H., Agileswari, R., Maniscalco, B., Arnou, P., Kumar, C. C., Bowers, J. W., and Marsadek, M. B., "Review on Substrate and Molybdenum Back Contact in CIGS Thin Film Solar Cell," *International Journal of Photoenergy*, 2018. https://doi.org/10.1155/2018/9106269.

[71] Zhang, J., Wang, W., Zhou, S., Yang, H., and Chen, C., "Transparent dust removal coatings for solar cell on mars and its Anti-dust mechanism," *Progress in Organic Coatings*, Vol. 134, 2019, pp. 312–322. https://doi.org/10.1016/j.porgcoat.2019.05.028.

[72] Hossain, M. I., Ali, A., Bermudez Benito, V., Figgis, B., and Aïssa, B., "Anti-Soiling Coatings for Enhancement of PV Panel Performance in Desert Environment: A Critical Review and Market Overview," *Materials*, Vol. 15, No. 20, 2022. https://doi.org/10.3390/ma15207139.

[73] "Electronic Speed Controller (ESC): Everything You Need to Know," https://www.jouav.com/blog/electronic-speed-controller-esc.html, 2023. [Online; Accessed: February 2024].

[74] "MAD AMPX 300A(12-24S) HV ESC Regulator," https://www.mad-motor.com/products/mad-ampx-esc-300a-12-24s-hv-droneesc.html, 2015. [Online; Accessed: February 2024].